NANOMETRIC STRUCTURES AND NANOSECOND DYNAMICS OF POLYMERS STUDIED BY FLUORESCENCE METHODS

Hiroyuki AOKI

2001

TABLE OF CONTENTS

Part II. Nanosecond Dynamics Studied by Fluorescence Depolarization Method

---

Chapter 1

GENERAL INTRODUCTION

1.1. BACKGROUND AND MOTIVATION

1.1.1. Fluorescence Method for Studying Polymer Structure and Dynamics

Polymers have a variety of structures and properties, and many kinds of high performance polymers have been developed for various applications. The physical and chemical properties of polymer materials are closely correlated to their structures. In a polymeric system, the structure must be described over wide length scales from a nanometer to several tens of microns in terms of chemical structure, conformation, and assembled structure of the polymer chain. In addition to the structure, the motion of polymer chains has a great influence on the physical properties. In order to design and fabricate polymeric materials with novel properties and functions, it is indispensable to understand both the static and dynamic structures in a wide spatial and temporal scale. In particular, it is of great importance to understand these issues from a molecular viewpoint with both "molecular space" and "molecular time" resolutions.

For investigating the structures and dynamics of polymers, numerous experimental techniques have been proposed so far. The fluorescence method is one of the powerful techniques which have been successfully utilized in various research fields. Even a single photon is observable with sensitive photodetectors, so that the fluorescence method has been employed for studying small objects such as thin films[1-8] and micelles.[9-13] The most striking advantage of the fluorescence method is that it

provides various information at the molecular level. Since the fluorescence spectra and their time evolution reflect the interaction between the dye molecules and the surroundings within a region in a nanometric scale, microscopic environments[14-17] and spatial distribution[5,18-20] of molecules can be probed by fluorescence spectroscopy. For example, the energy transfer phenomenon is often utilized for characterization of nanometric structures.[5,19-21] The excitation energy on an energy donor molecule transfers onto an energy acceptor molecule when they are close to each other in a distance of < 10 nm. Since the energy transfer efficiency is greatly dependent on the distance between the dye molecules, the analyses of the fluorescence spectra and the time-dependent fluorescence profiles provide the spatial distribution of dye molecules in a nanometer scale. In addition to characterizing nano-structures, the fluorescence method is capable of probing the molecular motion in a time scale of nanoseconds which is the same time scale as the fluorescence lifetime of molecules.[22-34] Thus, the fluorescence technique is a powerful tool for studying the structure and the dynamics of polymer materials. The works in this thesis focus on the local structures and molecular dynamics of polymers in dimensions of nanometer (10^{-9} m) and nanosecond (10^{-9} sec), respectively, investigated by means of the fluorescence method.

1.1.2. Nanometric Structure

Nowadays, characterization and fabrication of structures in a length scale of 1 – 100 nm have attracted much attention as "Nano-Technology." This length scale is an intermediate region between a molecule and bulk materials, and the physical properties in a nanometric scale are substantially different from those in the bulk state. Therefore, it is possible to produce novel properties by fabricating a nanometric structure without changing the chemical composition of materials. Because the electronic interaction between functional groups occurs in a nanometric length scale, the fabrication of nano-structures enables one to control electro- and photofunctions.

Since the dimension of a polymer chain is 1 – 10 nm, polymer materials have drawn much attention as the basic components of nano-structures aiming at the control of physical properties in bulk materials, and also of their photonic and electronic functions.[6,35-39]

In order to design and fabricate nano-architectures, it is indispensable to establish methodology for observation of a nanometric system. As mentioned above, the fluorescence method is advantageous to obtain various information at the molecular level. Therefore, the combination of optical microscopy and fluorescence spectroscopy appears to be useful to obtain molecular information in a local area. However, the spatial resolution for the conventional microscopy is theoretically limited to a half of a wavelength of the probe light, i.e., 200 – 400 nm in the visible region.[40-42] This limitation is called the diffraction limit. Hence, the fluorescence method had not been applicable to the local area smaller than several hundred nanometers. In this decade, scanning near-field optical microscopy (SNOM) has been extensively developed as a novel optical microscopic technique with a spatial resolution beyond the diffraction limit of light.[43-51] SNOM has an advantage over other microscopic techniques in that it can be used to examine the chemical composition beneath the probe tip through fluorescence[51-54] and Raman[55-60] spectroscopy. Therefore, SNOM has attracted much attention as a powerful tool for chemical analysis in a nanometer scale. In addition to high-resolution imaging, SNOM has been developed as a nano-fabrication apparatus using the high energy density of the near-field, which brings about photochemical reactions and ablations.[61-65]

The first part of this thesis describes the development of SNOM in an ultra-violet region (UV-SNOM) and its applications to polymer systems. The versatility of UV-SNOM for both observation and fabrication of nanometric structures is demonstrated. SNOM was employed for studying the phase separation structure of polymer blend monolayers and the inhomogeneous structure of polymer networks. A monolayer is

an ultra-thin film with a thickness of a single molecular dimension. Sequential deposition of monolayers yields multi-layered films in a nanometric scale,[35,66-68] which are called Langmuir-Blodgett (LB) films. Polymer monolayers, which have developed recently, have drawn attention since they form stable nano-architectures due to the high thermal durability, thinness, and homogeneity. The conformation and the motion of a polymer chain in the monolayer are restricted because of the low degree of freedom. Therefore, two-dimensional polymers have different characteristics from those in the bulk state. The studies on the properties of polymer monolayers are important from the viewpoints not only of the practical applications of LB films but also of the fundamental physical chemistry of "polymer science in two dimensions."[69] On the other hand, polymer gels have been studied by many researchers because gels have unique and interesting characteristics such as volume phase transition.[70-72] It is known that a polymer gel has an inhomogeneous network structure resulting from the network formation process,[73-75] and it has a great influence on the physical properties.[76-78] Whereas the inhomogeneity of the network structure has been extensively studied, it cannot be said that detailed information has been obtained sufficiently.

1.1.3. Nanosecond Dynamics

Dynamics also has a great influence on the physical properties of polymers such as the glass transition and the viscoelasticity. Polymer chain motions have been studied by many workers from the theoretical and experimental points of view. The Rouse-Zimm model is the first theoretical model for the polymer dynamics.[79,80] This model consists of a set of beads connected with springs, and it well describes experimental results about the viscoelasticity of polymer solutions. Besides the Rouse-Zimm model, many other theories have been proposed for describing the chain dynamics in various time scales.[81-85] With respect to the experimental studies, a lot of

techniques have been employed so far. Especially, the local chain dynamics in a time scale of nanoseconds has been examined by NMR,[86-91] ESR,[92-95] and fluorescence depolarization.[22-34] Among them, the fluorescence depolarization method is a powerful technique to investigate the nanosecond dynamics because the orientational autocorrelation function can be obtained without any assumption of the models for motional modes.

The second part of this thesis describes the local dynamics of the chain center of poly(*N*-vinylcarbazole) (PVCz) in dilute solutions and the local motion of the crosslinking points of poly(methyl methacrylate) (PMMA) gels. PVCz is known as a photofunctional polymer, which was practically used for a photosensitive film in a copying machine. The photophysics and photochemistry of PVCz have been studied extensively. The motion of the PVCz chain has an influence on its photophysical processes. It is important to understand the local chain dynamics. On the other hand, a polymer gel consists of crosslinked network chains and swelling fluid. The properties of a gel are affected not only by the network structure but also by the dynamics of the network chain and the crosslinking point. In the studies presented in this thesis, the local motion of PVCz and PMMA gels are examined by the fluorescence depolarization method.

1.2. Overview of Experimental Techniques

1.2.1. Scanning Near-Field Optical Microscopy

The imaging mechanism of SNOM is briefly described here. Two small objects A and B are considered, which are placed at a distance shorter than a wavelength of light as illustrated in Figure 1.1a. When the object A is illuminated by light, there arise not only a propagating field such as scattered light, but also an optical near-field

restricted around the object. With the propagating component, one cannot observe structures with a spatial frequency higher than the frequency of the incident light. On the other hand, the near-field component has information on the local structure smaller than the wavelength of the incident light because the distribution of the optical near-field is dependent on the size and shape of the object A and exists only in the vicinity of A irrespective of the wavelength. Therefore, a local structure smaller than the wavelength can be observed by the measurement of the near-field component. However, since the near-field component does not propagate in the far-field, it cannot be directly observed by a detector at a distance much larger than a wavelength of light. Now, the other object B plays an important role in the observation of the near-field component around A. When the small object B is close to A in a distance shorter than the wavelength of the incident light, B scatters the local optical near-field around A as a propagating wave. Thus, the non-propagating optical near-field associated with A can be measured with a detector in the far-field as the propagating light scattered by B. The interaction between the two objects is strongest when they are the same size. This indicates that the high spatial resolution regardless of the wavelength is provided with a sufficiently small probe object.

In the case of the actual SNOM system, the objects A and B correspond to an optical fiber probe and a specimen, respectively, as shown schematically in Figure 1.1b. The fiber probe has an aperture much smaller than the wavelength of light at the sharpened end, and a laser beam coupled in the other end of the fiber is guided to the aperture through the fiber core. The optical near-field emanating from the aperture illuminates the sample surface, and the intensities of the scattered light and the fluorescence from the sample are monitored. The SNOM tip probes optical properties only in an area as large as the size of the aperture. Therefore, the scattered light and fluorescence intensities from the specimen are measured at point by point with scanning

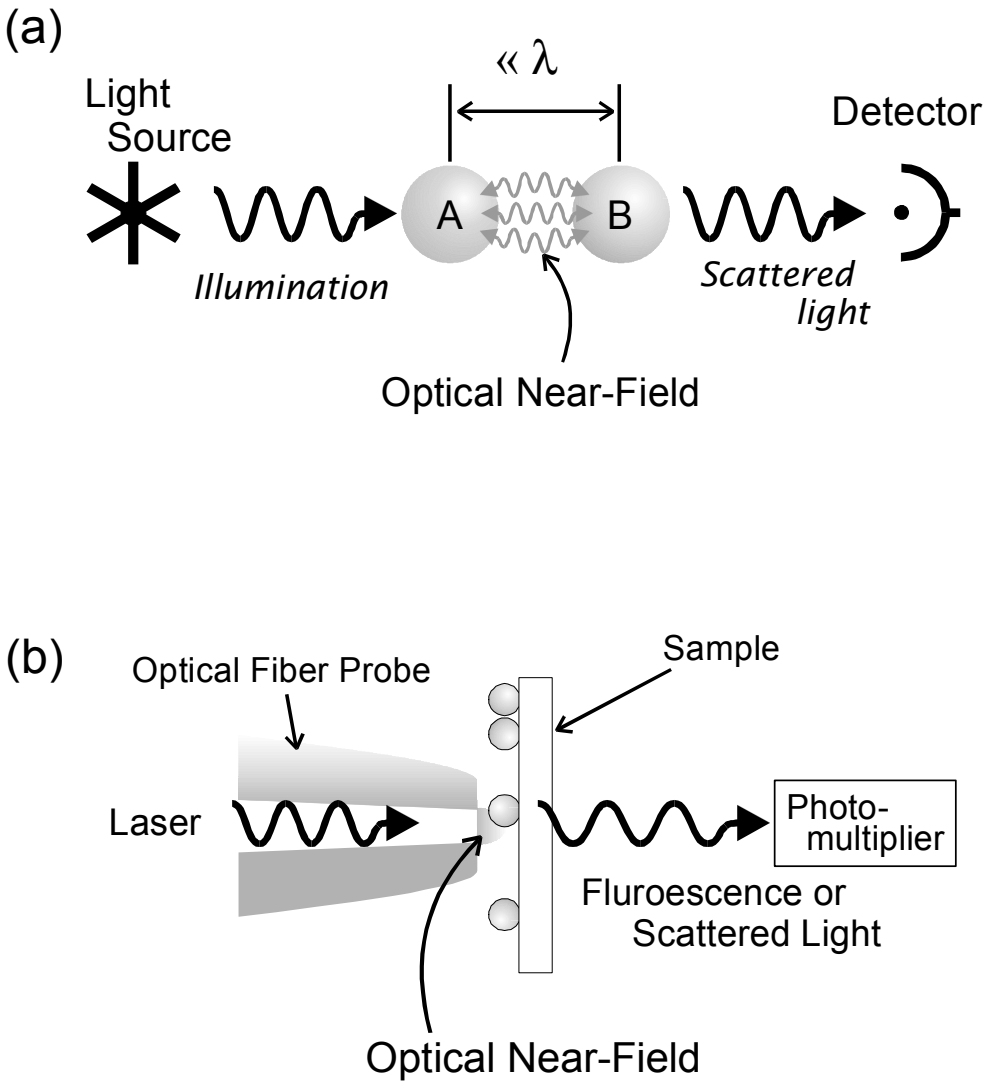

Figure 1.1. Schematic illustration for the optical near-field system. In (a), the two objects, A and B, are placed at a distance shorter than the wavelength of the light illuminating A. The scattered light from B is monitored by a detector in the far-field. In (b), the illumination-mode SNOM is depicted schematically. The objects A and B in (a) correspond to the optical fiber probe and the sample, respectively.

the probe tip. And then, the obtained micrograph is displayed as a two-dimensional array of the stored intensity data.

More than 70 years ago, Synge proposed the basic concept of SNOM with a scanned subwavelength-sized aperture.[96] However, the experimental demonstration could not be performed in those days because of the technical difficulties in fabrication of the nanometer-sized aperture, precise position control in a nanometer scale, and image processing of the obtained micrograph. The recent development of laser, piezo electrics, computer, and microfabrication technologies allowed the implementation of SNOM. Betzig et al. introduced a single-mode optical fiber to make a probe tip.[43,44] In their experiment, a sharpened fiber end was obtained by a heating-and-pulling process with a micropipette puller, and then the sides of the tapered region were metal coated by shadow-evaporation, leaving the apex uncoated as an aperture. Nowadays, this method is the most popular technique to fabricate a SNOM probe whereas many methods for the fabrication of a sharpened optical fiber have been reported.[45,97-102]

1.2.2. Fluorescence Depolarization Method

A fluorescent dye molecule has the transition moments, **M** and **E**, for excitation and emission, respectively. When the molecules are placed in an electric field of linearly polarized light, the selective excitation occurs for the molecules with the moment **M** parallel to the direction of the electric field. The excited dye molecules emit fluorescence polarized in the direction of the moment **E**. When the molecules rotate during the fluorescence lifetime, the direction of **E** differs from that of **M** at the moment of excitation. The different directions of **M** and **E** result in the fluorescence depolarization. Thus, the molecular motion in a nanosecond time scale can be examined through the fluorescence depolarization.

The formulation of the fluorescence depolarization is described here. Now, a fluorescent dye molecule with the transition moment, **M**, in the laboratory Cartesian

coordinate (x, y, z) is considered. **M** is fixed and oriented with a polar angle, θ, and an azimuthal angle, φ, as shown in Figure 1.2a. The excitation light, **P**, is linearly polarized in the z-direction. The fluorescence anisotropy ratio, r, is defined as

$$r = \frac{I_{\parallel} - I_{\perp}}{I_{\parallel} + 2I_{\perp}}, \tag{1.1}$$

where $I_{\parallel}$ and $I_{\perp}$ are the fluorescence components parallel and perpendicular to the polarization direction of the excitation light, respectively. In this geometry, $I_{\parallel}$ and $I_{\perp}$ observed for the fluorescent molecule are given as the following equations.

$$I_{\parallel} \propto \cos^2 \theta \tag{1.2}$$

$$I_{\perp} \propto \sin^2 \theta \cos^2 \varphi \tag{1.3}$$

The ensemble averaged fluorescence anisotropy ratio for randomly oriented chromophores is expressed as the following equation.

$$r = \frac{3\langle \cos^2 \theta \rangle - 1}{2}, \tag{1.4}$$

where the bracket $\langle\ \rangle$ indicates the ensemble average.

Next, the case of a rotating fluorescent molecule is considered. Suppose that the transition moment, **M**, rotates by the angle, δ, with respect to the initial orientation (θ, φ) during the time, t, as shown in Figure 1.2b. We introduce the localized Cartesian coordinate system (ξ, η, ζ) associated with **M**(0), which is defined by the Euler angles (θ, φ, 0) with respect to the external coordinate (x, y, z). The rotational angle δ corresponds to the polar angel of **M**(t) in the localized coordinate system (ξ, η, ζ). Now let ψ the azimuthal angle of **M**(t) in the local coordinate system, and $\theta(t)$ the polar angle of **M**(t) with respect to the laboratory coordinate (x, y, z). Then, $\theta(t)$ is related to θ, δ, and ψ according to the following equation,

$$\cos\theta(t) = -\sin\theta \sin\delta \cos\psi + \cos\theta \cos\delta \tag{1.5}$$

The fluorescence anisotropy ratio at time t, $r(t)$, is expressed by the following equations.

$$r(t) = \frac{3\langle \cos^2 \theta(t) \rangle - 1}{2}$$

$$= \frac{3\langle \cos^2 \theta \rangle - 1}{2} \cdot \frac{3\langle \cos^2 \delta \rangle - 1}{2}$$

$$= r_0 \frac{3\langle \cos^2 \delta \rangle - 1}{2}, \tag{1.6}$$

where

$$r_0 = \frac{3\langle \cos^2 \theta \rangle - 1}{2}. \tag{1.7}$$

r_0 is the fluorescence anisotropy at t = 0. On the other hand, the orientational autocorrelation function, $C_2(t)$, is defined as

$$C_2(t) = \langle P_2[\mathbf{M}(0) \cdot \mathbf{M}(t)] \rangle$$

$$= \frac{3\langle \cos^2 \delta \rangle - 1}{2}, \tag{1.8}$$

where P_2 is a Legendre polynomial of the second order. It should be noted that the normalized anisotropy, $r(t)/r_0$, has the same form as the orientational autocorrelation function for the transition moment of the dye molecule. Thus, the autocorrelation function in the time scale of the fluorescence lifetime can be directly obtained without any assumption of models through the time-resolved fluorescence anisotropy measurement.

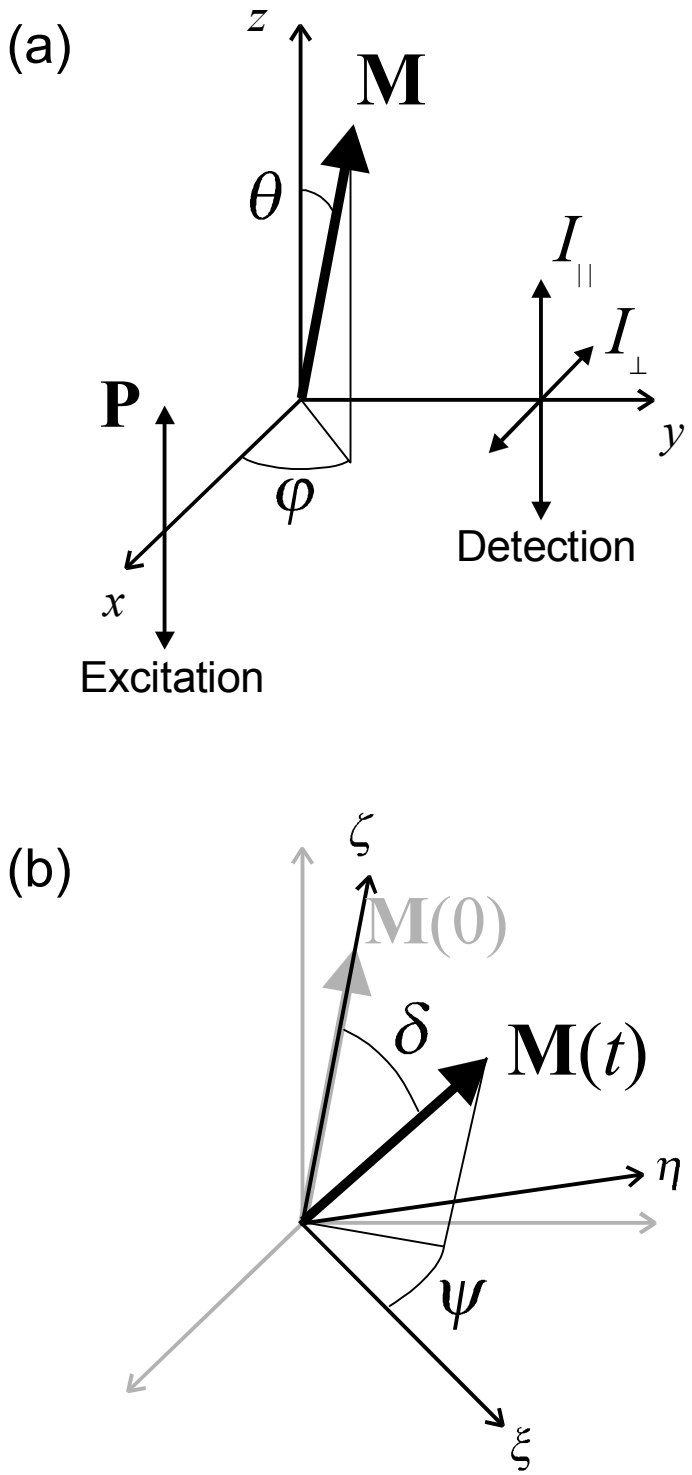

Figure 1.2. Experimental geometry of the fluorescence depolarization method. The laboratory fixed Cartesian coordinate system (x, y, z) (a) and the localized Cartesian coordinate system (ξ, η, ζ) associated with the transition moment **M**(0) which is defined by the Euler angles (θ, φ, 0) with respect to the laboratory fixed coordinate system (b).

1.3. OUTLINE OF THIS THESIS

This thesis consists of seven chapters. The first chapter describes the background and the motivation of this thesis. The principles of the scanning near-field optical microscopy and the fluorescence depolarization method are also mentioned. The following chapters are divided into two parts.

In Part I, nanometric structures of polymer systems are studied by the scanning near-field optical microscopy. Chapter 2 describes the development of SNOM operated in a UV region (UV-SNOM) and its applications to polymer systems. An optical fiber probe made from pure quartz allows one to use UV light in SNOM measurements. UV-SNOM covers a wide range of excitation wavelengths from ultraviolet to near-infrared region. Therefore, a variety of molecules can be probed through spectroscopic measurements. Polymer nano-particles on a substrate are imaged with a high spatial resolution, and the chemical species for each particle is determined through near-field fluorescence spectroscopy. The high energy density of UV optical near-field brings about photochemical reactions in a nanometric area. The photopatterning with UV near-field illumination is performed on a polymer monolayer, and the resolution is discussed. The weak fluorescence from a perylene-labeled polymer can be efficiently enhanced by the energy transfer mechanism from carbazole under the UV excitation, and the high detection sensitivity of SNOM enables one to observe of the fluorescence from the single polymer chains in a monolayer. These experiments demonstrate that UV-SNOM is a powerful tool for spectroscopic analysis in a nanometric area and fabrication of nano-structures in addition to imaging capability with a high spatial resolution.

In Chapter 3, the phase separation structure for a mixed monolayer of pyrene-labeled poly(isobutyl methacrylate) (PiBMA-Py) and perylene-labeled poly(octadecyl methacrylate) (PODMA-Pe) is investigated by the fluorescence SNOM. Light sources

with various wavelengths can be employed in UV-SNOM. By choosing the proper excitation wavelength, each phase of the PiBMA-Py / PODMA-Pe is selectively imaged as a bright area. SNOM images are obtained by collecting the energy transfer emission, which probes the region where both components are mixed at the molecular level. For the completely phase-separated monolayer, the structure of the phase boundary is discussed through the energy transfer SNOM image.

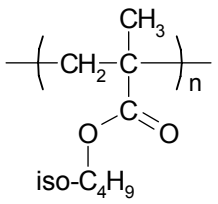

PiBMA

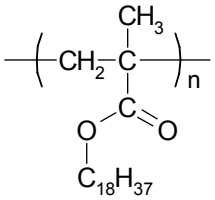

PODMA

In Chapter 4, the phase separation behavior of polymer blend monolayers consisting of dye-labeled PODMA and PiBMA is investigated in detail. The phase separation process with annealing is discussed through SNOM measurements. The factors governing the phase separation structure are discussed in terms of their chemical structures. The time-resolved SNOM measurement is carried out across the phase interface of the completely phase-separated monolayer. Through the fluorescence decay curves, the phase boundary structure is discussed in comparison with that of a phase-separated bulk system.

Chapter 5 deals with the SNOM study on structural inhomogeneity of poly(methyl methacrylate) (PMMA) networks. The fluorescence SNOM measurements are performed for the PMMA networks labeled at side chains and crosslinking points. The advantage of SNOM in the study of the gel structure is described. The spatial distributions of the chain segments and the crosslinks are visualized in real space. The SNOM image shows that the PMMA network has an inhomogeneous structure in a length scale of submicrons. The energy transfer dynamics among the dyes introduced to the side chains is also examined in order to

probe the chain segment density at the molecular level. We discuss the difference between the structures observed in submicron and molecular scales.

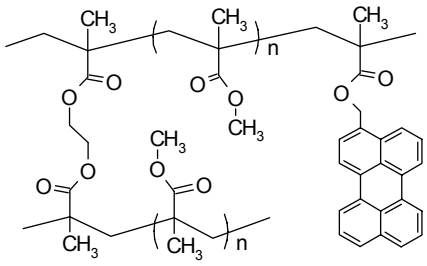

Side-chain-labeled PMMA network

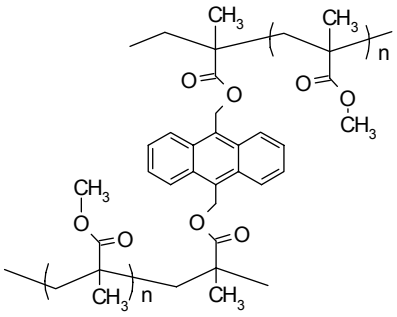

Crosslink-labeled PMMA network

In Part II, dynamics of polymer chains in a nanosecond temporal scale is investigated by the time-resolved fluorescence depolarization method. In Chapter 6, the local segmental motion of poly(*N*-vinylcarbazole) (PVCz) at the center of the main chain in dilute solutions is investigated. The relaxation time and the activation energy of the local motion in Θ and good solvents are evaluated through the fluorescence anisotropy decay for the PVCz samples with various molecular weights from 9.2×10^3 to 1.0×10^5. The factors governing the local dynamics in dilute solutions are discussed in terms of the molecular weight and solvent quality. Both the relaxation time and the activation energy for PVCz are compared with those for other polymers, and the difference from the other polymers is discussed.

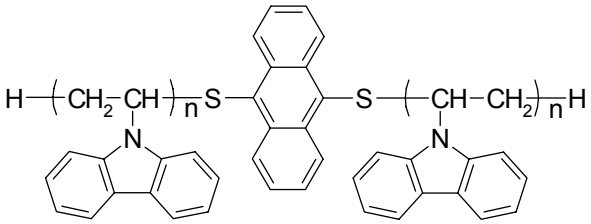

Anthracence-labeled PVCz

In Chapter 7, the local motion of the crosslinking points of poly(methyl methacrylate) (PMMA) gels is studied by the fluorescence depolarization method. The relaxation time and the activation energy of local motion are measured for PMMA

gels at the swollen states in various solvents through fluorescence anisotropy decay. The local dynamics of the crosslinking points is discussed in terms of the solvent quality, molecular weight between crosslinks, and swelling ratio.

References

1. S. Ohmori, S. Ito, and M. Yamamoto, *Macromolecules*, **24**, 2377 (1991).
2. S. Ito, K. Kanno, S. Ohmori, Y. Onogi, and M. Yamamoto, *Macromolecules*, **24**, 659 (1991).
3. S. Ito, S. Oki, N. Sato, and M. Yamamoto, *Macromolecules*, **29**, 724 (1996).
4. F. Feng, M. Mitsuishi, and T. Miyashita, *Langmuir*, **15**, 8673 (1999).
5. N. Sato, Y. Osawa, S. Ito, and M. Yamamoto, *Polym. J.*, **31**, 488 (1999).
6. H. Ohkita, H. Ishii, S. Ito, and M. Yamamoto, *Chem. Lett.*, 1092 (2000).
7. E. H. Ellison and J. K. Thomas, *Langmuir*, **12**, 1870 (1996).
8. P. Ballet, M. Van der Auweraer, F. C. De Schryver, H. Lemmetyinen, and E. Vuorimaa, *J. Phys. Chem.*, **100**, 13701 (1996).
9. C. K. Smith and G. Liu, *Macromolecules*, **29**, 2060 (1996).
10. M. Mizusaki, Y. Morishima, K. Yoshida, and P. L. Dubin, *Langmuir*, **13**, 6941 (1997).
11. T. Kawamoto and Y. Morishima, *Langmuir*, **14**, 6669 (1998).
12. R. Ranganathan, M. Peric, and B. L. Bales, *J. Phys. Chem. B*, **102**, 8436 (1998).
13. S. Matzinger, D. M. Hussey, and M. D. Fayer, *J. Phys. Chem. B*, **102**, 7216 (1998).
14. D. C. Dong and M. A. Winnik, *Can. J. Chem.*, **62**, 2560 (1984).
15. Y. Hu, K. Horie, and H. Ushiki, *Macromolecules*, **25**, 6040 (1992).
16. Y. Hu, K. Horie, H. Ushiki, T. Yamashita, and F. Tsunomori, *Macromolecules*, **26**, 1761 (1993).
17. K. Iwai, K. Hanasaki, and M. Yamamoto, *J. Luminescence*, **87-89**, 1289 (2000).
18. E. Perez and J. Lang, *J. Phys. Chem. B*, **103**, 2072 (1999).
19. O. Tcherkasskaya, S. Ni, and M. A. Winnik, *Macromolecules*, **29**, 610 (1996).
20. O. Tcherkasskaya, J. G. Spiro, S. Ni, and M. A. Winnik, *J. Phys. Chem.*, **100**,

7114 (1996).

21. Y. Ishii, T. Funatsu, T. Wazama, T. Yoshida, J. Watai, M. Ishii, and T. Yanagida, *Biophys. J.*, **72**, A283 (1997).
22. T. Sasaki, M. Yamamoto, and Y. Nishijima, *Macromolecules*, **21**, 610 (1988).
23. T. Sasaki and M. Yamamoto, *Macromolecules*, **22**, 4009 (1989).
24. K. Ono, K. Ueda, and M. Yamamoto, *Polym. J.*, **26**, 1345 (1994).
25. K. Ono, T. Sasaki, M. Yamamoto, Y. Yamasaki, K. Ute, and K. Hatada, *Macromolecules*, **27**, 5012 (1995).
26. J. Horinaka, K. Ono, and M. Yamamoto, *Polym. J.*, **27**, 429 (1995).
27. J. Horinaka, S. Amano, H. Funada, S. Ito, and M. Yamamoto, *Macromolecules*, **31**, 1197 (1998).
28. H. Aoki, J. Horinaka, S. Ito, and M. Yamamoto, *Polym. Bull.*, **37**, 109 (1997).
29. J. Horinaka, H. Aoki, S. Ito, and M. Yamamoto, *Polym. J.*, **31**, 172 (1999).
30. J. Horinaka, M. Maruta, S. Ito, and M. Yamamoto, *Macromolecules*, **32**, 1134 (1999).
31. J. Horinaka, S. Ito, M. Yamamoto, Y. Tsujii, and T. Matsuda, *Macromolecules*, **32**, 2270 (1999).
32. D. A. Waldow, M. D. Ediger, Y. Yamaguchi, Y. Matsushita, and I. Noda, *Macromolecules*, **24**, 3147 (1991).
33. A. D. Stein, D. A. Hoffman, C. W. Frank, and M. D. Fayer, *J. Phys. Chem.*, **96**, 3269 (1992).
34. P. B. Leezenberg, A. H. Marcus, C. W. Frank, and M. D. Fayer, *J. Phys. Chem.*, **100**, 7646 (1996).
35. A. Ulman, "An Introduction to Ultrathin Films from Langmuir-Blodgett to Self-Assembly," Academic Press, San Diego, 1991.
36. T. Taniguchi, Y. Fukasawa, and T. Miyashita, *J. Phys. Chem. B*, **103**, 1920 (1999).

37. J. A. Forrest, K. Dalnoki-Veress, J. R. Stevens, and J. R. Dutcher, *Phys. Rev. Lett.*, **77**, 2002 (1996).
38. J. A. Forrest, C. Svanberg, K. Revesz, M. Rodahl, L. M. Torell, and B. Kasemo, *Phys. Rev. E*, **58**, 1226 (1998).
39. Y. See, J. Cha, T. Chang, and M. Ree, *Langmuir*, **16**, 2351 (2000).
40. E. Abbe, *J. Roy. Microsc. Soc.*, **2**, 300 (1882).
41. E. Abbe, *J. Roy. Microsc. Soc.*, **2**, 460 (1882).
42. M. Born and E. Wolf, "Principles of Optics," Pergamon Press, New York, 1975.
43. E. Betzig, J. K. Trautman, T. D. Harris, J. S. Weiner, and R. L. Kostelak, *Science*, **251**, 1468 (1991).
44. E. Betzig and J. K. Trautman, *Science*, **257**, 189 (1992).
45. M. Ohtsu, "Near-Field Nano/Atom Optics and Technology," Springer, Tokyo, 1998.
46. M. A. Paesler and P. J. Moyer, "Near-Field Optics: Theory, Instrumentation, and Applications," John Wiley & Sons, New York, 1996.
47. W. P. Ambrose, P. M. Goodwin, J. C. Martin, and R. A. Keller, *Science*, **265**, 364 (1994).
48. X. S. Xie and R. C. Dunn, *Science*, **265**, 361 (1994).
49. X. S. Xie, *Acc. Chem. Res.*, **29**, 598 (1996).
50. B. Hecht, B. Sick, U. P. Wild, V. Deckert, R. Zenobi, O. J. F. Martin, and D. W. Pohl, *J. Chem. Phys.*, **112**, 7761 (2000).
51. D. A. Vanden Bout, J. Kerimo, D. A. Higgins, and P. F. Barbara, *Acc. Chem. Res.*, **30**, 204 (1997).
52. T. Ha, T. Enderle, D. F. Ogletree, D. S. Chemla, P. R. Selvin, and S. Weiss, *Proc. Natl. Acad. Sci. USA*, **93**, 6264 (1996).
53. J. Hofkens, L. Latterini, P. Vanoppen, H. Faes, K. Jeuris, S. De Feyter, J. Kerimo, P. F. Barbara, and F. C. De Schryver, *J. Phys. Chem. B*, **101**, 10588 (1997).

54. J. Kerimo, D. M. Adams, P. F. Barbara, D. M. Kaschak, and T. E. Mallouk, *J. Phys. Chem. B*, **102**, 9451 (1998).

55. C. L. Jahncke, M. A. Paesler, and H. D. Hallen, *Appl. Phys. Lett.*, **67**, 2483 (1995).

56. S. Webster, D. N. Batchelder, and D. A. Smith, *Appl. Phys. Lett.*, **72**, 1478 (1998).

57. Y. Narita, T. Tadokoro, T. Ikeda, T. Saiki, S. Mononobe, and M. Ohtsu, *Appl. Spectrosc.*, **52**, 1141 (1998).

58. V. Deckert, D. Zeisel, R. Zenobi, and T. Vo-Dinh, *Anal. Chem.*, **70**, 2646 (1998).

59. R. M. Stockle, Y. D. Suh, V. Deckert, and R. Zenobi, *Chem. Phys. Lett.*, **318**, 131 (2000).

60. N. Hayazawa, Y. Inouye, Z. Sekkat, and S. Kawata, *Opt. Commun.*, **183**, 333–336 (2000).

61. S. Davy and M. Spajer, *Appl. Phys. Lett.*, **69**, 3306 (1996).

62. D. P. Tsai and W. R. Guo, *J. Vac. Sci. Technol. A*, **15**, 1442 (1997).

63. A. Naber, T. Dziomba, U. C. Fischer, H. -J. Maas, and H. Fuchs, *Appl. Phys. A*, **70**, 227 (2000).

64. S. Nolte, B. N. Chichkov, H. Welling, Y. Shani, K. Lieberman, and H. Terkel, *Opt. Lett.*, **24**, 914 (1999).

65. R. Zenobi and V. Deckert, *Angew. Chem. Int. Ed.*, **39**, 1746 (2000).

66. K. B. Blodgett, *J. Am. Chem. Soc.*, **56**, 495 (1934).

67. K. B. Blodgett, *J. Am. Chem. Soc.*, **57**, 1007 (1935).

68. G. L. Gaines, Jr., "Insoluble Monolayers at Liquid-Gas Interfaces," Wiley-Interscience, New York, 1966.

69. N. Sato, Doctoral Thesis, Kyoto University, 1998.

70. T. Tanaka, *Phys. Rev. Lett.*, **40**, 820 (1978).

71. T. Tanaka, D. Fillmore, S.-T. Sun, I. Nishio, G. Swislow, and A. Shah, *Phys. Rev.*

Lett., **45**, 1636 (1980).

72. Y. Hirokawa and T. Tanaka, *J. Phys. Chem.*, **81**, 6379 (1984).
73. E. Sato-Matsuo, M. Orkisz, S.-T. Sun, Y. Li, and T. Tanaka, *Macromolecules*, **27**, 6791 (1994).
74. M. Shibayama, T. Norisuye, and S. Nomura, *Macromolecules*, **29**, 8746 (1996).
75. M. Shibayama, F. Ikkai, Y. Shiwa, and Y. Rabin, *J. Chem. Phys.*, **107**, 5227 (1997).
76. N. Weiss, T. van Vliet, and A. Silberberg, *J. Polym. Sci., Polym. Phys. Ed.*, **17**, 2229 (1979).
77. T. P. Hsu, D. S. Ma, and C. Cohen, *Polymer*, **24**, 1273 (1983).
78. S. Mallam, F. Horkay, A. M. Hecht, and E. Geissler, *Macromolecules*, **22**, 3356 (1989).
79. P. E. Rouse, *J. Chem. Phys.*, **21**, 1272 (1953).
80. B. H. Zimm, *J. Chem. Phys.*, **24**, 269 (1956).
81. E. Helfand, *J. Chem. Phys.*, **54**, 4651 (1971).
82. B. Valeuer, J.-P. Jarry, F. Geny, and L. Monnerie, *J. Polym. Sci.,Polym. Phys.Ed.*, **13**, 667 (1975).
83. M. Doi and S. F. Edwards, "The Theory of Polymer Dynamics," Clarendon Press, Oxford, 1986.
84. G. J. Moro, *J. Chem. Phys.*, **97**, 5749 (1992).
85. H. Yamakawa, "Helical Wormlike Chains in Polymer Solutions," Springer, Berlin, 1997.
86. R. Dejean de la Batie, F. Laupretre, and L. Monnerie, *Macromolecules*, **21**, 2052 (1988).
87. S. Glowinkowski, D. J. Gisser, and M. D. Ediger, *Macromolecules*, **23**, 3520 (1990).
88. W. Zhu and M. D. Ediger, *Macromolecules*, **28**, 7549 (1995).

89. C. Baysal, B. Erman, I. Bahar, F. Laupretre, and L. Monnerie, *Macromolecules*, **30**, 2058 (1997).

90. M. M. Fuson, K. H. Hanser, and M. D. Ediger, *Macromolecules*, **30**, 5714 (1997).

91. A. Karali, P. Dais, and F. Heatley, *Macromolecules*, **33**, 5524 (2000).

92. A. T. Bullok, G. G. Cameron, and P. M. Smith, *J. Phys. Chem.*, **77**, 1635 (1973).

93. M. Shiotani, J. Sohma, and J. H. Freed, *Macromolecules*, **16**, 1495 (1983).

94. J. Pilar and J. Labsky, *Macromolecules*, **27**, 3977 (1994).

95. J. Pilar, J. Labsky, A. Marek, D. E. Budil, K. A. Earle, and J. H. Freed, *Macromolecules*, **33**, 4438 (2000).

96. E. H. Synge, *Phil. Mag.*, **6**, 356 (1928).

97. G. A. Valaskovic, M. Holton, and G. H. Morrison, *Appl. Opt.*, **34**, 1215 (1995).

98. M. N. Islam, X. K. Zhao, A. A. Said, S. S. Mickel, and C. F. Vail, *Appl. Phys. Lett.*, **71**, 2886 (1997).

99. J. A. Veerman, A. M. Otter, L. Kuipers, and N. F. van Hulst, *Appl. Phys. Lett.*, **72**, 3115 (1998).

100. S. Mononobe, T. Saiki, T. Suzuki, S. Koshihara, and M. Ohtsu, *Opt. Commun.*, **146**, 45 (1998).

101. R. Stockle, C. Fokas, V. Deckert, R. Zenobi, B. Sick, B. Hecht, and U. P. Wild, *Appl. Phys. Lett.*, **75**, 160 (1999).

102. T. Saiki and K. Matsuda, *Appl. Phys. Lett.*, **74**, 2773 (1999).

Part I

NANOMETRIC STRUCTURES STUDIED BY SCANNING NEAR-FIELD OPTICAL MICROSCOPY

Chapter 2

SCANNING NEAR-FIELD OPTICAL MICROSCOPY IN THE ULTRA-VIOLET REGION: APPLICATIONS TO POLYMER SYSTEMS

2.1. INTRODUCTION

Scanning near-field optical microscopy (SNOM) is a recently developed scanning probe microscopic technique with a high spatial resolution beyond the diffraction limit of light.[1-4] Besides imaging of a specimen, SNOM enables one to obtain spectroscopic information[5-7] in a nanometric area illuminated with an optical near-field which is emanating from an aperture of subwavelength size. Since SNOM is also applicable to high-resolution recording by using photochemical reactions at a tiny spot under the aperture,[8-10] this apparatus has attracted much attention from various fields of researchers. So far, far-field spectroscopy has been extensively carried out for studying photophysics and photochemistry of dye molecules. Carbazole,[11-13] pyrene,[14,15] and naphthalene[16,17] are just a few of well-defined chromophores in polymeric systems. It would be interesting to investigate the photophysical processes in a nanometric scale because our knowledge on the photoprocesses has been based on the properties averaged over a large volume shone by the far-field light.

From the practical point of view, most of chromophores have the absorption bands in an ultra-violet (UV) range of 200 − 400 nm, and the excited states produced undergo physical and/or chemical reactions, some of which have been utilized for

applications such as coating, curing, recording, and microfabrication of the semiconductor devices. Thus, the use of SNOM in the UV region is an important progress not only for the fundamental study of photophysics and photochemistry but also for applications. However, only a few studies of SNOM in the UV region have been reported so far.[18-20] The difficulties in the UV-SNOM measurement result from the optical fiber probe. Commercial SNOM fibers usually contain a dopant such as GeO_2 which causes a serious problem that the guided UV light is absorbed by the dopant, yielding the autofluorescence from the fiber itself. Mononobe et al. overcame this problem by making a triple-tapered fiber probe with the double-step index core made of GeO_2-doped silica and pure silica. The GeO_2-doped region in the core was only 0.1 μm in diameter, so that the undesired fluorescence from the fiber probe was remarkably reduced.

In the present chapter, we employed an optical fiber probe with a pure silica core.[2] Using the 325-nm line of a He-Cd laser, the UV-SNOM is applied to the detection of nano-particles of polymer latex, an ultra-thin polymer monolayer, and a single polymer chain despersed in a polymer film, in order to demonstrate its versatile characteristics. The experiments shown here exemplify the high spatial resolution of the new optical microscope, the extreme sensitivity of fluorescence detection, and the spectroscopic performance, capable of probing molecular information and the excitation dynamics in a nanometric space.

2.2. EXPERIMENTS

2.2.1. Scanning Near-Field Optical Microscope

SNOM probes were made from an optical fiber with a pure silica core by a chemical etching method combined with a heating-and-pulling process.[2] The optical fiber was sharpened with a commercial micropipette puller (P-2000, Sutter Instrument), and then the sharpened end was immersed in a buffered hydrogen fluoride solution,

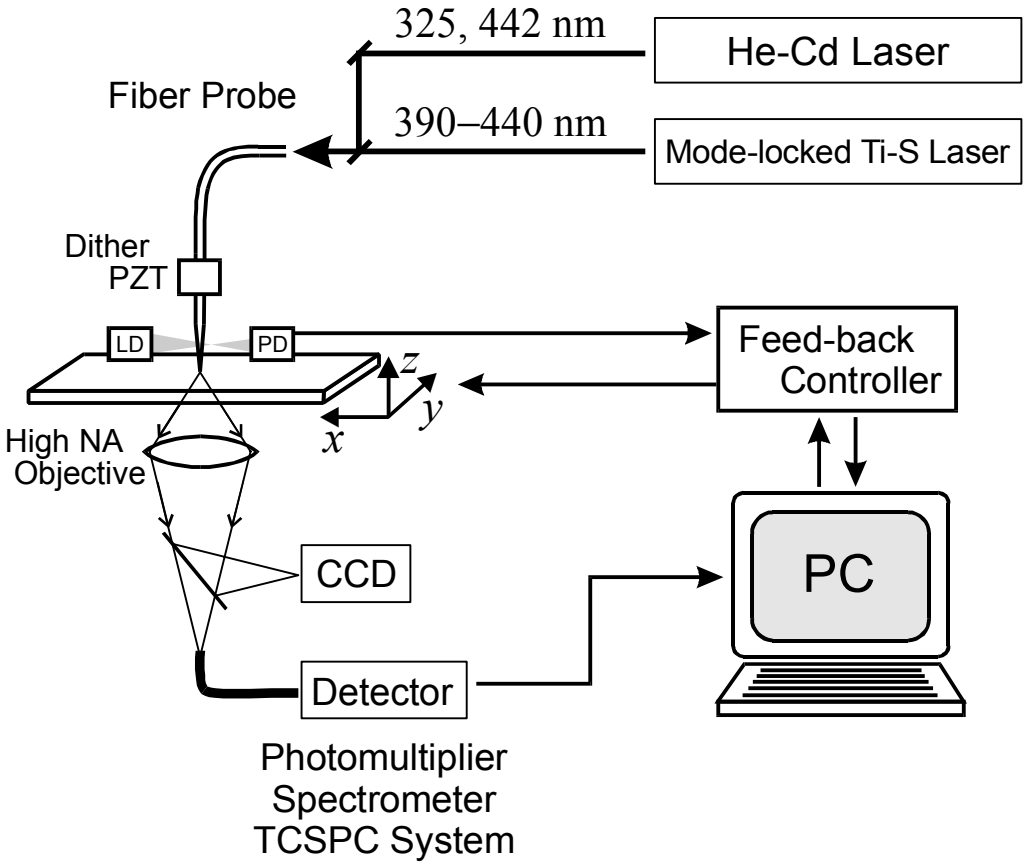

Figure 2.1. Block diagram for the SNOM system. The fluorescence from a specimen was collected by a high NA objective and guided to a detector through a milti-mode optical fiber.

which consisted of 40 wt% NH_4F aqueous solution, 48 wt% hydrofluoric acid, and distilled water with a ratio of 10 / 1 / 1 by volume. The etching time was 40 – 60 min at room temperature. The side of the probe was metal-coated except the apex to make an aperture of 50 – 100 nm in diameter.

The SNOM system used in this study was based on a commercially available instrument (SP-301, Unisoku). The block diagram is shown in Figure 2.1. Since the optical near-field exists only at the vicinity of the SNOM tip end, the distance between the tip end and the sample surface must be regulated to a constant value in a nanometer scale. The tip-sample gap was controlled by a shear force feed-back system. The SNOM probe was mechanically vibrated at its resonant frequency (typically 30 – 50 kHz) by a piezo electrics. A 780-nm diode laser beam was focused on the probe and its shadow was detected by a divided photodiode. The amplitude of the probe oscillation was monitored by a lock-in amplifier as the difference of the output voltages for the both sides of the photodiode. Figure 2.2 shows the resonance spectrum for a SNOM probe and the relationship between the tip-sample distance and the amplitude of the probe oscillation. The feed-back control of a z-piezo tube maintained the tip-sample distance to a constant value of 3 – 5 nm. The light sources were a He-Cd laser (IK5351R-D, Kimmon Electric) and a Ti:sapphire laser (Tsunami, Spectra Physics). The laser beam of the He-Cd laser was attenuated to a few mW by an appropriate neutral density filter. For the Ti:sapphire laser, the second harmonic with an average power of 300 – 400 μW was directly coupled into the cleaved end of the optical fiber probe. The fluorescence from the sample was collected by a high NA objective (1.3 NA; 100×, Nikon) and coupled into a multi-mode optical fiber. The collected light was guided to a photomultiplier tube (PMT; R2949 or R4220P, Hamamatsu Photonics) through optical filters for taking a SNOM image with appropriate wavelengths. In order to obtain fluorescence spectra, the fiber was connected to a computer-controlled monochrometer equipped with a PMT.

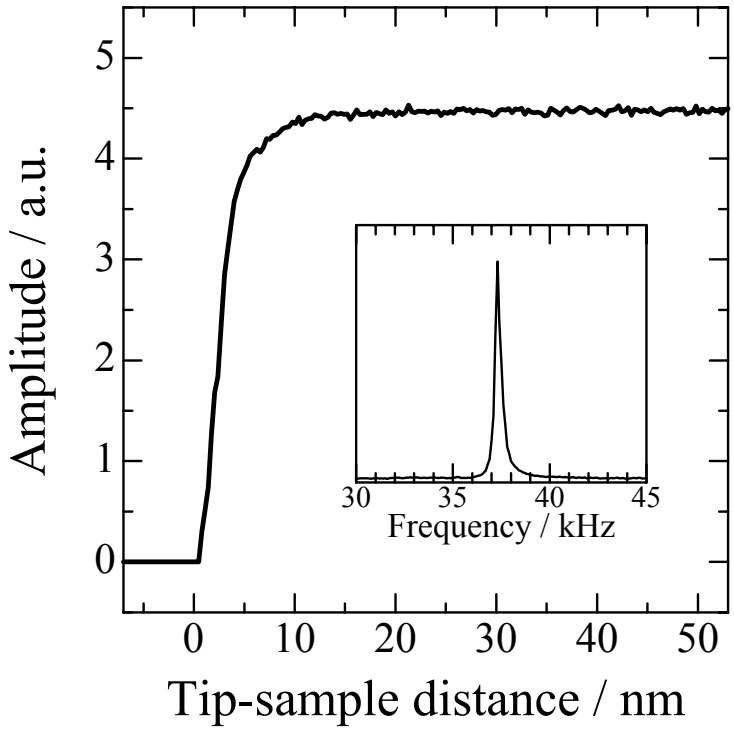

Figure 2.2. Relationship between the oscillation amplitude and the probe-sample distance. The inset shows the resonance spectrum for a SNOM probe.

2.2.2. Materials

The commercial fluorescent latex beads, 0.1μ BB and 0.1μ YG (Fluoresbrite™, Polyscience), with a diameter of 100 nm were used. They are different in the labeled fluorescent dye. The latex 0.1μ BB absorbs UV light at the wavelength of 300 – 390 nm and emits fluorescence from 360 to 490 nm, and the latex 0.1μ YG absorbs the visible range of 390 – 490 nm and emits fluorescence from 470 to 620 nm. Equal amounts of 0.1μ BB and YG were mixed and dispersed in a 4 wt% poly(vinyl alcohol) aqueous solution. The obtained latex dispersion was spin-cast on a cover slip.

Polymer monolayers were employed for the experiments of the nano-photolithography and the single polymer chain detection. Poly(isobutyl methacrylate)

(PiBMA), which is known to form a stable monolayer,[12,21] was used for the monolayer preparation. The side-chain of the PiBMA was labeled with fluorescent dyes, perylene (PiBMA-Pe), carbazole (PiBMA-Cz), and pyrene (PiBMA-Py), by means of copolymerization of isobutyl methacrylate and a dye-labeled methacrylate monomer. Table 2.1 summarizes the characterization of the polymers: number-averaged molecular weight, M_n, molecular weight dispersion, M_w/M_n, and the fraction of the fluorescent moiety introduced to the side-chain, f. The monolayers were prepared by the Langmuir-Blodgett technique.

Table 2.1. Characterization of Sample Polymers

	$M_n \times 10^{-3}$	M_w/M_n	f / %
PiBMA-Pe	2,700	1.25	1.3
PiBMA-Cz	52	3.06	20.2
PiBMA-Py	40	2.05	2.9

2.3. RESULTS AND DISCUSSION

2.3.1. Characterization of SNOM Probe for UV Excitation

The optical fiber probe is the most crucial part in the SNOM experiment. Figure 2.3 shows the scanning electron microscope (SEM) image of the end of the tip prior to metal coating. The taper angle and the radius of curvature at the tip end were 30 degree and less than 20 nm, respectively. Both the aperture size and the tip shape have a great influence on the quality of the obtained micrograph. The size of the aperture determines the area illuminated with the optical near-field, so that the spatial

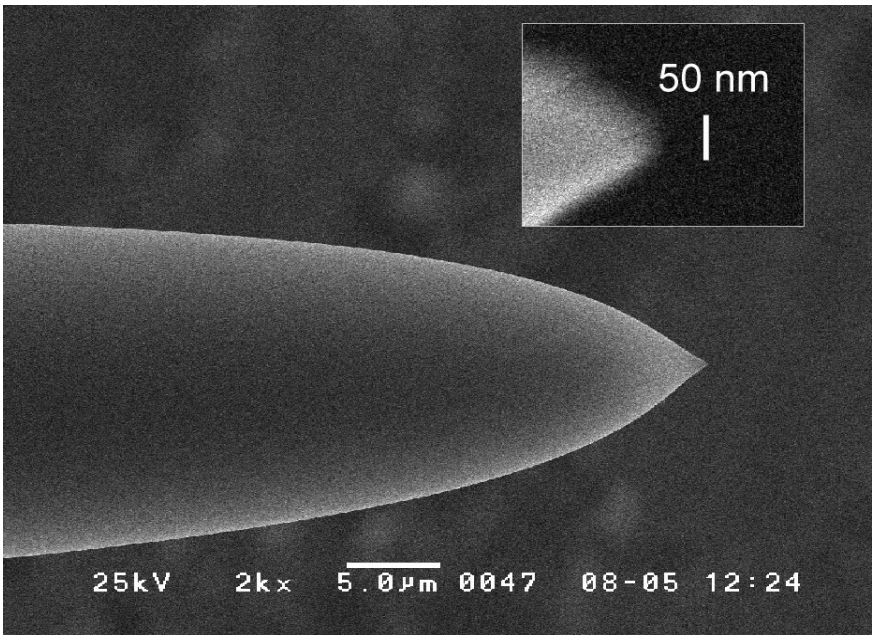

Figure 2.3. SEM micrographs for the end of a homemade SNOM probe.

resolution of the illumination-mode SNOM is governed by the aperture diameter. The throughput of the fiber probe is affected not only by the aperture diameter but also by the geometry at the tip end.[2,3,22] The laser beam coupled in the optical fiber is guided to the sharpened end through the fiber core, however, the intensity of the light delivered to the tip end is attenuated in the tapered region. Therefore, in order to gain a high throughput, the tapered region should be reduced as short as possible. Novotny et al. examined the effect of the taper angle on the throughput and the spatial resolution by the numerical simulation according to the multiple multipole method.[22] They concluded that the optimum taper angle both for the high resolution and the high throughput is 30 – 50 degree, which is in good agreement with the taper angle of the SNOM probe fabricated by the pulling-and-etching method as shown in Figure 2.3.

The spectroscopic measurements were performed for the light transmitted through the homemade SNOM probe and commercially available ones. The laser beam at a

wavelength of 325 nm was coupled to the cleaved end of the optical fiber. As shown in Figure 2.4, the commercial SNOM probes absorb the UV light and emit the autofluorescence, which interrupts the detection of the weak fluorescence from the specimen. This is due to the dopant in the optical fiber core. On the other hand, the autofluorescence for the homemade SNOM probe is negligible under the same experimental conditions for the commercial ones. Thus, the SNOM probe made from the pure silica optical fiber[2] enables one to carry out the fluorescence measurements in the UV region.

2.3.2. SNOM Measurement of Latex Particles

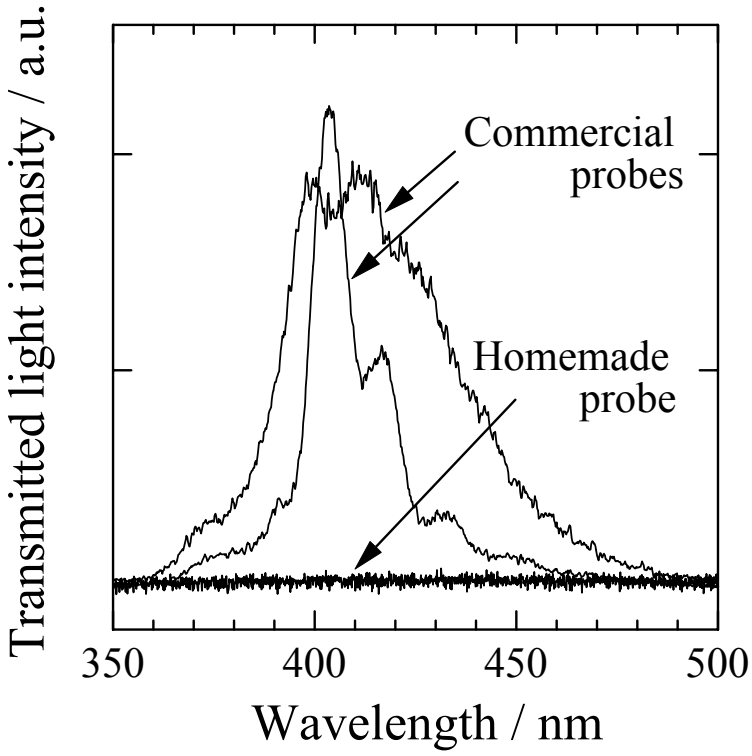

Figure2.4. Spectra for the light transmitted through homemade and commercially available SNOM probes. The wavelength of the incident light was 325 nm.

Figure 2.5 shows the SNOM images for the latex particles. Figure 2.5a depicts a transmission SNOM image, which was taken by monitoring the light scattered at the sample surface. The topographical feature of the surface has a great influence on the image contrast,[3,23,24] therefore, all the particles on the surface can be seen in the transmission image. The green and blue fluorescence spots in Figures 2.5b and 2.5c were observed by collecting the fluorescence in the range of 460 – 650 nm and 360 – 400 nm, respectively. Because the latex 0.1μ YG emits the fluorescence at 470 – 620 nm, it was measured only in Figure 2.5b and could not be seen in Figure 2.5c. On the other hand, the latex 0.1μ BB could be measured as the bright spots in Figure 2.5c. Thus, the fluorescence SNOM allows one to distinguish each component by choosing the excitation and collection wavelengths. From the comparison of these images, the distribution of 0.1μ BB and 0.1μ YG is shown in Figure 2.5d. It should be noted that in Figure 2.5a, a dark spot appeared at the lower right side of each bright spot like a shadow. These dark spots did not show the real topographic feature of the sample but resulted from a protrusion beside the aperture. On the other hand, the artifact could be eliminated in the fluorescence SNOM images even in the use of the same probe.

The spectroscopic measurements were also carried out for a single latex particle. The aperture was fixed on a latex bead and the fluorescence was guided to a spectrometer. Figure 2.6 shows the fluorescence spectra for the single beads of 0.1μ YG and BB. These spectra were in good agreement with the fluorescence spectra obtained by a conventional spectrometer in the far-field measurement, i.e., with the ensemble average spectra for a number of particles.

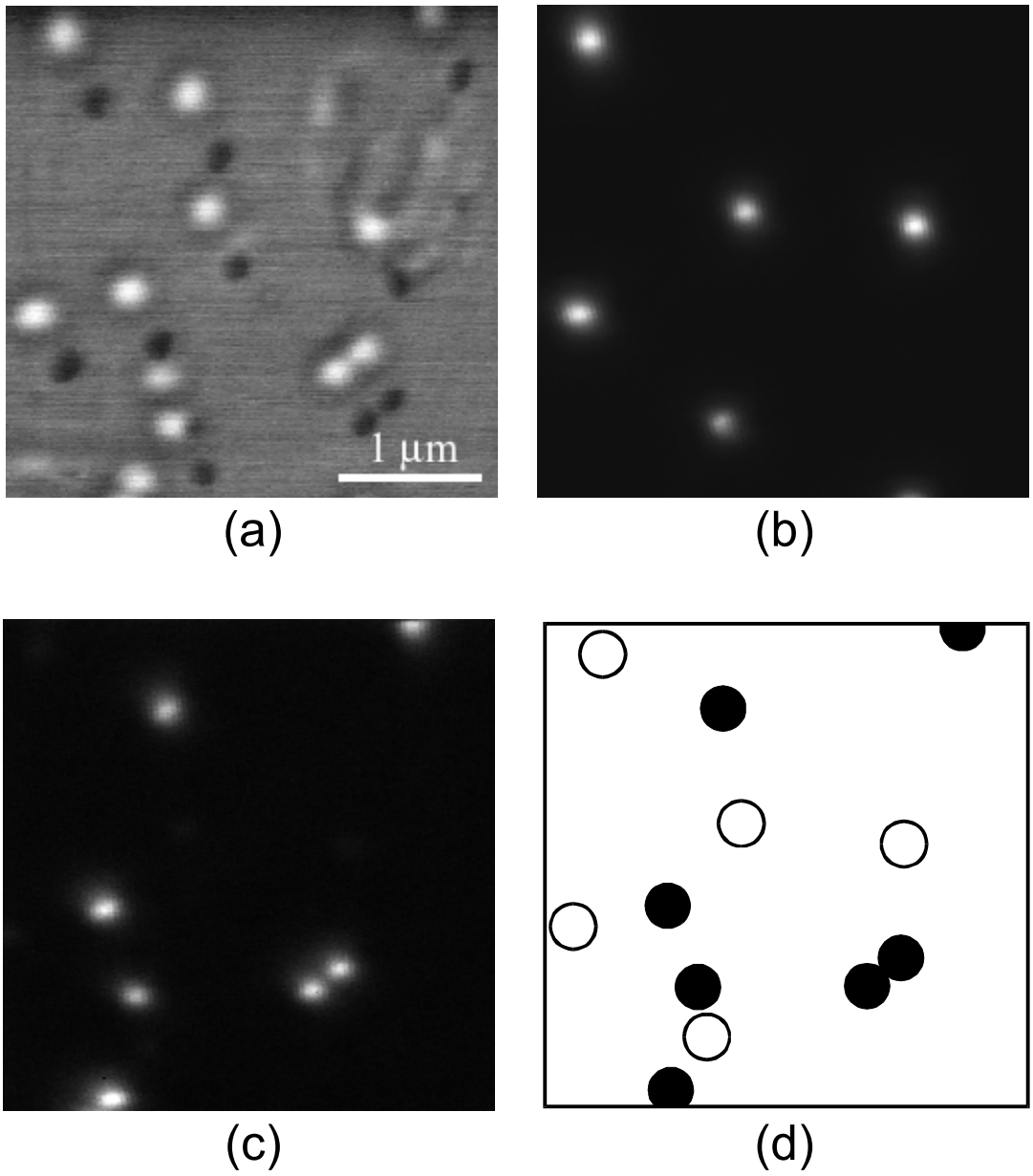

Figure 2.5. Transmission (a), green fluorescence (b), and blue fluorescence (c) SNOM images for the latex particles dispersed on a glass substrate, and the schematic illustration for the distribution of 0.1μ BB and 0.1μ YG, which are indicated as closed and open circles, respectively (d). The transmission image was recorded at 442 nm. The green fluorescence image was obtained by collecting the fluorescence of $\lambda > 460$ nm from the latex particles excited at 442 nm. The blue fluorescence image was obtained by detecting the fluorescence at 360 – 400 nm with 325-nm illumination.

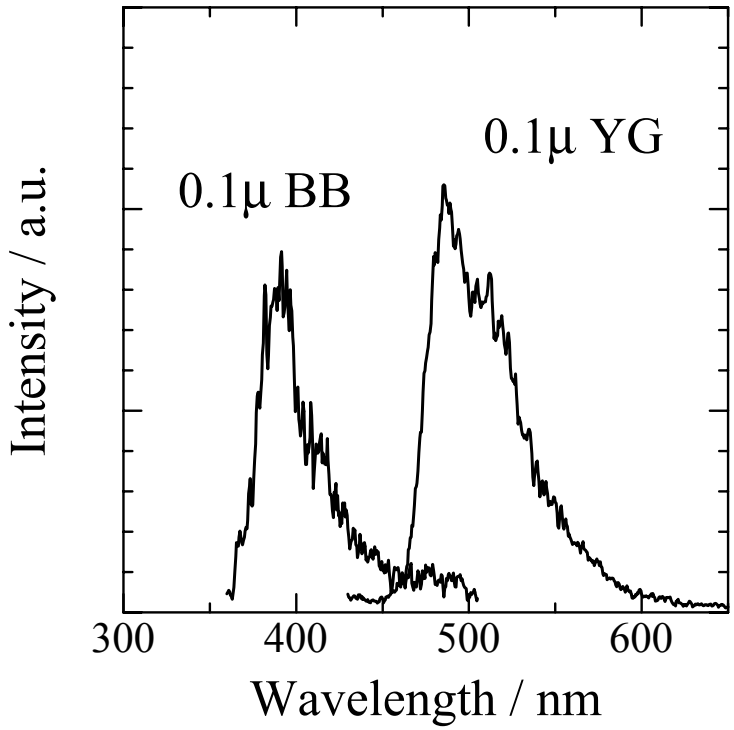

Figure 2.6. Fluorescence spectra for the individual particles of the fluorescent latex 0.1μ BB and 0.1μ YG. The excitation wavelengths for 0.1μ BB and 0.1μ YG were 325 and 415 nm, respectively.

2.3.3. Nano-Photorecording on Polymer Monolayer

The optical near-field has a high energy density since the incident light is confined in a small area at the tip end. Therefore, SNOM is able to bring about photochemical reactions in a local area if the specimen contains reactive species at the surface. The near-field technique has a potential of photopatterning with an extremely high spatial resolution.[8-10] In this study, pyrene was used as a photoreactive compound. A monolayer of the pyrene-labeled PiBMA was deposited on a glass substrate. The 325-nm line of the He-Cd laser with a power of 5 mW was coupled into the fiber probe, and the "line art" was drawn on a "canvas" with the SNOM probe.

The written lines were measured by the fluorescence SNOM, imaged at the same excitation wavelength with a laser power of 2 mW at the cleaved end of the fiber probe. Since pyrene is bleached by the intense irradiation of UV light, the fluorescence intensity on the line becomes weak compared to the non-irradiated area. Figure 2.7 shows the Japanese Kanji letters meaning "Near-Field" and a typical profile of fluorescence intensity across the written line. The full width at half maximum (fwhm) for the line was 170 nm. The observed line width in the fluorescence image is determined by the convolution of the actual structure and the instrument function which is approximately given by the aperture size (~ 100 nm), i.e., the optical near-field distribution at the sample surface. Hence, the real width for the written structure is expected to be finer than the observed width. Since the writing and imaging were carried out sequentially with the same tip, it is reasonable to say that the instrument function has the same profile for the writing and reading processes. Assuming that the instrument function is approximated to be Gaussian, the width for the written structure was estimated to be 120 nm.[10] The light emanating from the aperture spreads out with the increase of the distance from the aperture. Hence, in order to obtain a higher resolution, the dye should be closer to the aperture. In this study, the pyrene molecules were placed in the ultra-thin layer of PiBMA with a thickness of 1 nm, therefore, they existed only in the vicinity of the aperture. The well-controlled and uniform placement of pyrene dyes are also attributed to the high resolution patterning. Besides the thinness, polymer monolayers have high thermal stability and fewer defects compared to the monolayers of low molecular weight amphiphilic materials.[25,26] Therefore, it can be said that the dye-labeled polymer monolayer is one of the suitable materials for the photopatterning with a high spatial resolution.

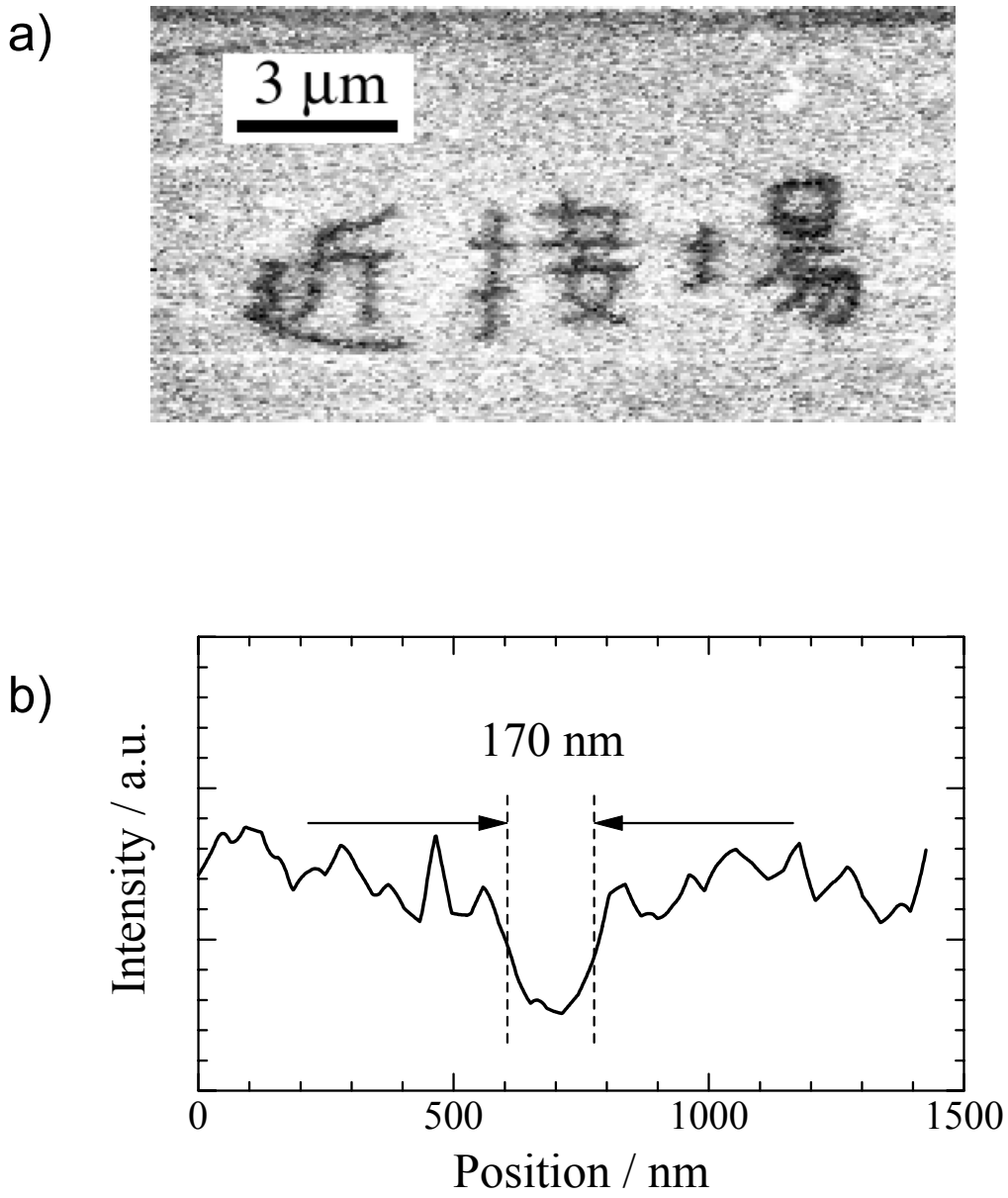

Figure 2.7. "Near-Field" written in Japanese Kanji characters (a) and fluorescence intensity profile (b).

2.3.4. Single Macromolecule Detection

The first observation of single chains of a synthetic polymer was performed by Kumaki et al.[27] They directly observed the conformation of polystyrene-*block*-poly(methyl methacrylate) chain with the atomic force microscopy (AFM). In their experiment, the single polymer chain was isolated on a mica surface in an extremely dilute condition, and it was kept in a humid atmosphere to take an elongated conformation. The height difference between the adsorbed chain and the mica surface was recorded by AFM, and it showed a specific conformation of the polymer chain lying on the substrate. SNOM is able to probe the spatial distribution of fluorescent molecules not only at the surface but also in the bulk, by using the optical near-field

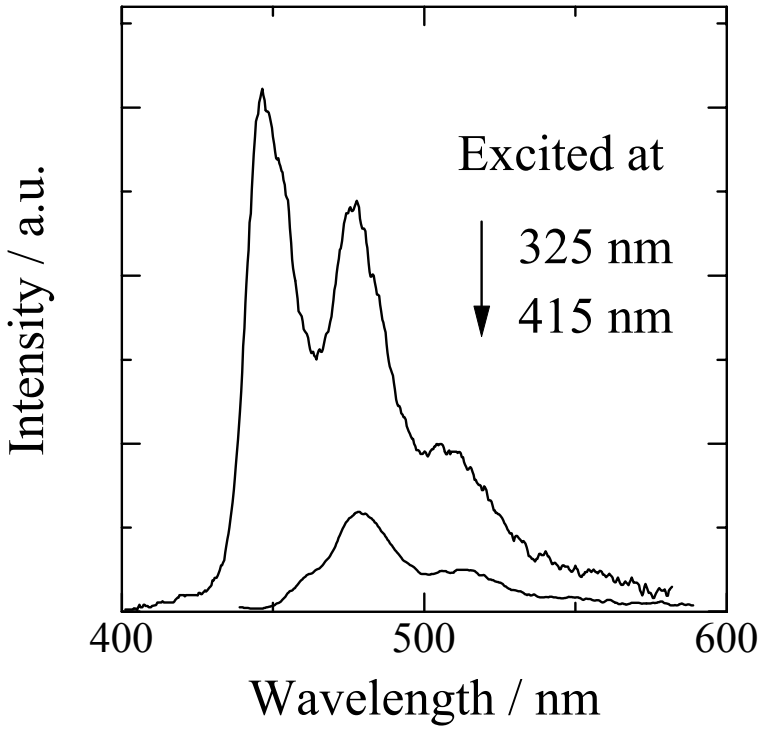

Figure 2.8. Far-field fluorescence spectra for a PiBMA-Pe monolayer on PiBMA-Cz. The excitation wavelengths were 415 and 325 nm.

which penetrates under the surface. Therefore, a single chain as deposited in a film could be visualized in a SNOM image when the polymer chains are labeled with fluorescent dyes. The single molecule fluorescence experiment needs a 'bright' dye such as carbocyanine and rhodamine,[28-31] which have large absorption coefficients, high quantum yields, and strong durability against photobleaching. These dyes are ionic and insoluble in organic solvents so that it is impossible to introduce them covalently to the side group of methacrylate polymers. In this study, the PiBMA was labeled with perylene (PiBMA-Pe). The absorption coefficient of perylene is not so large as that of cyanine or rhodamine dye. Therefore, it is desirable to increase the excitation probability under a given optical field and enhance the fluorescence intensity from perylene. Carbazole was employed to sensitize the perylene fluorescence because the emission band of carbazole has a large overlap with the absorption band of perylene, yielding the efficient energy transfer from carbazole to perylene. Figure 2.8 shows the far-field fluorescence spectra for a monolayer of PiBMA-Pe deposited onto a PiBMA-Cz triple layer. These spectra were obtained for the same sample, but with the different excitation wavelengths of 325 and 415 nm, at which carbazole and perylene were selectively excited, respectively. In the spectrum with 415-nm excitation, the 0-0 band of perylene emission was remarkably depressed because it was recorded through the same filters as those in the SNOM measurement, in which a long-pass filter (> 460 nm) must be incorporated in order to block the strong excitation light at 415 nm. On the other hand, the intensity of the perylene fluorescence with the 325-nm excitation was much larger than that with the 415-nm excitation. Under the 325-nm illumination, the absorbed energy on carbazole can migrate among many carbazolyl groups, and finally transfers to a perylene molecule. This is a kind of light harvesting system in which a perylene can collect photon energies from a number of surrounding carbazole molecules. Consequently, the fluorescence intensity under the excitation of carbazole was much larger than that under the 415-nm illumination.

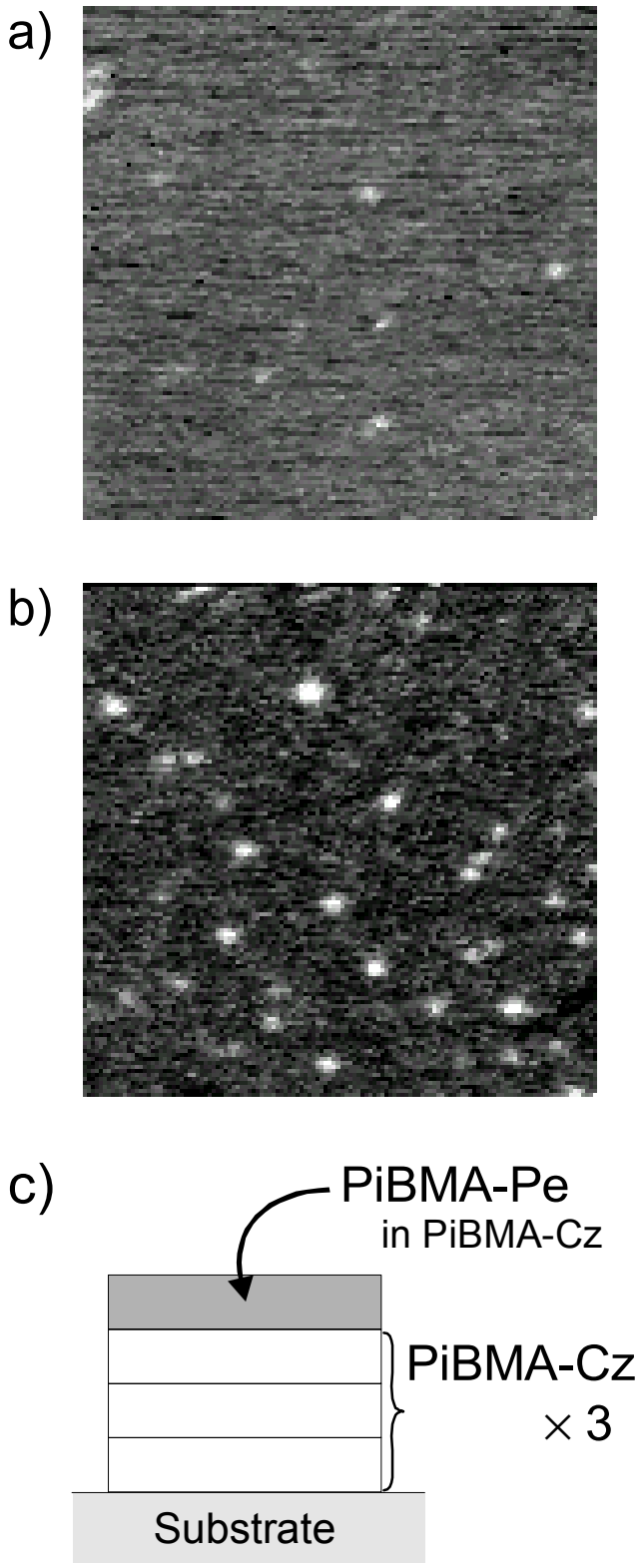

Figure 2.9. Fluorescence SNOM images for single perylene-labeled poly(isobutyl methacrylate) chains obtained by collecting the perylene fluorescence (7.5 × 7.5 μm^2). The excitation wavelength were 415 nm (a) and 325 nm (b). The fraction of PiBMA-Pe was 0.33 % by the occupation area. Figure (c) indicates the layer structure for the sample film.

Figure 2.9 shows the perylene fluorescence SNOM images for the PiBMA-Pe chains and the schematic illustration for the layer structure of the specimen. The fraction of PiBMA-Pe was 0.33 % in the occupation area. Figures 2.9a and 2.9b depict the SNOM images with the excitation wavelengths of 415 nm and 325 nm, respectively. In the latter, the signal-to-noise ratio was improved from 2.6 to 7.9 by the sensitization of the perylene fluorescence. As mentioned above, the sensitization mechanism was based on the excitation energy migration among carbazole moieties and the energy transfer from carbazole to perylene. It should be noted that the diffusion of the excitation energy may degrade the spatial resolution of the fluorescence image obtained with SNOM. However, the energy diffusion length was evaluated to be less than 10 nm.[12] Hence, it can be said that the reduction of the resolution is almost negligible compared with the spatial resolution of SNOM (~ 100 nm).

Next, we discuss if the bright spots in Figure 2.9 actually show single polymer chains in the PiBMA monolayer. For the multi-chromophoric system, it is difficult to measure the discrete jump of the fluorescence intensity, which is usually observed as a proof of the single molecule detection.[31-33] Instead, for the monolayer sample, the area density of the dispersed PiBMA-Pe chain is quantitatively determined from the occupation area for a single chain and the fraction of PiBMA-Pe in PiBMA-Cz. Because the occupation area for a monomer unit and the number-averaged degree of polymerization are 0.28 nm^2 and 1.9×10^4, respectively, the area occupied by a single PiBMA-Pe chain is estimated to be 5,300 nm^2. For example, when the fraction of PiBMA-Pe is 0.1 %, the number of PiBMA-Pe chains per unit area is estimated to be 0.20 μm^{-2}. Figure 2.10 shows the relationship between the observed and calculated area densities of the fluorescence spot. The observed density of the spot was slightly smaller than the calculated density on the assumption that the single PiBMA-Pe chains were dispersed individually. This difference probably comes from the fact that the molecular weight dispersion for PiBMA-Pe is 1.25. This means that PiBMA-Pe

contains the polymer chains with a wide range of molecular weights of $5 \times 10^5 - 1 \times 10^7$. Therefore, a part of the low molecular weight component could not be detected in Figure 2.9b due to the small amount of dye molecules for a single chain. However, the difference between the observed and calculated densities was small, so it can be said that the fluorescence spots observed in Figure 2.9 indicate individual PiBMA chains.

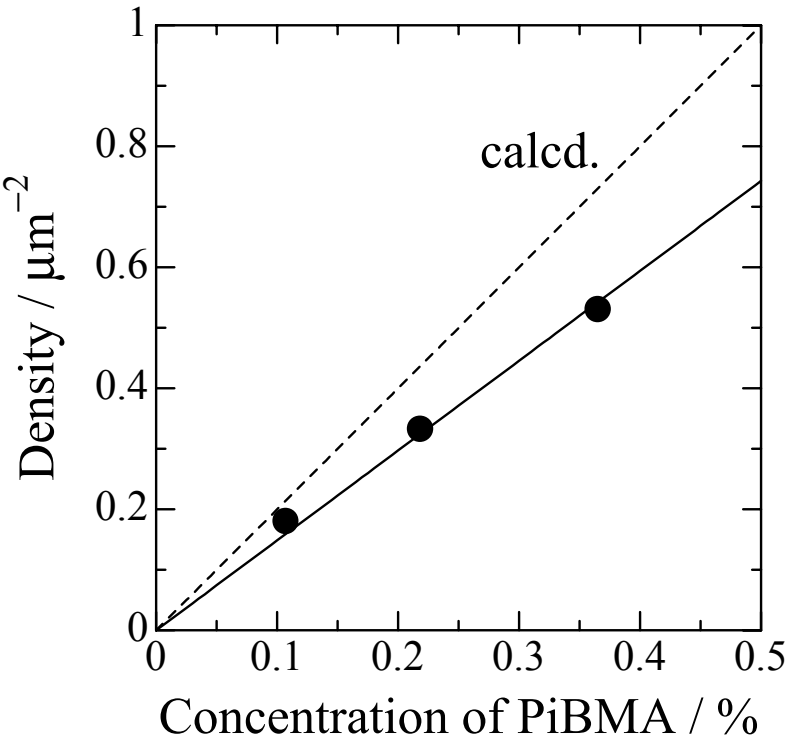

Figure 2.10. Relationship between the calculated (broken line) and measured area density (closed circles) of perylene-labeled polymer chains.

Finally, we discuss the conformation of a PiBMA-Pe chain in the monolayer. The average contour length for the PiBMA-Pe chain was estimated to be about 5 μm from the degree of polymerization of 1.9×10^4 and the unit length of ca. 0.25 nm. If the PiBMA-Pe chain took an expanded form, it should be observed as a long fluorescent string in the SNOM image with a spatial resolution of 100 nm. The PiBMA-Pe chains were actually observed as circular spots with a small diameter of $\lesssim$ 200 nm. Therefore, it can be said that the PiBMA chain was not elongated but took a rather contracted form in the monolayer.[34,35]

2.4. CONCLUSION

Scanning near-field optical microscopy operated with an ultra-violet laser (UV-SNOM) was developed and applied to polymer systems. UV-SNOM enabled one to perform spectroscopic measurements in a local area with a high spatial resolution beyond the diffraction limit of light. This chapter demonstrated the versatility of UV-SNOM for studying the nanometric structure of polymer systems. i) A mixture of two kinds of the nano-sized particles labeled with different dyes were measured by SNOM. Whereas the topographic measurement could not distinguish them, they were identified one by one through the spectroscopic measurement. ii) UV-SNOM is able to provide a high photon energy through a subwavelength-sized aperture and bring about photochemical reactions in a nanometric area. Applying this characteristic of SNOM, we demonstrated photorecording/reading on a dye-labeled polymer monolayer. The width of the written line was ca. 120 nm, which is beyond the diffraction limit. iii) The high detection sensitivity of SNOM allowed the observation of fluorescence from a single polymer chain. The weak fluorescence from a individual polymer chain was efficiently enhanced with the UV excitation, resulting in the single macromolecule

imaging with a high signal-to-noise ratio. Thus, in addition to imaging nano-structure of polymeric materials, UV-SNOM is a powerful tool for nanometric chemical analysis, nano-fabrication, and also for probing molecular information through fluorescence spectroscopy.

References

1. E. Betzig and J. K. Trautman, *Science*, **257**, 189 (1992).
2. M. Ohtsu, "Near-Field Nano/Atom Optics and Technology," Springer, Tokyo, 1998.
3. B. Hecht, B. Sick, U. P. Wild, V. Deckert, R. Zenobi, O. J. F. Martin, and D. W. Pohl, *J. Chem. Phys.*, **112**, 7761 (2000).
4. N. F. van Hulst, J. A. Veerman, M. F. Garcia-Parajo, and L. Kuipers, *J. Chem. Phys.*, **112**, 7799 (2000).
5. T. Ha, T. Enderle, D. F. Ogletree, D. S. Chemla, P. R. Selvin, and S. Weiss, *Proc. Natl. Acad. Sci. USA*, **93**, 6264 (1996).
6. J. Kerimo, D. M. Adams, P. F. Barbara, D. M. Kaschak, and T. E. Mallouk, *J. Phys. Chem. B*, **102**, 9451 (1998).
7. R. Zenobi and V. Deckert, *Angew. Chem. Int. Ed.*, **39**, 1746 (2000).
8. S. Davy and M. Spajer, *Appl. Phys. Lett.*, **69**, 3306 (1996).
9. D. P. Tsai and W. R. Guo, *J. Vac. Sci. Technol. A*, **15**, 1442 (1997).
10. A. Naber, T. Dziomba, U. C. Fischer, H. -J. Maas, and H. Fuchs, *Appl. Phys. A*, **70**, 227 (2000).
11. S. Ito, H. Okubo, S. Ohmori, and M. Yamamoto, *Thin Solid Films*, **179**, 445 (1989).
12. S. Ito, S. Ohmori, and M. Yamamoto, *Macromolecules*, **25**, 185 (1992).
13. H. Sakai, A. Itaya, H. Masuhara, K. Sasaki, and S. Kawata, *Polymer*, **37**, 31 (1996).
14. K. Zachariasse and W. Kuhnle, *Z. Phys. Chem. N. F.*, **101**, 267 (1976).
15. T. Kanaya, K. Goshiki, M. Yamamoto, and Y. Nishijima, *J. Am. Chem. Soc.*, **104**, 3580 (1982).
16. S. Ito, M. Yamamoto, and Y. Nishijima, *Bull. Chem. Soc. Jpn.*, **54**, 35 (1981).

17. A. Tsuchida, Y. Tsujii, S. Ito, M. Yamamoto, and Y. Wada, *J. Phys. Chem.*, **93**, 1244 (1989).
18. H. Aoki, Y. Sakurai, S. Ito, and T. Nakagawa, *J. Phys. Chem. B*, **103**, 10553 (1999).
19. S. Mononobe, T. Saiki, T. Suzuki, S. Koshihara, and M. Ohtsu, *Opt. Commun.*, **146**, 45 (1998).
20. M. Arai, S. Koshihara, M. Ueda, M. Yoshimoto, T. Saiki, S. Mononobe, M. Ohtsu, T. Miyazawa, and M. Kira, *J. Luminescence*, **87-89**, 951 (2000).
21. K. Naito, *J. Colloid Interface Sci.*, **131**, 218 (1989).
22. L. Novotny, D. W. Pohl, and B. Hecht, *Opt. Lett.*, **20**, 970 (1995).
23. B. Hecht, H. Bielefeldt, Y. Inouye, D. W. Pohl, and L. Novotny, *J. Appl. Phys.*, **81**, 2492 (1997).
24. H. Aoki, S. Tanaka, S. Ito, and M. Yamamoto, *Macromolecules*, **33**, 9650 (2000).
25. S. Ito, K. Kawano, M. Mabuchi, and M. Yamamoto, *Polym. J.*, **28**, 164 (1996).
26. M. Mabuchi, K. Kawano, S. Ito, M. Yamamoto, M. Takahashi, and T. Masuda, *Macromolecules*, **31**, 6083 (1998).
27. J. Kumaki, Y. Nishikawa, and T. Hashimoto, *J. Am. Chem. Soc.*, **118**, 3321 (1996).
28. A. G. T. Ruiter, J. A. Veerman, M. F. Garcia-Parajo, and N. F. van Hulst, *J. Phys. Chem. A*, **101**, 7318 (1997).
29. J. A. Veerman, M. F. Garcia-Parajo, L. Kuipers, and N. F. van Hulst, *J. Microscopy*, **194**, 477 (1999).
30. C. W. Hollars and R. C. Dunn, *J. Phys. Chem.*, **112**, 7822 (2000).
31. E. Betzig and R. Chichester, *Science*, **262**, 1422 (1993).
32. X. S. Xie and R. C. Dunn, *Science*, **265**, 361 (1994).
33. J. A. Veerman, M. F. Garcia-Parajo, L. Kuipers, and N. F. van Hulst, *Phys. Rev. Lett.*, **83**, 2155 (1999).

34. P. G. de Gennes, “Scaling Concepts in Polymer Physics,” Cornell University Press, Ithaca, New York, 1979.

35. N. Sato, Y. Osawa, S. Ito, and M. Yamamoto, *Polym. J.*, **31**, 488 (1999).

Chapter 3

PHASE SEPARATION STRUCTURE OF A MONOLAYER OF BINARY POLYMER BLEND STUDIED BY SCANNING NEAR-FIELD OPTICAL MICROSCOPY

3.1. INTRODUCTION

Recently, polymer monolayers, which are prepared at the air/water interface, have attracted much attention because the sequential deposition of them by the Langmuir-Blodgett (LB) technique allows one to fabricate highly controlled molecular assemblies. Mobility and conformation of a polymer chain in a monolayer is thought to be extremely constrained, considering that the polymer chain is confined into a two-dimensional plane from a random-coil conformation in a three-dimensional space.[1-4] Thus, it is expected that the properties of polymer monolayers are different from those of polymers in bulk.

Our research project is concerned with "polymer science in two dimensions," and we have so far investigated the properties of polymer monolayers by various optical techniques, such as Brewster angle microscopy[5,6] and fluorescence spectroscopy.[7,8] However, the lateral resolution is not sufficient to observe microscopic structures due to the diffraction limit ($\lambda/2$) of conventional optical methods. Scanning near-field optical microscopy (SNOM) allows one to obtain a fluorescence micrograph with a high resolution beyond the diffraction limit.[9,10] As described in the previous chapter, SNOM has the advantage of the capability to perform spectroscopic measurements in a

nanometric area, and other several studies have shown that SNOM is a versatile tool for studying both the morphology and the spectroscopic properties of an organic thin film simultaneously.[11-15]

The current chapter is concerned with a two-dimensionally phase-separated polymer blend. The phase separation of polymer blends in three-dimensional space has been extensively studied by many workers.[16-18] However, little is known about that of polymers restricted in a two-dimensional plane.[19,20] We investigated the phase separation structure of a binary polymer blend which consists of poly(isobutyl methacrylate) (PiBMA) and poly(octadecyl methacrylate) (PODMA). The structure of the completely phase-separated monolayer was measured by a fluorescence SNOM with a resolution of ca. 100 nm using UV and visible lasers as light sources. The excitation energy transfer method from pyrene to perylene was applied to investigate the mixing of these polymers at the phase interface.

3.2. EXPERIMENTS

3.2.1. Materials

Pyrene-labeled poly(isobutyl methacrylate) (PiBMA-Py) was synthesized by the radical copolymerization of isobutyl methacrylate and 1-pyrenylmethyl methacrylate. The molecular weight was determined by GPC calibrated with polystyrene standards. The fraction of pyrene moiety introduced into the polymer chain, *f*, was estimated from UV-Vis absorption (U3500, Hitachi) and ^{1}H-NMR (JNM-EX400, JEOL) measurements. Perylene-labeled poly(octadecyl methacrylate) (PODMA-Pe) was synthesized from octadecyl methacrylate and 3-perylenylmethyl methacrylate, and characterized similarly to PiBMA-Py. The chemical structures and the characterization of the polymers are shown in Figure 3.1 and Table 3.1, respectively.

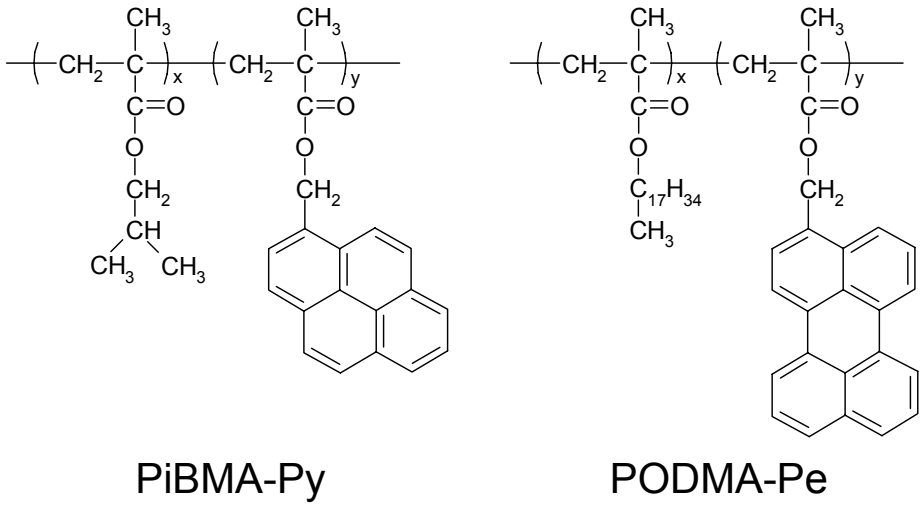

Figure 3.1. Chemical structures of pyrene-labeled poly(isobutyl methacrylate) (PiBMA-Py) and perylene-labeled poly(octadecyl methacrylate) (PODMA-Pe).

Table 3.1. Characterization of PiBMA-Py and PODMA-Pe

	$M_n \times 10^{-3}$	M_w/M_n	f / %
PiBMA-Py	39,600	2.05	2.9
PODMA-Pe	11,900	2.08	2.0

Phase-separated monolayers of the PiBMA-Py / PODMA-Pe blend were prepared by the following procedure. A mixed solution of PiBMA-Py and PODMA-Pe (50:50) was spread dropwise onto a subphase of purified water (Barnstead NANO Pure II) at 20 °C. The temperature of the subphase was raised to 40 °C and kept constant for 60 min for complete phase separation of PiBMA-Py / PODMA-Pe blend on a water surface. After cooling to 20 °C, the phase-separated monolayer was compressed and transferred onto a clean cover glass.

3.2.2. Measurements

Fluorescence SNOM images were recorded on a commercially available instrument (SP-301, Unisoku). The 325 and 442-nm lines of a He-Cd laser (IK5351R-D, Kimmon Electric) were used as the excitation light. The distance between a probe and a sample surface was regulated to be several nanometers by a shear force feed-back system. The fluorescence from the sample was collected by a high NA objective and detected with a photomultiplier (R2949, Hamamatsu Photonics). SNOM probes used in this study were made from an optical fiber with a pure silica core by etching in a buffered hydrogen fluoride solution following a heating-and-pulling process (P-2000, Sutter Instrument).[21,22] The lateral resolution of our system is typically 50 – 100 nm. Measurements were performed at room temperature, and no image processing was applied. In our SNOM system, the vertical resolution of a topographic image, which is typically 1 nm, is rather worse than a commercially available AFM. Therefore, contact mode AFM (SPM-9500J, Shimadzu) measurements were also carried out to probe the height difference between PiBMA-Py and PODMA-Pe domains. The spring constant of the cantilever (OMCL-TR400PSA-3, Olympus) was 0.09 N m^{-1}.

3.3. RESULTS AND DISCUSSION

3.3.1. AFM Measurement

A contact mode AFM image is shown in Figure 3.2. The bright and dark areas correspond to PODMA and PiBMA domains, respectively. The height difference between these areas was 2 nm, which was in good agreement with the thickness difference between PODMA[23] and PiBMA[24,25] monolayers reported in the literature. This indicates that the polymer blend spread on water surface was able to be transferred

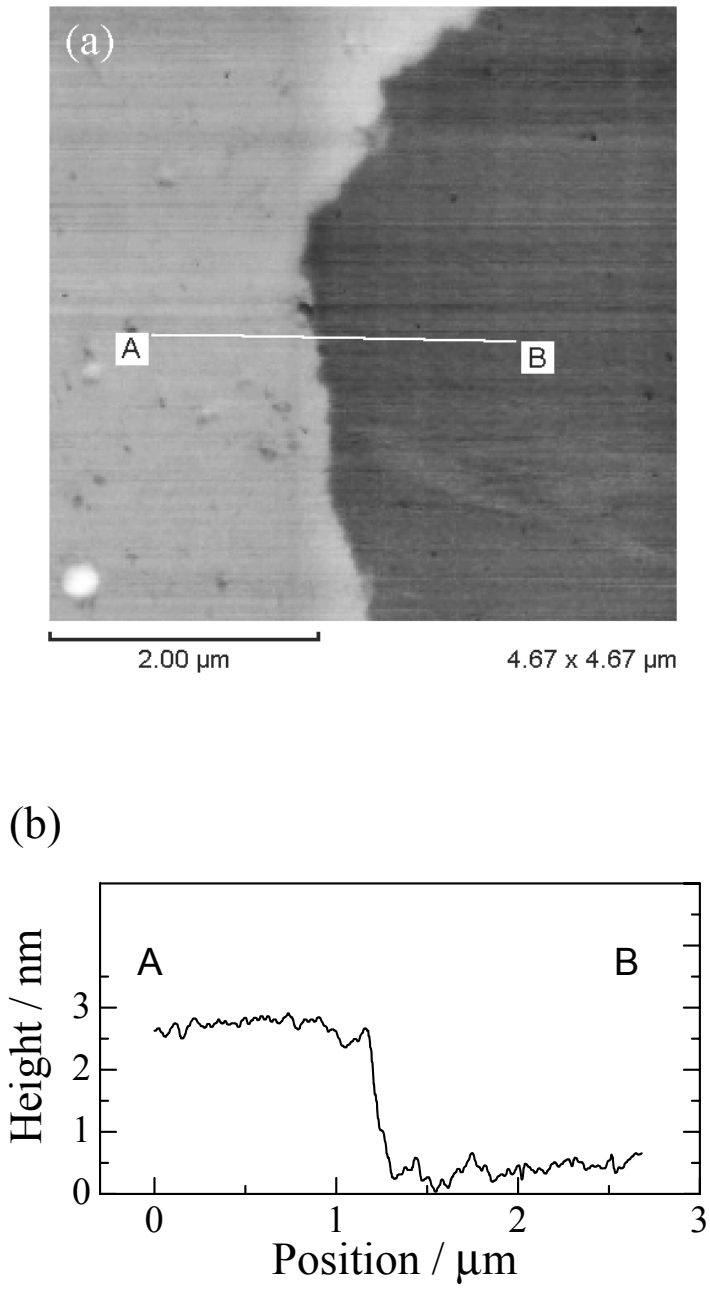

Figure 3.2. AFM image of a phase-separated monolayer (a) and the height profile along the line indicated in the AFM image (b).

onto a solid substrate as a monolayer.

3.3.2. Fluorescence SNOM Image

Figure 3.3 shows the fluorescence SNOM images of a phase-separated monolayer deposited at a surface pressure of 5 mN m^{-1}. A perylene fluorescence image is shown in Figure 3.3a, which was recorded by collecting the fluorescence from perylene excited at 442 nm. The bright area indicates PODMA-Pe rich phase because perylene was introduced into only the PODMA chain. Figure 3.3b shows a pyrene fluorescence SNOM image obtained by illumination with a 325-nm evanescent field and collection of the monomer fluorescence (360 – 410 nm) from pyrene. PiBMA-Py rich phase could be visualized as a bright area in the image of pyrene fluorescence. The PiBMA and PODMA domains in a two-dimensional phase-separated polymer blend were able to be selectively imaged by choosing appropriate excitation wavelengths. These two fluorescence SNOM images have complementary features, that is, the bright areas in the pyrene fluorescence image (Figure 3.3b) exactly coincide with the regions which were darkly measured in the perylene fluorescence image (Figure 3.3a). This indicates that the phase-separated monolayer was able to be transferred on the solid substrate without any defect.

3.3.3. Energy Transfer SNOM Image

The energy transfer method was combined with the fluorescence SNOM measurement in order to investigate the phase separation structure in more detail. The excitation energy transfers from a donor (pyrene) to an acceptor (perylene) when they are close to each other. The energy transfer efficiency is very sensitive to the alteration of the distance between the donor and the acceptor, and the Förster radius of a pyrene-perylene pair, at which the energy transfer efficiency is 50 %, is known to be

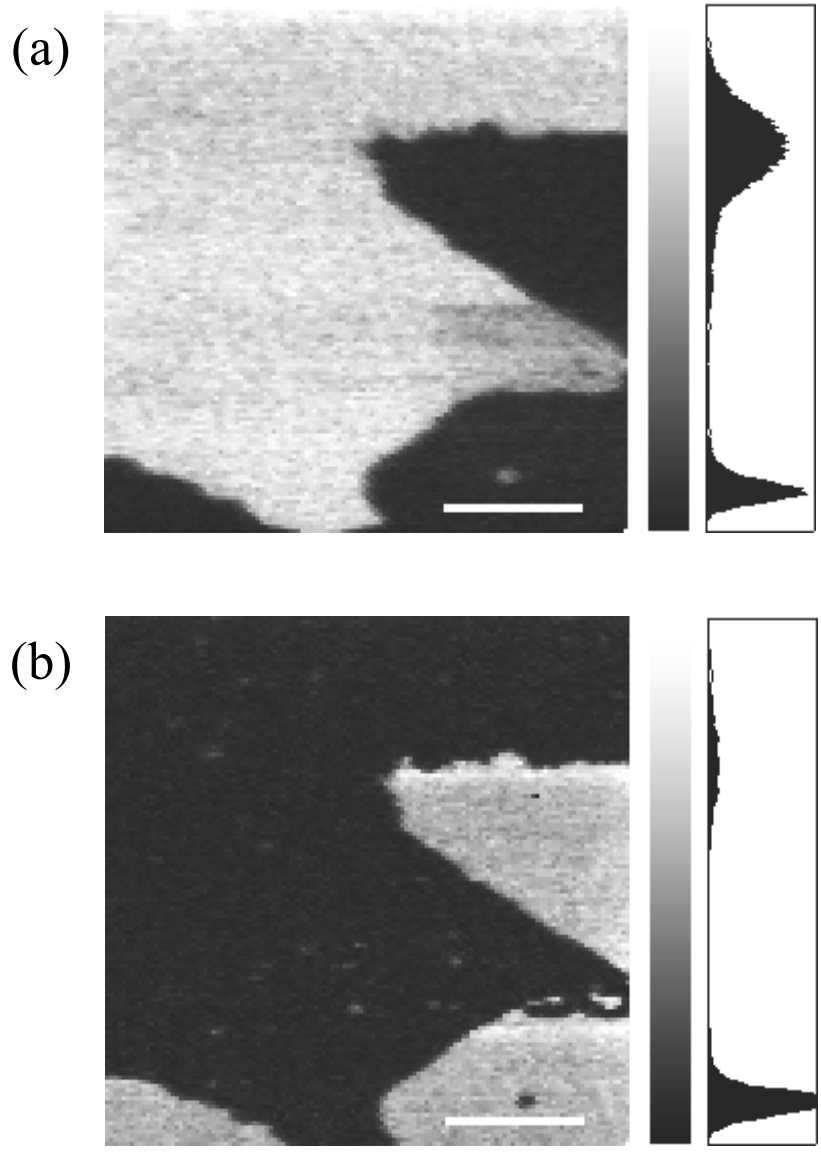

Figure 3.3. Fluorescence SNOM images of a phase-separated polymer monolayer. The scanning area was 15 × 15 μm^2. The scale bar in each image indicates 4 μm. (a) Perylene fluorescence SNOM image. The excitation wavelength was 442 nm and the fluorescence from perylene was collected through a filter, Y-47 (Hoya). (b) Pyrene fluorescence SNOM image. The excitation wavelength was 325 nm. A filter, UV-D33S (Toshiba), was put in front of the detector to collect only the fluorescence from pyrene. The fluorescence intensity histogram for each image is shown in the right hand side, which is the plot of the number of data points against the observed fluorescence intensity.

3.3 nm.[26] Therefore, when pyrene is selectively excited and the perylene emission is recorded with raster-scanning the probe, the bright areas in the image obtained indicate the regions where PiBMA-Py and PODMA-Pe are mixed at the molecular level.

The energy transfer image is shown in Figure 3.4, which was obtained by scanning the same area as that in Figure 3.3 and collecting the fluorescence from perylene (λ > 440 nm) with 325-nm illumination. In this image, only the phase boundary was recorded as a bright area. This indicates that PiBMA and PODMA are mixed at the interface. A fluorescence intensity profile at the interface is shown in Figure 3.5. The typical value of the interface width was 200 – 400 nm, which was

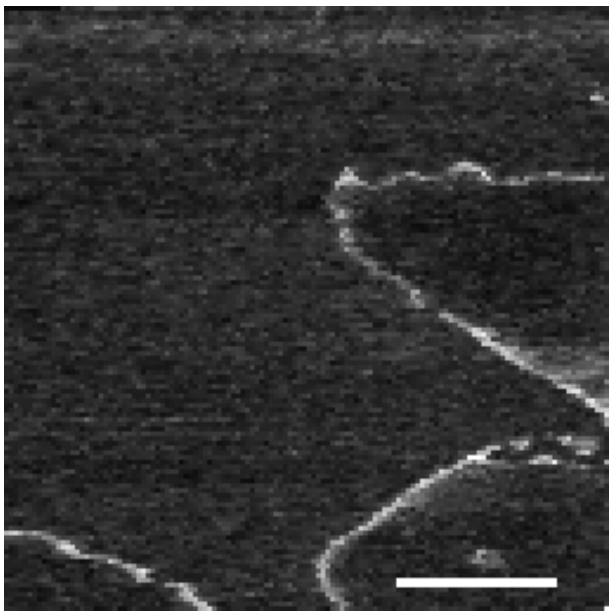

Figure 3.4. Energy transfer image of a phase-separated monolayer. The scanning area was the same as that of Figure 3.3. The scale bar in the image indicates 4 μm. The excitation wavelength was 325 nm. An optical filter, Y-44 (Hoya), was used to block the fluorescence from pyrene and collect only that from perylene. The bright areas in this image indicate the regions where PODMA-Pe and PiBMA-Py were mixed at the molecular level.

defined as the fwhm of a fluorescence intensity profile across the phase boundary. Considering that the lateral resolution of SNOM used in this study was about 100 nm, the real width could be estimated to be 100 – 300 nm. The interface thickness in the bulk state was estimated to be several nanometers from Broseta's theory[27] by using a calculated χ parameter.[28,29] The interface width between PiBMA and PODMA domains observed in quasi-two dimensions was considerably large compared to the value calculated in the three-dimensional state. Although the morphology of the boundary was influenced by the physical factors, such as shear flow and stress, during the compression process after the annealing, the interfacial width was independent of the surface pressure at deposition (data are not shown). This result suggests that the wide line of the phase boundary is determined by the miscibility between PiBMA and PODMA on the surface, rather than the effect of the compression on the water surface.

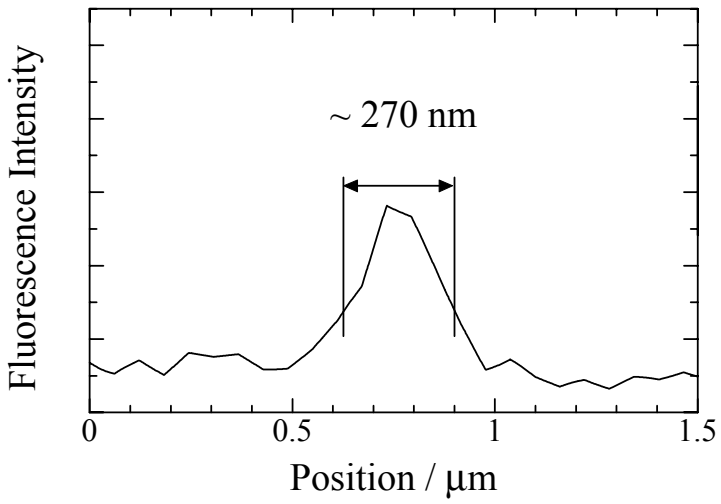

Figure 3.5. Typical fluorescence intensity profile of the phase interface. The interface width was ca. 270 nm.

The fluorescence intensity in the energy transfer image stayed almost at the background level when measured inside of each domain. Little PiBMA existed in the PODMA rich domain, namely $\varphi_{PiBMA} \sim 0$ and $\varphi_{PODMA} \sim 1$, where φ_A is the composition of the polymer A. The fluorescence intensity histogram for each SNOM image in Figure 3.3 has two clearly distinct levels, that is, the fluorescence intensity level was almost constant within each domain. These results indicate that the polymer composition, φ_{PiBMA} and φ_{PODMA}, in each phase reached the equilibrium values and almost completely phase-separated within 60 min during annealing at 40 °C.

3.4. CONCLUSION

The phase separation structure of a binary polymer blend restricted in a two-dimensional plane was investigated by using a fluorescence SNOM. PiBMA-Py and PODMA-Pe domains were selectively imaged by UV and visible lasers, respectively. The topographic image drawn by the excitation energy transfer efficiency revealed that the phase separation of the PiBMA / PODMA blend at the air/water interface was almost completed within 60 min at 40 °C and the phase boundary width was a few hundred nanometers.

The fluorescence method, such as the energy transfer method, in combination with SNOM is expected to be a powerful tool for investigating the morphology and properties of polymers in a two-dimensional plane.

References

1. P. G. de Gennes, "Scaling Concepts in Polymer Physics," Cornell University Press, Ithaca, New York, 1979.
2. R. Vilanove, D. Poupinet, and F. Rondelez, *Macromolecules*, **21**, 2880 (1988).
3. D. Poupinet, R. Vilanove, and F. Rondelez, *Macromolecules*, **22**, 2491 (1989).
4. M. Kawaguchi, A. Yoshida, and A. Takahashi, *Macromolecules*, **16**, 956 (1983).
5. N. Sato, S. Ito, and M. Yamamoto, *Polym. J.*, **28**, 784 (1996).
6. N. Sato, S. Ito, and M. Yamamoto, *Macromolecules*, **31**, 2673 (1998).
7. S. Ito, S. Oki, N. Sato, and M. Yamamoto, *Macromolecules*, **29**, 724 (1996).
8. N. Sato, K. Sugiura, S. Ito, and M. Yamamoto, *Langmuir*, **13**, 5685 (1997).
9. E. Betzig and J. K. Trautman, *Science*, **257**, 189 (1992).
10. D. A. Vanden Bout, J. Kerimo, D. A. Higgins, and P. F. Barbara, *Acc. Chem. Res.*, **30**, 204 (1997).
11. M. H. P. Moers, H. E. Gaub, and N. F. van Hulst, *Langmuir*, **10**, 2774 (1994).
12. J. Hwang, L. K. Tamm, C. Bohm, T. S. Ramalingam, E. Betzig, and M. Edidin, *Science*, **270**, 610 (1995).
13. A. K. Kirsch, A. Schaper, H. Huesmann, M. A. Rampi, D. Mobius, and T. M. Jovin, *Langmuir*, **14**, 3895 (1998).
14. J. Kerimo, D. M. Adams, P. F. Barbara, D. M. Kaschak, and T. E. Mallouk, *J. Phys. Chem. B*, **102**, 9451 (1998).
15. A. K. Dutta, P. Vanoppen, K. Jeuris, P. C. M. Grim, D. Pevenage, C. Salesse, and F. C. De Schryver, *Langmuir*, **15**, 607 (1999).
16. L. A. Utracki, "Polymer Alloys and Blends: Thermodynamics and Rheology," Hanser, New York, 1990.
17. T. Hashimoto, M. Takenaka, and H. Jinnai, *J. Appl. Cryst.*, **24**, 457 (1991).
18. M. Takenaka and T. Hashimoto, *J. Chem. Phys.*, **96**, 6177 (1992).

19. T. Yuba, S. Yokoyama, M. Kakimoto, and Y. Imai, *Adv. Mater.*, **6**, 888 (1994).
20. J. Kumaki and T. Hashimoto, *J. Am. Chem. Soc.*, **120**, 423 (1998).
21. G. A. Valaskovic, M. Holton, and G. H. Morrison, *Appl. Opt.*, **34**, 1215 (1995).
22. M. Ohtsu, "Near-Field Nano/Atom Optics and Technology," Springer, Tokyo, 1998.
23. S. J. Mumby, J. D. Swalen, and J. F. Rabolt, *Macromolecules*, **19**, 1054 (1986).
24. K. Naito, *J. Colloid Interface Sci.*, **131**, 218 (1989).
25. S. Ito, S. Ohmori, and M. Yamamoto, *Macromolecules*, **25**, 185 (1992).
26. I. B. Berlman, "Energy Transfer Parameters of Aromatic Compounds," Academic Press, New York, 1973.
27. D. Broseta, G. H. Fredrickson, E. Helfand, and L. Leibler, *Macromolecules*, **23**, 132 (1990).
28. P. A. Small, *J. Appl. Chem.*, **3**, 71 (1953).
29. S. Krause, *J. Macromol. Sci. Rev. Macromol. Chem.*, **C7**, 251 (1972).

Chapter 4

PHASE SEPARATION BEHAVIOR OF POLYMER BLEND MONOLAYER INVESTIGATED BY TIME-RESOLVED SCANNING NEAR-FIELD OPTICAL MICROSCOPY

4.1. INTRODUCTION

Polymer Langmuir-Blodgett (LB) films have been successfully used to control the excitation energy[1-3] and electron[4,5] transfer processes because the LB technique allows one to construct layered structures in a nanometer scale by the sequential deposition of monolayers spread at the air/water interface. The polymer chain in a monolayer is expected to have different properties from those in a three dimensional space[6-8] because of the low degree of freedom for the polymer chain restricted in a two-dimensional plane. The understanding of properties and morphology of polymer monolayers is important to fabricate well-defined assemblies. In the research filed of the two-dimensional polymers, we have been concerned with phase separation of polymer blend monolayers from the viewpoints of not only polymer physics in two dimensions but also application as a self-organizing method[9,10] to control the in-plane structure of nano-fabrics.

Direct observation of the two-dimensional morphology of polymer monolayers has been carried out so far by Brewster angle microscopy (BAM)[7,11] and atomic force microscopy (AFM).[10,12] Scanning near-field optical microscopy (SNOM) is an emerging scanning probe microscopic technique, which illuminates a specimen with the

optical near-field emanating from an aperture much smaller than the wavelength of light.[13-16] Since SNOM allows one to obtain various unique information such as the molecular orientation and the chemical composition of the specimen with a subwavelength spatial resolution, SNOM is expected to be a powerful tool to investigate the two-dimensional morphology of polymer monolayers as well as the other organic systems: lipid monolayers,[17,18] self-assembled films,[19] liquid crystals,[20] and dye aggregates.[21,22]

In Chapter 3, the two-dimensional morphology of the completely phase-separated polymer blend monolayer was studied,[23] which consisted of poly(octadecyl methacrylate) (PODMA) and poly(isobutyl methacrylate) (PiBMA) labeled with perylene and pyrene as the fluorescent dyes, respectively. SNOM allowed us to observe each polymer domain selectively by choosing the excitation wavelength. The phase boundary region could be selectively visualized in the SNOM image by the energy transfer emission, which was detected from the region where both components were molecularly mixed. In the current chapter, the phase separation behavior of the dye-labeled PODMA / PiBMA blend monolayers was studied in more detail by means of SNOM. The annealing time effect on the phase separation structure was examined through the far-field spectroscopy and the energy transfer emission mapping with SNOM. The time-resolved measurements in the near-field were also carried out for the phase-separated monolayers with a temporal resolution of subnanoseconds. The phase separation structure before and after annealing was discussed through the excitation energy transfer dynamics among the dyes introduced to PODMA and PiBMA.

4.2. EXPERIMENTS

4.2.1. Materials

PODMA and PiBMA were labeled at the side-chains with fluorescent dye molecules: pyrene (Py), perylene (Pe), and eosin (Eo). The chemical structures are shown in Figure 4.1. Dye-labeled methacrylate monomers, 1-pyrenylmethyl methacrylate, 3-perylenylmethyl methacrylate, and eosin methacrylate, were synthesized by the esterification of methacryloyl chloride. 1-Pyrenylmethyl methacrylate was synthesized by the following procedure. 1-Pyrenemethanol was prepared by the reduction of 1-pyrenecarboxaldehyde (Aldrich) with $NaBH_4$. Methacryloyl chloride (Tokyo Chemical Industry) was added dropwise to a THF solution of 1-pyrenemethanol and pyridine at 0 °C, and then stirred for 3 h at room temperature. The product was purified by twice recrystallization from ethanol. 3-Perylenylmethyl methacrylate was prepared from 3-perylenemethanol, which was synthesized by the reduction of 3-formylperylene following Vilsmeiyer reaction of perylene. Eosin-labeled methacrylate monomer was synthesized by the esterification of methacryloyl chloride with methyl eosin (Aldrich) in DMF. PiBMA labeled at the side-chains was prepared by copolymerization of isobutyl methacrylate (distilled under a reduced pressure, Nacalai Tesque) and one of the dye-labeled methacrylate monomers. Polymerization was carried out by the free radical polymerization initiated by α, α'-azobisisobutyronitrile (Nacalai Tesque) in toluene at 60 °C for 24 h. PODMA was polymerized from octadecyl methacrylate (recrystallized from acetone, Tokyo Chemical Industry) in the same manner as PiBMA. Polymers were purified by repeated reprecipitation from toluene into methanol. Molecular weight was determined by size exclusion chromatography calibrated with polystyrene standards. The fraction of fluorescent moiety, f, introduced into the polymer chain was estimated from UV-vis absorption (U3500, Hitachi) and 400 MHz ^{1}H-NMR (JNM-EX400, JEOL)

measurements. Characterization of the sample polymers is summarized in Table 4.1.

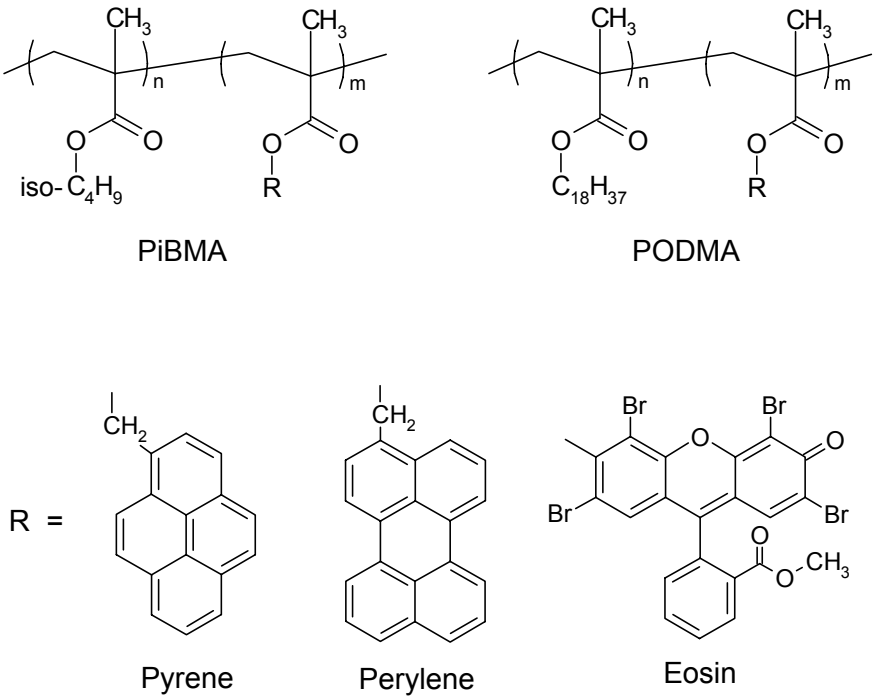

Figure 4.1. Chemical structures of polymers labeled with fluorescent dyes.

Table 4.1. Characterization of Polymers

	$M_n \times 10^{-3}$	M_w/M_n	f / %
PODMA-Pe	11.9	2.08	2.0
PODMA-Py	14.4	1.94	2.3
PiBMA-Pe	45.1	1.56	2.0
PiBMA-Py	39.6	2.05	2.9
PiBMA-Eo	48.8	1.50	2.5

A mixed benzene solution of dye-labeled PiBMA and PODMA (0.1 g L^{-1}) was dropped onto the surface of pure water, which was ion-exchanged, distilled, and treated with a water purification system (Nano Pure II, Barnstead). The composition of PODMA / PiBMA mixture was 1 : 1 by the monomer unit. The subphase temperature was kept at 20 °C when spreading the polymer solution. After evaporation of the solvent, the temperature of the subphase was raised to 40 °C and kept constant for a given duration to anneal the monolayer, and then lowered to 20 °C. The monolayer was compressed up to 5 mN m^{-1}, and then transferred onto a clean cover slip by the vertical dipping method at a rate of 2.0 mm min^{-1}.

4.2.2. Measurements

The SNOM system used in this study was based on a commercially available instrument (SP-301, Unisoku). A CW He-Cd laser (λ = 325 and 442 nm; IK5351R-D, Kimmon Electric) and the second harmonic of a picosecond Ti:sapphire laser (λ = 415 nm; Tsunami, Spectra Physics) were used as the light sources. Commercially available SNOM probes cannot be used for the UV excitation because of the low transmittance and the autofluorescence of the optical fiber core in the UV region. The SNOM probes were made from an optical fiber with a pure silica core by etching in a hydrogen fluoride solution buffered with NH_4F following a heating-and-pulling process (P-2000, Sutter Instrument).[15,24] The cone angle and the radius of curvature at the end of a tip were ca. 60 ° and less than 20 nm, respectively. Then, the side of the probe was metal-coated to prevent the light leakage except for the tip end. The diameter of the aperture was typically 50 – 100 nm. Autofluorescence from the optical fiber core was negligible when the 325-nm line of the He-Cd laser was coupled in. Thus, the use of homemade probes made of a pure silica enabled us to carry out SNOM measurements in the UV region. The distance between the probe and the sample surface was regulated to be several nanometers by a shear force feed-back system.

The fluorescence from the sample was collected by an objective (1.3 NA, Nikon) and detected with a photomultiplier (R4220P, Hamamatsu Photonics). Time-resolved measurement was carried out by the time-correlated single photon counting method.[25] The fluorescence photon signal from the sample and the excitation pulse were fed into a time-to-amplitude converter (TAC; Model 457, Ortec). The time-correlated TAC signals were accumulated at a multichannel analyzer (Ino-Tech 5300, Norland) and transferred to a computer. The fwhm of the instrumental response function was ca. 500 ps. Far-field fluorescence spectra were recorded by a Hitachi 850 spectrophotometer. All measurements were carried out at room temperature.

4.3. RESULTS AND DISCUSSION

4.3.1. Phase Separation Structure Before Annealing

Figures 4.2a and 4.2b show the perylene and pyrene fluorescence SNOM images for the same area of a PODMA-Pe / PiBMA-Py monolayer deposited without annealing process, respectively. These images have complementary features. This indicates that the phase-separated polymer monolayer could be transferred on a substrate without any defect. It is known that the energy transfer from pyrene to perylene, used as fluorescent dyes in this sample, occurs efficiently. Because the Förster radius for the pyrene-perylene pair is 3.3 nm and the energy transfer efficiency steeply decreases with the increase in the separation distance between the donor and the acceptor,[26] the energy transfer emission is detected only from the region where PODMA-Pe and PiBMA-Py were mixed at the molecular level. The spatially resolved energy transfer measurement by SNOM will provide further insight into the phase separation structure of the polymer blend monolayer, that is, the energy transfer fluorescence SNOM image directly reveals the region where both polymers were mixed. The combination of

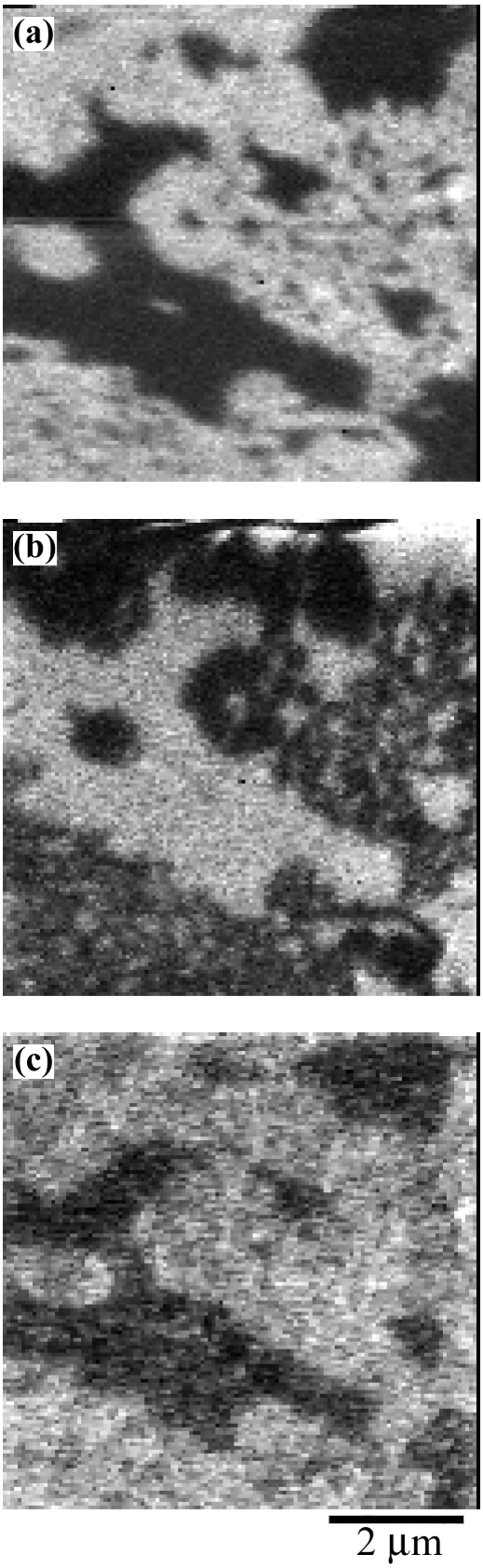

Figure 4.2. Fluorescence SNOM images for the phase-separated PODMA-Pe / PiBMA-Py monolayer before annealing; (a) Perylene fluorescence image. The excitation wavelength was 442 nm and the fluorescence from perylene was collected. (b) Pyrene fluorescence image. The excitation wavelength was 325 nm. A filter, UV-D33S (Toshiba), was placed in front of the detector to collect only the fluorescence from pyrene (360 – 400 nm). (c) Energy transfer SNOM image. The perylene fluorescence was recorded with the selective excitation of pyrene at 325 nm.

pyrene and perylene is suitable for the energy transfer fluorescence imaging since the emission bands for pyrene and perylene are clearly separated from each other. Figure 4.2c shows the energy transfer SNOM image obtained by collecting the perylene fluorescence under the selective excitation of pyrene at 325 nm. Comparison of the energy transfer image in Figure 4.2c with Figures 4.2a and 4.2b revealed that the bright area where energy transfer emission took place was in good agreement with the PODMA-Pe rich domain. This result for the monolayer deposited without annealing indicates that the PODMA domain included the area where both components were mixed at the molecular level, whereas PODMA and PiBMA appeared to form separate domains in a submicron scale as shown in Figure 4.2.

The same measurements were carried out for a PODMA-Py / PiBMA-Pe blend monolayer, for which the polymer-dye combination was opposite to that of the PODMA-Pe / PiBMA-Py sample. The SNOM images for the PODMA-Py / PiBMA-Pe monolayer are shown in Figure 4.3. Similarly to the previous PODMA-Pe / PiBMA-Py sample, the perylene fluorescence image is a negative copy of the pyrene fluorescence image, and vice versa. The perylene fluorescence SNOM image has three distinct intensity levels: low, intermediate, and high fluorescence intensities. The dark and bright areas are attributed to the PODMA-Py and PiBMA-Pe domains, respectively. AFM study for the PODMA / PiBMA blend monolayer showed that a part of the PODMA domains had a network structure including PiBMA chains in a scale of 100 nm.[27] The area with the intermediate intensity probably corresponds to such the network-like domain, from which the observed intensity appeared uniform because the structure size was smaller than the resolution of SNOM. Comparing the energy transfer emission image (Figure 4.3c) with the perylene and pyrene fluorescence images (Figures 4.3a and 4.3b), it was again found that the fluorescence due to the energy transfer was preferentially detected from the PODMA-Py domain, and not from the PiBMA-Pe rich domain.

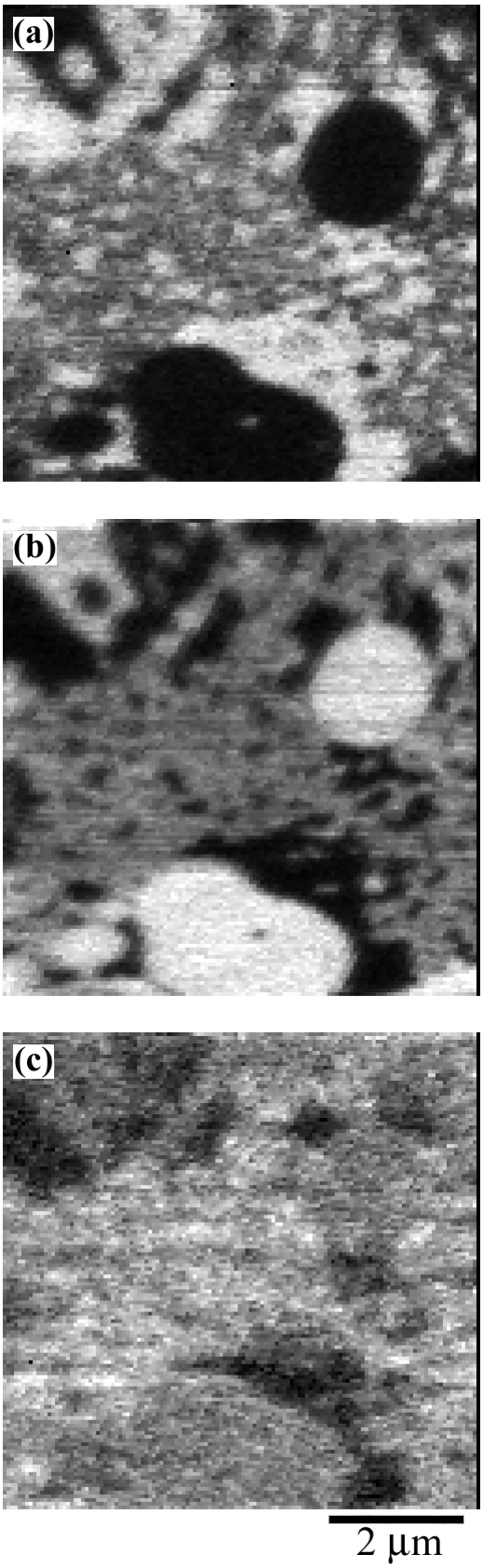

Figure 4.3. Perylene (a), pyrene (b), and energy transfer (c) fluorescence SNOM images for the PODMA-Py / PiBMA-Pe monolayer before annealing. The measurement conditions were the same as those for the PODMA-Py / PiBMA-Pe monolayer (Figure 4.2).

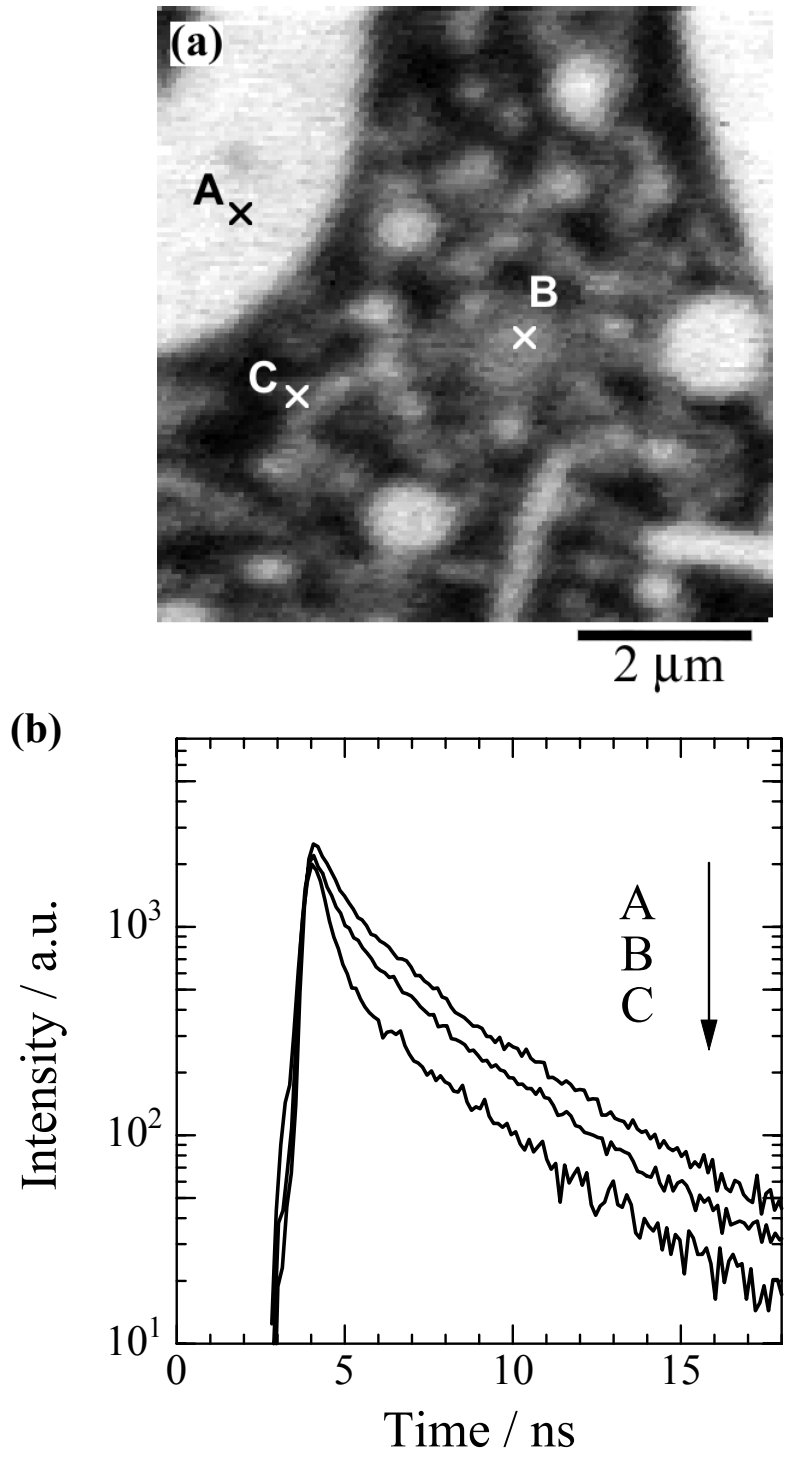

Figure 4.4. Perylene fluorescence SNOM image for the PODMA-Pe / PiBMA-Eo monolayer deposited without annealing (a) and fluorescence decay curves obtained at the different probe positions (b). The excitation wavelength was 415 nm and the fluorescence from perylene (460 – 500 nm) was collected through appropriate filters.

For both PODMA-Pe / PiBMA-Py and PODMA-Py / PiBMA-Pe monolayers, the energy transfer occurred in the PODMA rich domain irrespective of the polymer-dye combination. This result indicates that PODMA rich domain includes the other component, PiBMA. Since the octadecyl side-chains of PODMA crystallize at room temperature,[28] PODMA aggregates and forms a solid-like monolayer in spreading the polymer blend solution onto a water surface. The strong cohesive interaction between the long alkyl side-chains of PODMA resulted in the domain formation before the phase separation of PODMA and PiBMA was completed. The PiBMA components trapped in the PODMA domain caused the energy transfer emission. Since the PiBMA monolayer is liquid-like, it is unlikely that a small amount of PODMA is isolated within a PiBMA domain. Therefore, the energy transfer emission was detected preferentially from the PODMA rich domains, and not from the PiBMA domain.

The near-field time-resolved measurement was also carried out for the phase-separated monolayer. In the fluorescence decay measurements, the PODMA-Pe / PiBMA-Eo blend monolayers were used as the samples. Eosin is an energy acceptor for perylene, and the Förster radius for perylene-eosin pair was evaluated to be 4.0 nm from a separate experiment. The perylene fluorescence SNOM image is shown in Figure 4.4a. The phase separation structure was similar to those for the PODMA-Pe / PiBMA-Py and PODMA-Py / PiBMA-Pe monolayers irrespective of the polymer-dye combination. This implies that the introduction of a small amount of dye molecules (2 – 3 % of the side group) had little influence on the phase separation structure. The near-field fluorescence decay curves were obtained at the different points denoted as A, B, and C in Figure 4.4a. Each decay curve is depicted in Figure 4.4b. The brightness in Figure 4.4a indicates the ‘area’ fraction of PODMA-Pe; the brighter perylene fluorescence intensity at a given area, the larger the fraction of PODMA-Pe. Figures 4.4a and 4.4b show that the perylene fluorescence decays faster with the decrease of the

PODMA-Pe fraction, i.e., with the increase of the PiBMA-Eo fraction, because the eosin molecules deactivated the excited perylene through the energy transfer mechanism. Thus, the near-field fluorescence decay curve reflects the polymer fraction at a local area pointed by the fiber probe.

4.3.2. Phase Separation Process

Figure 4.5 shows the fluorescence SNOM images for the PODMA-Pe / PiBMA-Py monolayers with different annealing times, t_{anneal} = 0, 5, and 60 min. These images were obtained by illuminating the optical near-field at a wavelength of 442 nm and collecting the fluorescence of perylene. The bright areas correspond to the PODMA rich domains, which were labeled with perylene. Figure 4.5a indicates the image of the phase separation structure of the monolayer for t_{anneal} = 0 min, i.e., deposited without annealing. The shape of the domain for the monolayer before annealing was indented, and the domain size had a broad dispersion from ~ 100 nm to several tens of micrometers. Figures 4.5b and 4.5c show the SNOM micrographs for the monolayers annealed at 40 °C prior to deposition onto substrates. The structure of the phase-separated monolayers after annealing was round-shaped and large compared to that before annealing (Figure 4.5a). The phase structure for t_{anneal} = 60 min was larger compared to that for t_{anneal} = 5 min. Figure 4.6 depicts the far-field fluorescence spectra for the PODMA-Pe / PiBMA-Py monolayers with different annealing times; 0, 5, and 60 min. The excitation wavelength was 325 nm, at which pyrene was selectively excited. The fluorescence spectrum for the monolayer without annealing had both pyrene (360 – 430 nm) and perylene (440 – 520 nm) emission bands. As discussed in the previous section, the perylene fluorescence component in this spectrum resulted from the incomplete phase separation of PODMA and PiBMA. On the other hand, the perylene emission due to the energy transfer was not observed for the monolayers annealed at 40 °C, indicating that the annealing on the air/water interface

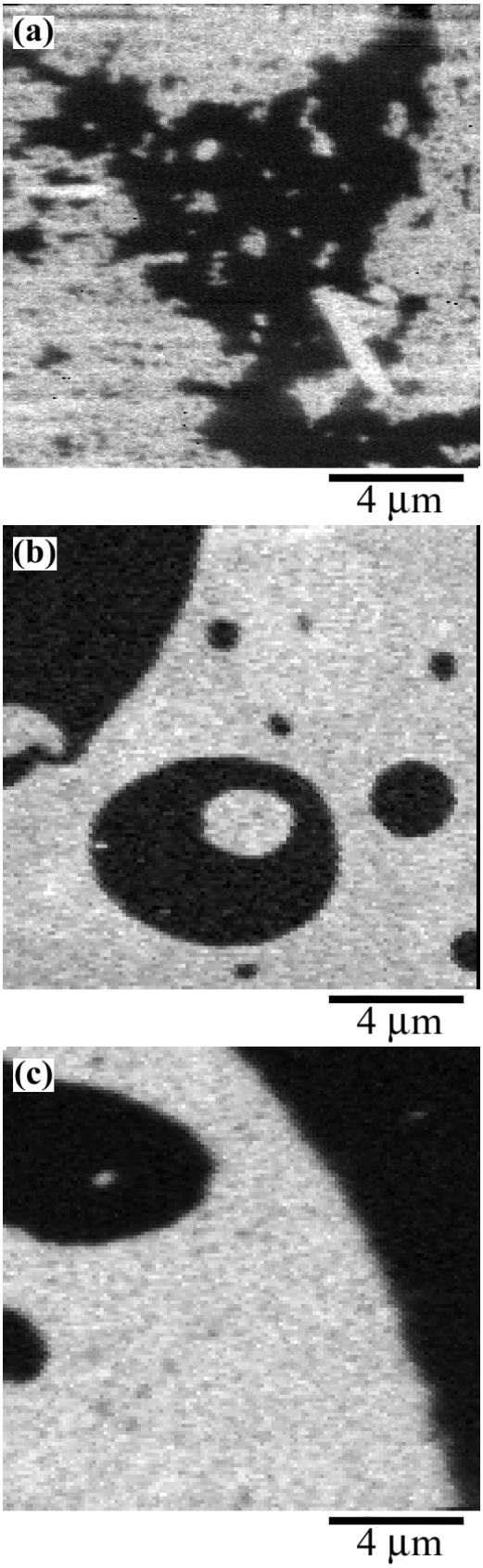

Figure 4.5. Perylene fluorescence SNOM images for the PODMA-Pe / PiBMA-Py monolayers with different annealing times; (a) 0, (b) 5, and (c) 60 min. The excitation wavelength was 442 nm and the fluorescence from perylene was collected through a filter, SC-46 (Fuji).

promoted the phase separation. Π-A isotherm measurements[28] and BAM[27] have shown that the octadecyl side-chain melts at 32 – 33 °C at the air/water interface. The PODMA behaves as a liquid-like monolayer at the annealing temperature of 40 °C. Consequently, PODMA and PiBMA become further separated from each other because of the incompatibility of these polymers, resulting in the decrease of the energy transfer emission. By comparing Figures 4.5b and 4.5c, it was found that the phase separation

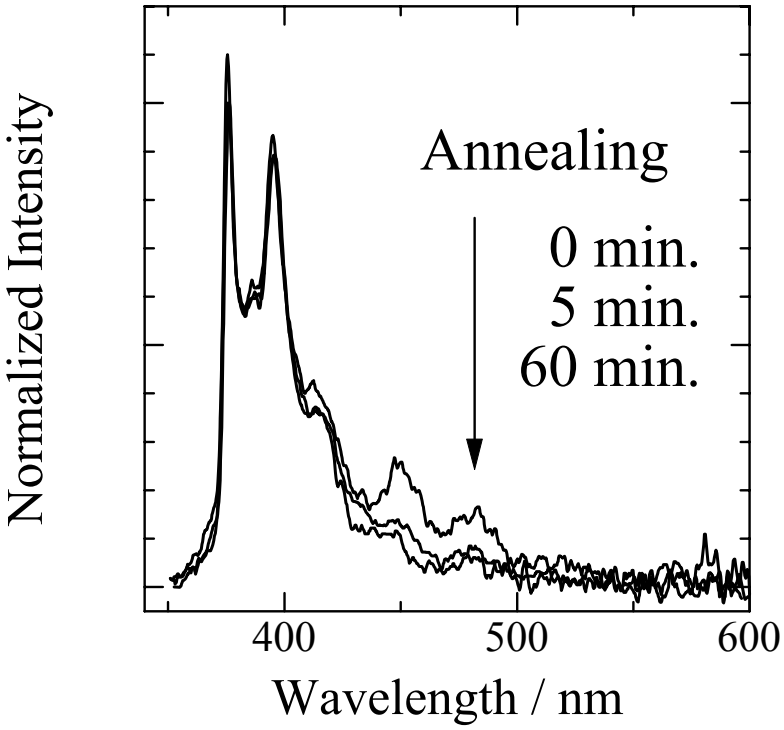

Figure 4.6. Far-field fluorescence spectra for the PODMA-Pe / PiBMA-Py monolayers with different annealing times. The wavelength of the light source was 325 nm, at which pyrene was selectively excited.

structure for t_{anneal} = 60 min was larger. Thus, the phase separation of the PODMA / PiBMA monolayer proceeded by annealing on the water surface. The polymer composition in each phase reached the equilibrium within several minutes (Figure 4.5a to 4.5b), and then the size of the structure increased with the annealing period (Figure 4.5b to 4.5c).

4.3.3. Phase Separation Structure After Annealing

The phase separation structure of the PODMA-Pe / PiBMA-Py monolayer annealed at 40 °C is discussed through the energy transfer SNOM measurements. As shown in Figure 4.7, only the phase boundary was measured as a bright area in the energy transfer SNOM image. The interfacial width estimated from Figure 4.7b was 100 – 300 nm.

The time-resolved fluorescence measurements were carried out at the phase boundary. Figure 4.8 depicts the fluorescence image for PODMA-Pe / PiBMA-Eo after annealing for 60 min. The fluorescence decays for perylene were obtained along line A indicated in Figure 4.8. The obtained fluorescence decays were fitted to a three-component exponential function, eq. 4.1, convoluted with the instrumental response function,

$$S(t) = S_0\left[a_1 \exp\left(-\frac{t}{\tau_1}\right) + a_2 \exp\left(-\frac{t}{\tau_2}\right) + a_3 \exp\left(-\frac{t}{\tau_3}\right)\right], \tag{4.1}$$

where S_0 is the intensity at $t = 0$ and $a_1 + a_2 + a_3 = 1$. The mean fluorescence lifetime, $\langle\tau\rangle$, was evaluated by the following equation.

$$\begin{aligned}\langle\tau\rangle &= S_0^{-1}\int_0^\infty S(t)\,\mathrm{d}t \\ &= a_1\tau_1 + a_2\tau_2 + a_3\tau_3\end{aligned} \tag{4.2}$$

Figure 4.9 shows the fluorescence lifetime and intensity profiles along the line A

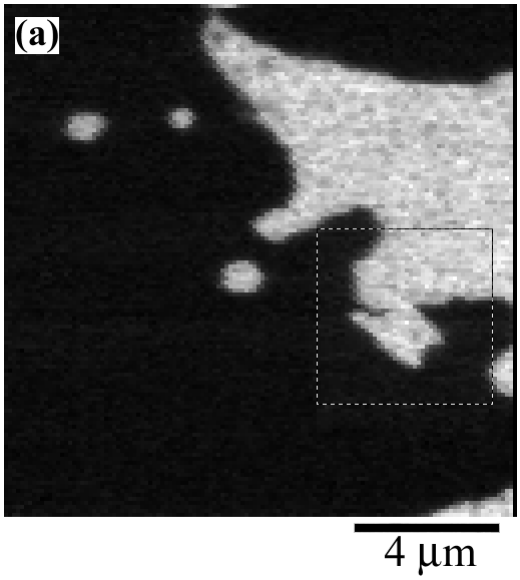

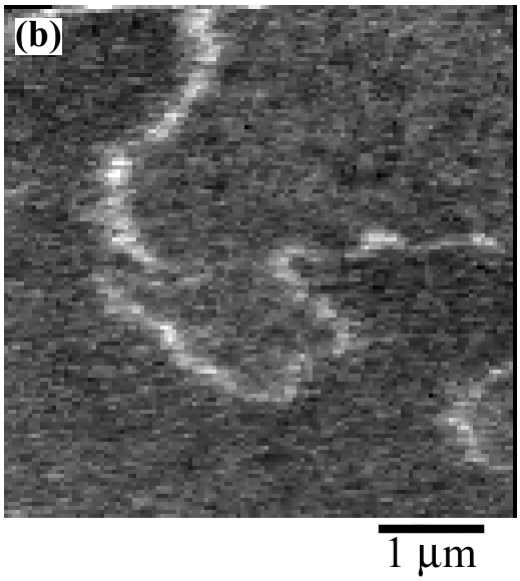

Figure 4.7. Perylene fluorescence (a) and energy transfer emission (b) SNOM images of the PODMA-Pe / PiBMA-Py monolayer after annealing. Figure 4.7b was obtained by scanning the area indicated as a dashed square in Figure 4.7a.

indicated in Figure 4.8. The mean lifetime of perylene fluorescence decreased gradually at the phase interface with scanning of the probe from the POMDA-Pe to PiBMA-Eo domains. The alteration of the lifetime was observed for the region of 200 – 400 nm in width. The effect of the SNOM probe on the time-resolved measurement is considered. Xie et al. reported that the fluorescence lifetime of a single dye molecule on a substrate was perturbed by the metal coating of the SNOM probe.[29,30] However, in our case, the fluorescence lifetime was almost constant irrespective of the distance between the probe and the sample surface. This implies little effect of the SNOM tip upon the fluorescence decay profile. Although the fluorescence decay for the PODMA-Pe monolayer measured by the near-field excitation deviated from a single exponential function, this was probably due to the other factors. Therefore, the alteration of the fluorescence lifetime across the phase interface resulted from that of the energy transfer rates at the local area under the near-field aperture. In order to discuss the effect of the interfacial width on the lifetime profile, a computer simulation was carried out.

4.3.4. Simulation of Fluorescence Lifetime Profile

The perylene fluorescence decay was calculated according to the simplified model which assumed 1) random dye distribution in a plane, 2) no perturbation of the metal coating of the probe to the energy transfer mechanism, and 3) homogeneous distribution of the optical near-field emanating from the aperture, i.e., uniform excitation probability for all dyes under the aperture. As mentioned above, the tip effect on the fluorescence lifetime was almost negligible in our experiment. Therefore, the lifetime alteration with the plane density of eosin can be simulated according to the following procedure. (i) Perylene and eosin molecules were dispersed in a two-dimensional plane assuming that PODMA-Pe and PiBMA-Eo domains came into contact at the boundary of W nm in width, i.e., the plane densities of perylene and

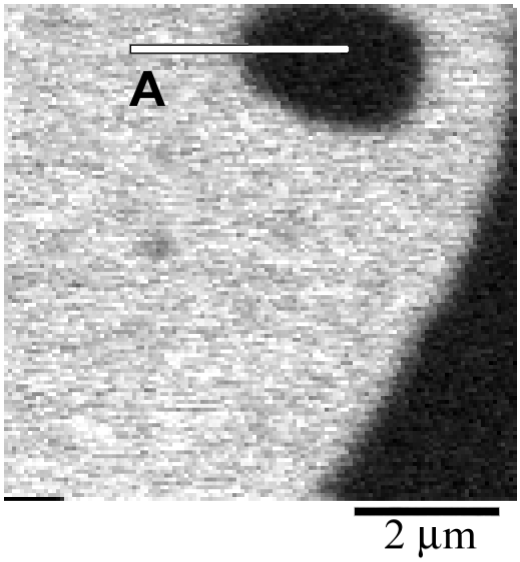

Figure 4.8. Perylene fluorescence SNOM image for the PODMA-Pe / PiBMA-Eo monolayer annealed for 60 min at the air/water interface prior to deposition. The excitation wavelength was 415 nm.

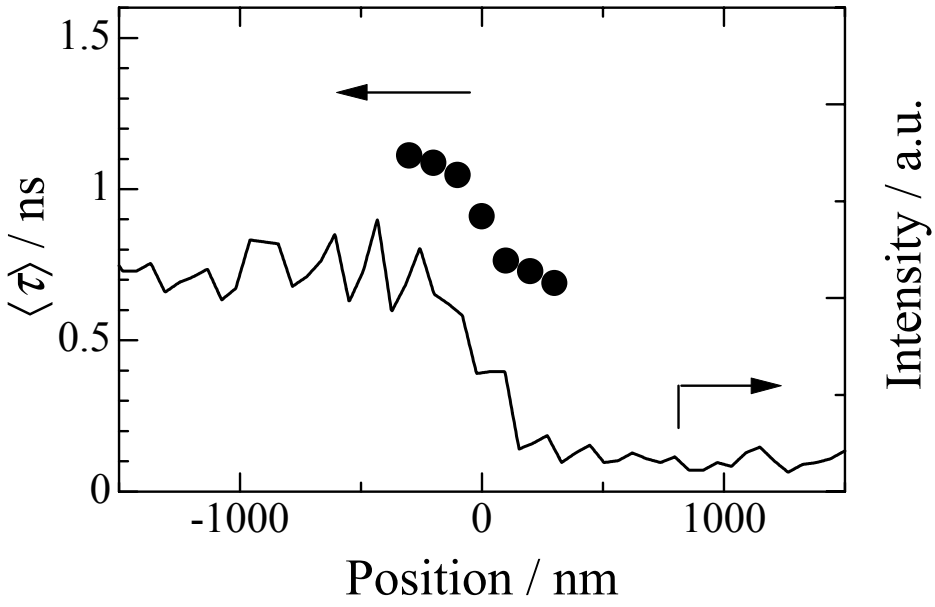

Figure 4.9. Fluorescence lifetime (closed circle) and intensity (solid line) profiles along line A indicated in Figure 4.8. The lifetime was evaluated by fitting the obtained decay curve to a three-component exponential function.

eosin at position x, $d_{Pe}(x)$ and $d_{Eo}(x)$, were given as the following equations.

$$d_{Pe}(x) = \sigma_{Pe} P(x) \tag{4.3}$$

$$d_{Eo}(x) = \sigma_{Eo} \left(1 - P(x)\right) \tag{4.4}$$

$$\begin{aligned} P(x) = \; & 1 && \text{for } x < -W/2 \\ = \; & \frac{1}{2} - \frac{x}{W} && \text{for } -W/2 \le x \le W/2 \\ = \; & 0 && \text{for } x > W/2\,, \end{aligned} \tag{4.5}$$

where σ_{Pe} and σ_{Eo} are the plane densities of the pure PODMA-Pe and PiBMA-Eo domains, respectively. $d_{Pe}(x)$ and $d_{Eo}(x)$ are schematically illustrated in Figure 4.10. (ii) The probe position x was determined, and then the perylene and eosin molecules under the aperture were counted. (iii) The fluorescence decay curve for one perylene molecule under the aperture, $S_I(t)$, was estimated according to

$$S_I(t) = \exp\left[-\frac{t}{\tau_0} \left\{ 1 + \sum_j \left(\frac{R_0}{r_{Ij}} \right)^6 \right\} \right], \tag{4.6}$$

where τ_0, R_0, and r_{Ij} are the fluorescence lifetime without quenching processes, the Förster radius, and the distance between I-th perylene and j-th eosin, respectively. For all the perylene molecules under the probe aperture, the calculations were carried out. (iv) The fluorescence decay with the SNOM probe located at position x was calculated as the sum of the decay curve for each perylene molecule under the aperture. The detailed calculation procedure for (iii) and (iv) is described elsewhere.[31,32] (v) The calculations (ii) – (iv) were carried out with respect to the different probe positions. Finally, the fluorescence lifetime at each probe position was obtained according to eq. 4.2. Thus, the fluorescence decays with a line scan across the phase boundary were obtained for a given dye distribution. In this calculation, the aperture diameter was

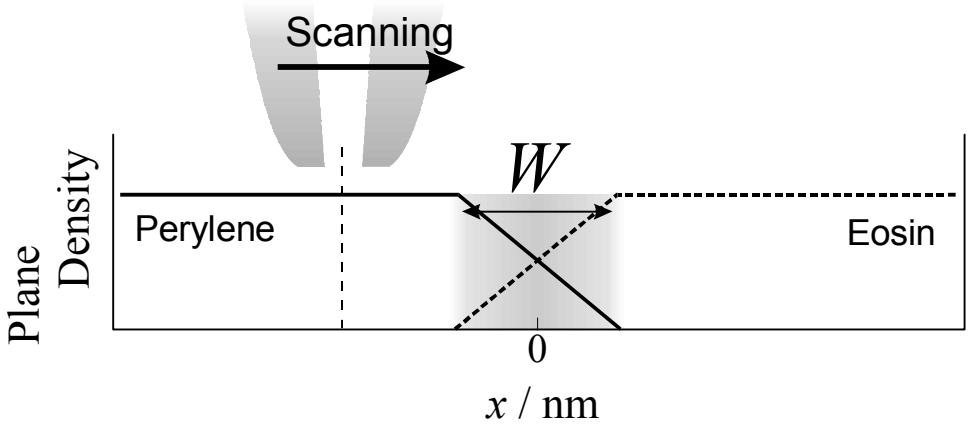

Figure 4.10. Schematic illustration for the distribution of perylene and eosin molecules. See text for details.

assumed to be 100 nm, and the other parameters, such as σ_{Pe}, σ_{Eo}, and R_0, were obtained from separate experiments.

Figure 4.11 shows the simulated decay curves averaged for 500 calculation runs, and Figure 4.12 shows the fluorescence lifetime profiles. Figure 4.11a depicts the decays calculated for a narrow interfacial width, W = 10 nm. As shown in Figure 4.12 (closed circle), the alteration of the fluorescence lifetime across the interface was almost negligible, whereas the intensity, which was defined as the integral of the fluorescence decay, varied with respect to the aperture position (the intensity profile is not shown). As mentioned above, the excitation energy transfer occurs only in the boundary region. In the case of W = 10 nm, because the interface was narrow compared to the aperture diameter, most of the excited perylene molecules under the probe were not in the boundary region and emitted fluorescence with the intrinsic lifetime, τ_0, without energy transfer. Therefore, the fluorescence decay profile was independent of the probe position. On the other hand, Figure 4.11b shows that the

fluorescence decay rate depends upon the aperture position near the wide boundary region, W = 300 nm. The simulated lifetime profile for W = 300 nm is shown as open circles in Figure 4.12, indicating that the calculated fluorescence lifetime decreases with scanning the aperture toward the PiBMA-Eo domain. In this case, the aperture size was smaller than the phase boundary. Consequently, the fluorescence lifetime was dependent on the probe position around the interface between two domains. Thus, the alteration of the mean fluorescence lifetime was observed only when the interfacial width is comparable to or larger than the aperture diameter.

It was found that an interfacial width larger than the aperture diameter was required for observing the decrease of the fluorescence lifetime at the phase boundary. The experimental result obtained from the time-resolved SNOM measurement was in good agreement with the fluorescence lifetime profile calculated for the wide interfacial width. Although the width of the phase boundary cannot be discussed quantitatively from the calculation presented here, the good agreement about the lifetime profiles obtained by the experiment and the calculation indicates clearly that PODMA and PiBMA were actually mixed in the molecular scale at the boundary on the order of a few hundred nanometers in width. The interface thickness for PODMA / PiBMA in the three-dimensional bulk state was estimated to be ca. 3 nm[23] from the theoretical equation derived by Helfand and co-workers[33,34] using the calculated interaction parameter.[35] The interfacial width for the PODMA / PiBMA blend monolayer was considerably larger than the estimated thickness for the bulk state. Such a large difference probably resulted from the low degree of freedom for the two-dimensional polymer chain.

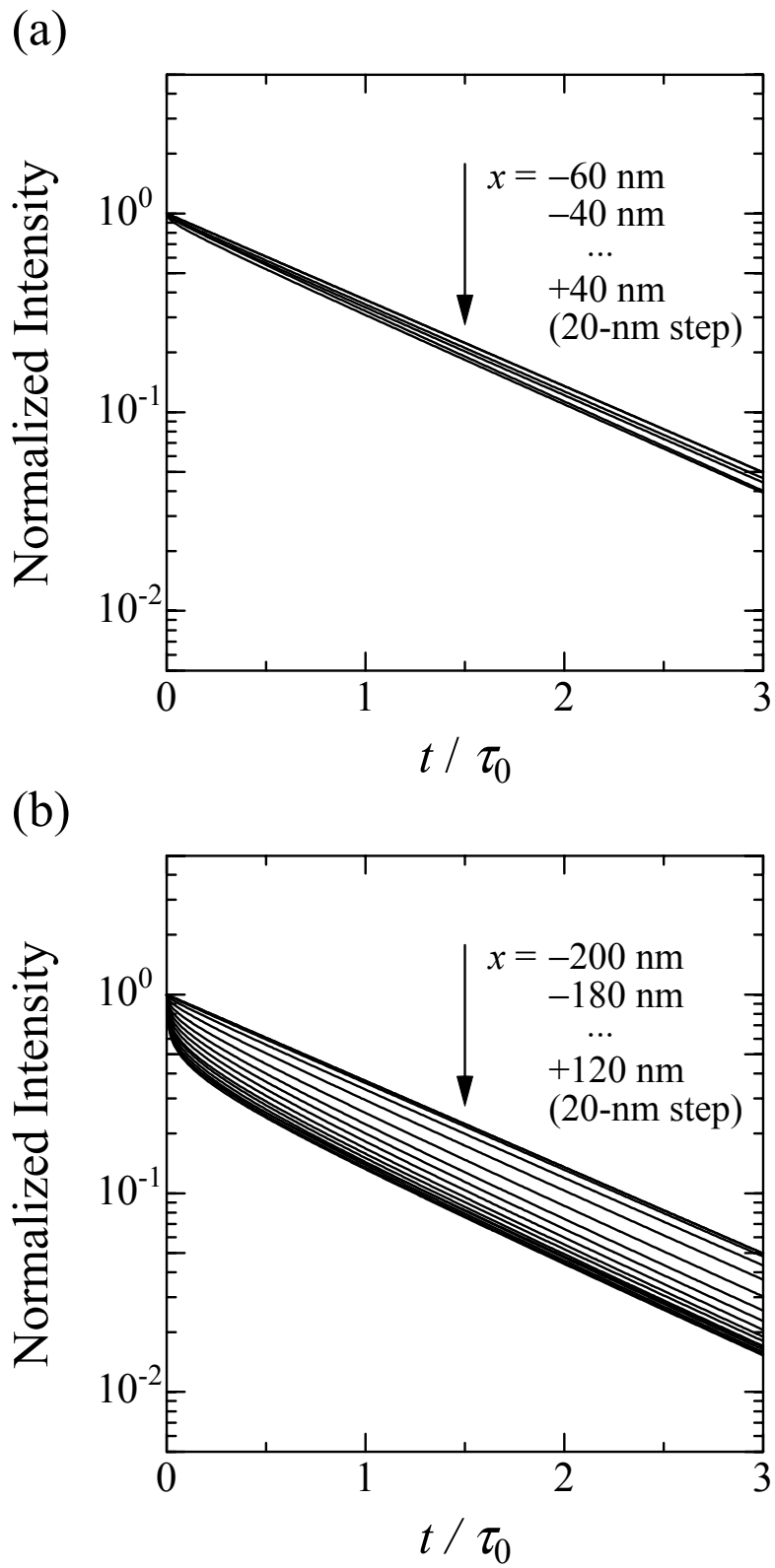

Figure 4.11. Calculated perylene fluorescence decay curves with scanning the aperture from PODMA-Pe to PiBMA-Eo domains across the phase interface. The decays were calculated for W = 10 nm (a) and W = 300 nm (b).

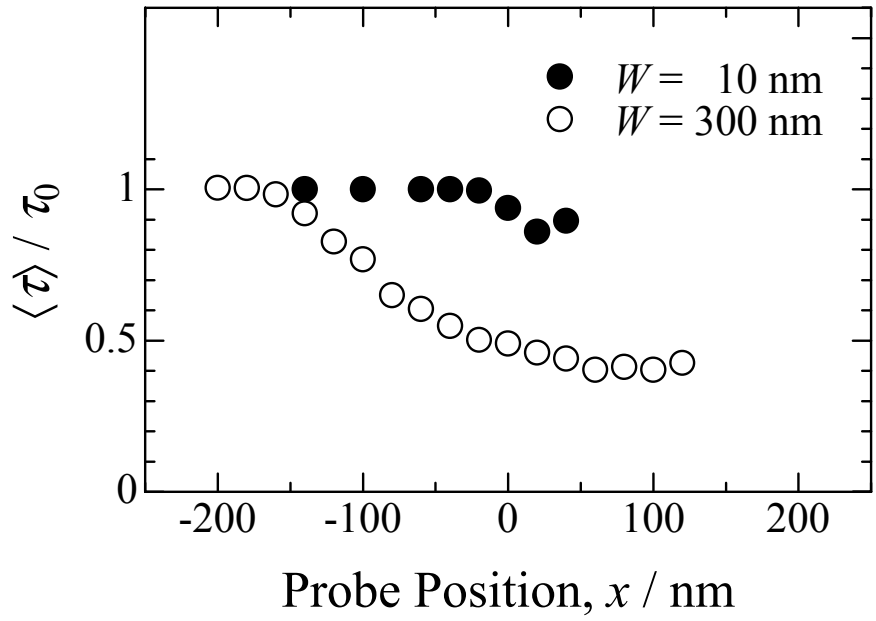

Figure 4.12. Calculated perylene fluorescence lifetime profiles across the boundary region. Closed and open circles indicate the data for W = 10 nm and W = 300 nm, respectively.

4.4. CONCLUSION

The phase separation behavior of PODMA / PiBMA blend monolayers was investigated by scanning near-field optical microscopy (SNOM). For the monolayer without annealing prior to deposition, the small amount of PiBMA component was incorporated within the PODMA rich domain. This is due to the strong crystallinity of the octadecyl side-chain which causes quick formation of a solid-like domain before the phase separation is completed. By raising the subphase temperature to 40 °C, the phase separation of both polymers was almost completed in several minutes, and then the domain size increased with annealing time. The fluorescence intensity and

lifetime profiles were obtained by time-resolved SNOM measurement for the phase-separated monolayer annealed for 60 min. The alteration of the fluorescence lifetime at the phase interface was measured. This result indicates the existence of the phase boundary on the order of a hundred nanometers, which is fairly wide compared to the interfacial thickness in the bulk state.

References

1. S. Ito, H. Okubo, S. Ohmori, and M. Yamamoto, *Thin Solid Films*, **179**, 445 (1989).
2. S. Ito, S. Ohmori, and M. Yamamoto, *Macromolecules*, **25**, 185 (1992).
3. M. Mabuchi, S. Ito, M. Yamamoto, T. Miyamoto, A. Schmidt, and W. Knoll, *Macromolecules*, **31**, 8802 (1998).
4. T. Taniguchi, Y. Fukasawa, and T. Miyashita, *J. Phys. Chem. B*, **103**, 1920 (1999).
5. H. Ohkita, H. Ishii, S. Ito, and M. Yamamoto, *Chem. Lett.*, 1092 (2000).
6. P. G. de Gennes, "Scaling Concepts in Polymer Physics," Cornell University Press, Ithaca, New York, 1979.
7. N. Sato, S. Ito, and M. Yamamoto, *Macromolecules*, **31**, 2673 (1998).
8. N. Sato, Y. Osawa, S. Ito, and M. Yamamoto, *Polym. J.*, **31**, 488 (1999).
9. T. Hashimoto, K. Tsutsumi, and Y. Funaki, *Langmuir*, **13**, 6869 (1997).
10. J. Kumaki and T. Hashimoto, *J. Am. Chem. Soc.*, **120**, 423 (1998).
11. N. Sato, S. Ito, and M. Yamamoto, *Polym. J.*, **28**, 784 (1996).
12. T. Yuba, S. Yokoyama, M. Kakimoto, and Y. Imai, *Adv. Mater.*, **6**, 888 (1994).
13. E. Betzig and J. K. Trautman, *Science*, **257**, 189 (1992).
14. M. A. Paesler and P. J. Moyer, "Near-Field Optics: Theory, Instrumentation, and Applications," John Wiley & Sons, New York, 1996.
15. M. Ohtsu, "Near-Field Nano/Atom Optics and Technology," Springer, Tokyo, 1998.
16. B. Hecht, B. Sick, U. P. Wild, V. Deckert, R. Zenobi, O. J. F. Martin, and D. W. Pohl, *J. Chem. Phys.*, **112**, 7761 (2000).
17. J. Hwang, L. K. Tamm, C. Bohm, T. S. Ramalingam, E. Betzig, and M. Edidin, *Science*, **270**, 610 (1995).

18. C. W. Hollars and R. C. Dunn, *J. Phys. Chem. B*, **101**, 6313 (1997).
19. J. Kerimo, D. M. Adams, P. F. Barbara, D. M. Kaschak, and T. E. Mallouk, *J. Phys. Chem. B*, **102**, 9451 (1998).
20. E. Mei and D. A. Higgins, *Appl. Phys. Lett.*, **75**, 430 (1999).
21. D. A. Vanden Bout, J. Kerimo, D. A. Higgins, and P. F. Barbara, *Acc. Chem. Res.*, **30**, 204 (1997).
22. J. Hofkens, L. Latterini, P. Vanoppen, H. Faes, K. Jeuris, S. De Feyter, J. Kerimo, P. F. Barbara, and F. C. De Schryver, *J. Phys. Chem. B*, **101**, 10588 (1997).
23. H. Aoki, Y. Sakurai, S. Ito, and T. Nakagawa, *J. Phys. Chem. B*, **103**, 10553 (1999).
24. S. Mononobe, T. Saiki, T. Suzuki, S. Koshihara, and M. Ohtsu, *Opt. Commun.*, **146**, 45 (1998).
25. D. V. O'Cornner and D. Phillips, "Time-Correlated Single Photon Counting," Academic Press, London, 1984.
26. I. B. Berlman, "Energy Transfer Parameters of Aromatic Compounds," Academic Press, New York, 1973.
27. Y. Sakurai, N. Sato, S. Ito, and M. Yamamoto, *Kobunshi Ronbunshu*, **56**, 850 (1999).
28. T. Nakahara, K. Motomura, and R. Matuura, *J. Polym. Sci. A-2*, **4**, 649 (1966).
29. X. S. Xie and R. C. Dunn, *Science*, **265**, 361 (1994).
30. R. X. Bian, R. C. Dunn, and X. S. Xie, *Phys. Rev. Lett.*, **75**, 4772 (1995).
31. S. Ohmori, S. Ito, and M. Yamamoto, *Macromolecules*, **24**, 2377 (1991).
32. M. Mabuchi, K. Kawano, S. Ito, M. Yamamoto, M. Takahashi, and T. Masuda, *Macromolecules*, **31**, 6083 (1998).
33. E. Helfand and Y. Tagami, *J. Chem. Phys.*, **56**, 3592 (1972).
34. D. Broseta, G. H. Fredrickson, E. Helfand, and L. Leibler, *Macromolecules*, **23**, 132 (1990).

35. S. Krause, *J. Macromol. Sci. Rev. Macromol. Chem.*, **C7**, 251 (1972).

Chapter 5

NANOMETRIC INHOMOGENEITY OF POLYMER NETWORK STUDIED BY SCANNING NEAR-FIELD OPTICAL MICROSCOPY

5.1. INTRODUCTION

Gels, which consist of three-dimensional networks of polymer chains, have attracted much attention for a long time from the viewpoints of both fundamental physical chemistry and applications to various fields. Since the structural heterogeneity is a critical factor for determining the functions of gels, the internal structure of polymer networks has been extensively investigated by many workers.[1-13] In a gelation process, the fluctuations of polymer density are frozen permanently by the introduction of crosslinking, resulting in the static structural inhomogeneity.[5] The heterogeneity of the network structure has been found to increase with the increase of crosslink density.[4,6] Recently, Shibayama et al. demonstrated the inverse dependence on the crosslink density in weakly charged hydrogels in particular experimental conditions, such as the temperature and the degree of ionization.[7-9] They explained the inverse phenomenon on the basis of Rabin-Panyukov theory.[10]

Although the inhomogeneity of the polymer networks has been mainly studied by various scattering techniques, few direct observations in real space have been reported. Suzuki et al. investigated the surface structure of poly(acrylamide) (PAAm) and poly(*N*-isopropylacrylamide) (PNIPAm) gels by atomic force microscopy.[11,12] They showed that the submicron structure of the gel surface was strongly dependent on

the crosslink density and the osmotic pressure. Hirokawa et al. examined the three-dimensional internal structure of the PNIPAm gels in a scale of several microns using a confocal microscope.[13] They discussed the preparation temperature dependence of the internal structure and showed that the gels had a bicontinuous structure of dense and sparse regions in the PNIPAm gel.

Fluorescence techniques have been widely used for investigation of structure and dynamics of various polymer systems,[14-19] and it seems to be also useful to study the internal structure of polymer networks. However, the fluorescence techniques have not been applicable to the local area smaller than several hundred nanometers because of the diffraction limit of light for the conventional optical microscopy. Scanning near-field optical microscopy (SNOM) allows one to take optical micrographs and spectroscopic information in a nanometric local area where the specimen is illuminated by the optical near-field emanating from an aperture much smaller than the wavelength of light.[20-27] Because the probe-sample gap is kept constant during the raster-scanning of the sample in SNOM measurement, the height profile of the sample surface can be obtained simultaneously with the optical image and the spectroscopic properties in the local area. In this chapter, the static structural inhomogeneity of the poly(methyl methacrylate) (PMMA) network was investigated by means of SNOM. The spatial distribution of the network chain segments labeled with fluorescent groups was directly observed with a resolution of < 100 nm. The time-resolved measurements were also carried out by SNOM. The energy transfer among the dyes introduced into the network chain was also discussed in terms of the segment density on the molecular scale.

5.2. EXPERIMENTS

5.2.1. Materials

Figure 5.1 shows the chemical structures of the PMMA networks labeled at the side-chains and the crosslinking points. 3-Perylenylmethyl methacrylate was synthesized by the following procedure. 3-Perylenemethanol was synthesized by the reduction of 3-formylperylene, which was prepared by Vilsmeiyer reaction of perylene. The esterification of 3-perylenemethanol with methacryloyl chloride (Tokyo Chemical Industry) yielded 3-perylenylmethyl methacrylate, which was purified by column chromatography on silica gel. Eosin-labeled methacrylate monomer was synthesized by the esterification of methacryloyl chloride with methyl eosin (Aldrich) and purified through a silica gel column. 9,10-Anthrylenemethyl dimethacrylate was synthesized as a fluorescent crosslinking agent.[16,28]

The PMMA network labeled with perylene at the side-chains was prepared by the free radical copolymerization of methyl methacrylate (MMA; Wako Pure Chemical Industries), 3-perylenylmethyl methacrylate (dye-labeled monomer), and ethylene glycol dimethacrylate (crosslinker; Wako Pure Chemical Industries). The crosslink density, which was defined as the molar ratio of crosslinker to the MMA monomer, was varied from 0.1 to 0.5 %. *N*, *N*'-dimethyl formamide (DMF), benzene, and acetonitrile were used as solvents. MMA and the solvents were purified by distillation, and ethylene glycol dimethacrylate was used as received. Polymerization was carried out at 60 °C for 15 h in a solution of the monomer mixture (50 vol%) using α, α'-azobisisobutyronitrile (Nacalai Tesque) as an initiator. The gels labeled with both perylene and eosin were also prepared similarly. The crosslink labeled network was prepared from MMA and 9,10-anthrylenemethyl dimethacrylate (dye-labeled crosslinker) in a benzene solution with a crosslink density of 0.1 %. Polymerization was carried out in the same manner as the case of the side-chain labeled gel. The

residual monomer and sol fraction were extracted in distilled toluene until the absorption of the dye was not detected from the decanted solvent. The amount of the extracted dye was determined by UV-vis absorption measurement. The dye-labeled linear PMMA was also prepared according to the same procedure except for the absence of the crosslinker. In SNOM measurement, the samples must be sufficiently thin with respect to the dimension of the expected structure. However, since the gels swollen in a solvent were so fragile that they could not be cut to a thickness of a few hundred nanometers, the sample gels were solidified according to the following procedure. The gels were cut into a thick disk, dried in vacuum, swollen in MMA,

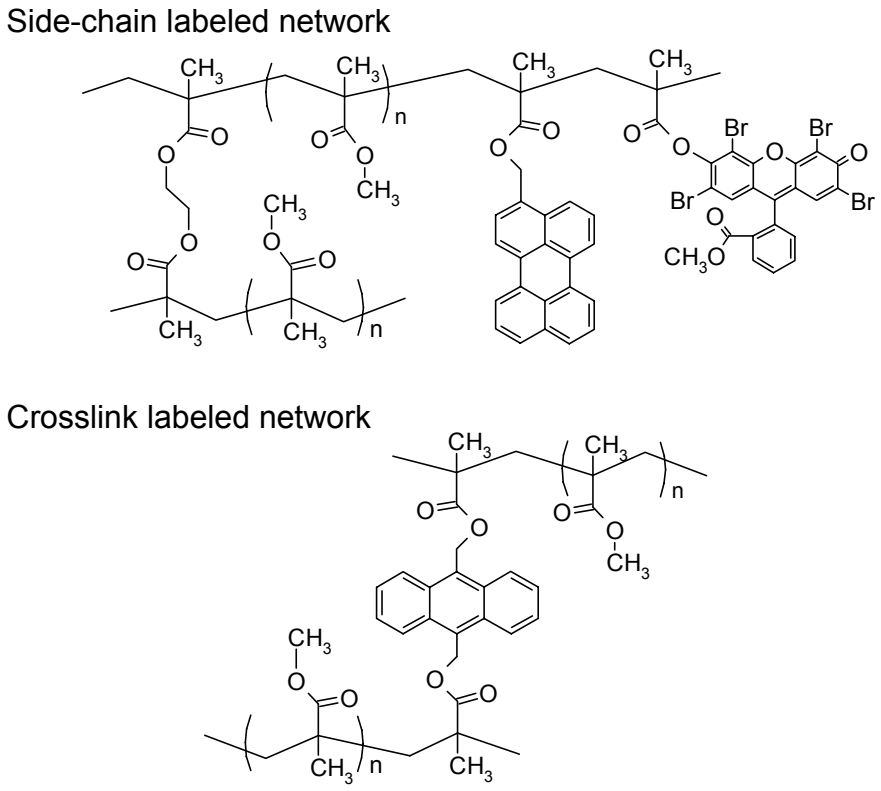

Figure 5.1. Chemical structures of side-chain and crosslink labeled PMMA network samples.

and then heated in order to polymerize the MMA monomer. The resulting network in the PMMA bulk was optically transparent and appeared homogeneous. The gel was sliced to ca. 100 nm thick using an ultramicrotome, and each sample piece was transferred onto a glass cover slip for SNOM measurements.

5.2.2. SNOM Measurements

The SNOM system used in this study was based on a commercially available instrument (SP-301, Unisoku). A CW He-Cd laser (λ = 442 nm; IK5351R-D, Kimmon Electric) and the second harmonic of a picosec Ti:sapphire laser (Tsunami, Spectra Physics) were used as the light sources. The wavelength of the Ti:Sa laser was 397 and 415 nm for the samples labeled with anthracence and perylene, respectively, and the repetition rate of the excitation pulse was 4 MHz. The SNOM probes used were made from an optical fiber with a pure silica core,[22,29,30] and the diameter of the aperture at the end of a probe was typically 50 – 100 nm. The obtained SNOM images consisted of 256 × 256 pixels, and the gate time for photon counting was 16 ms for each pixel. The near-field time-resolved measurement was carried out by the time-correlated single photon counting technique.[31] The details for the near-field time-resolved measurement were described in Chapter 4.

5.3. RESULTS AND DISCUSSION

5.3.1. SNOM Image of Polymer Network

Figures 5.2 shows the topographic, transmission, and fluorescence SNOM images for the same area of the PMMA network side-chain labeled with perylene in which the crosslink density was 0.1 %, respectively. In the topographic image (Figure 5.2a), there were several ridges in an oblique direction. They were “knife marks” on

the surface, which were the traces of the glass knife of the microtome due to the roughness of the knife blade. The transmission SNOM image was obtained by recording the intensity of light transmitted through the sample. The contrast in the transmission SNOM image results from the surface topography and the optical properties, such as refractive index and transmittance, beneath the sample surface.[25,32] No structural features besides the knife marks were seen in Figure 5.2b, indicating that the contrast in this image was mainly affected by the surface topography for the specimen and the internal structure could not be measured. On the other hand, the fluorescence SNOM image, Figure 5.2c, had no correlation with the topographic image. It can be safely said that the structure seen in Figure 5.2c is free from the artifact due to the topographic effect at the surface, and shows the spatial distribution of the fluorescent dye molecules in the PMMA gel. Thus, the fluorescence SNOM allowed the direct observation of the distribution of the chain segments with a lateral resolution of 100 nm. The PMMA network had structural inhomogeneity in a scale of several hundred nanometers. The topographic images for all the samples were also measured for the larger scanning area to estimate the sample thickness, which was defined as the height difference between the upper surface of the sample and the glass substrate (the images are not shown here). The thickness of each sample was typically 100 nm, which was sufficiently small compared to the dimension of the network structure. As the control experiment, the SNOM measurement was carried out also for the uncrosslinked PMMA sample, which was prepared by the solidification of the dye-labeled linear PMMA dissolved in MMA. Figure 5.3 shows the fluorescence SNOM image for the uncrosslinked sample. Any contrast could not be seen in Figure 5.3. This indicates that the inhomogeneous structure observed in the fluorescence SNOM image (Figure 5.2c) was not formed by the solidification procedure following the gel preparation but induced by the introduction of crosslinking. Thus, the internal structure of the gel could be successfully measured in a length scale of 100 nm.

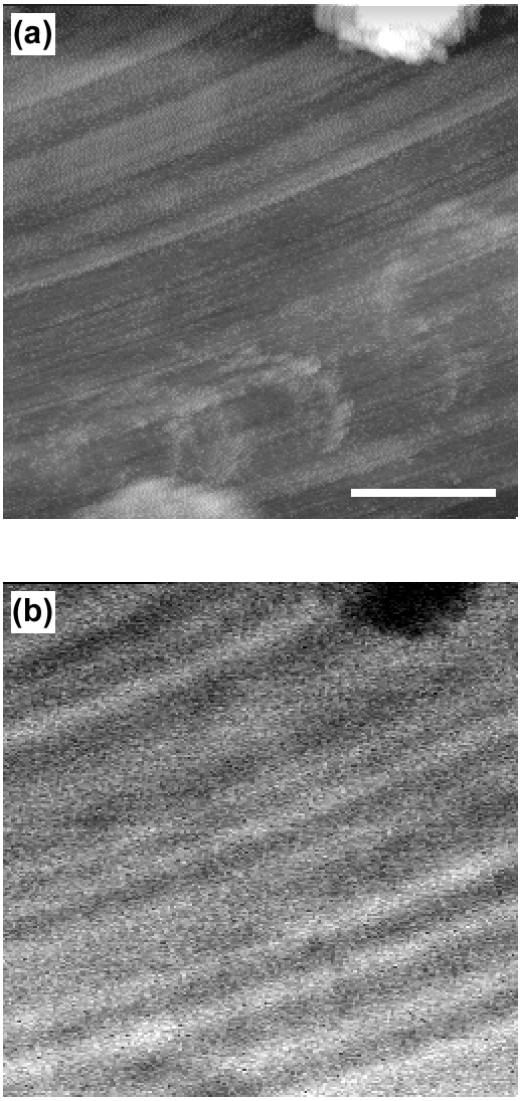

Figure 5.2. Topographic (a), transmission (b), and fluorescence SNOM images (c) for the side-chain labeled PMMA network with a crosslink density of 0.1 %. All the images were obtained for the same area. The wavelength of the light source was 442 nm. The scale bars indicate 1 μm.

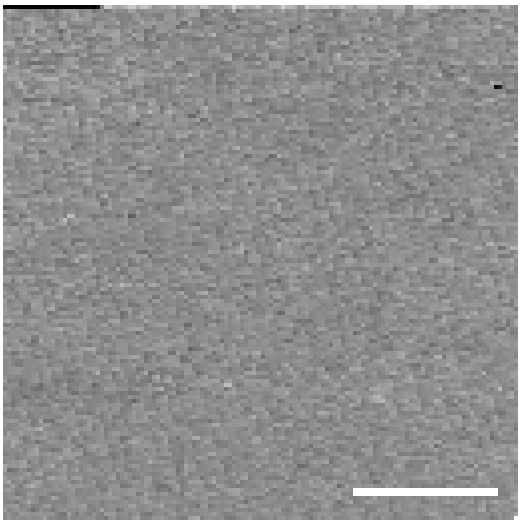

Figure 5.3. Fluorescence SNOM image for the uncrosslinked PMMA. The sample was prepared by the solidification of the dye-labeled linear PMMA dissolved in MMA. The fraction of the labeled polymer was the same as that of the network with a crosslink density of 0.1 %. The scale bar indicates 1 μm.

5.3.2. Spatial Distribution of Crosslinking Point

Figure 5.4 depicts the fluorescence SNOM images for the side-chain and crosslink labeled networks, both of which were prepared under the same condition except for the dye-labeled position. The dimensions of the structure for both samples were estimated to be 500 – 600 nm, implying that the spatial distribution of the crosslinking points was similar to that of the network chain segments.

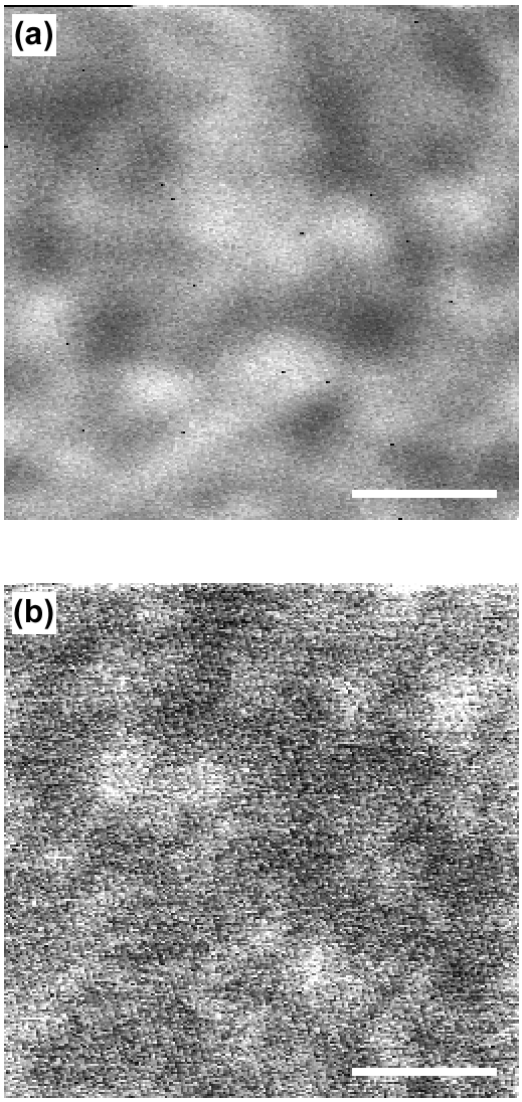

Figure 5.4. Fluorescence SNOM images for the side-chain (a) and crosslink (b) labeled PMMA networks. The crosslink density was 0.1 % for each network. The He-Cd laser (442 nm) and the second harmonic of the Ti:sapphire laser (397 nm) were used as the excitation sources for the side-chain and crosslink labeled samples, respectively. The scale bar in each image indicates 1 μm.

5.3.3. Preparation Condition Dependence

The preparation condition, such as temperature and solvent, plays an important role in the formation of polymer network structure. Shibayama et al. reported that the structural inhomogeneity of PAAm and PNIPAm gels was dependent upon the solvent quality in the network formation.[6,8] Figure 5.5 shows an example of the SNOM images for the PMMA network prepared in acetonitrile, which is a Θ solvent for PMMA. The size of the bright domain was evaluated to be 1 μm, which was much larger than that for the network prepared in benzene. The details are still unclear, but the lower solvent quality may have caused the larger structure, possibly resulting from the aggregation of the chain segments enhanced by phase separation during the network formation.

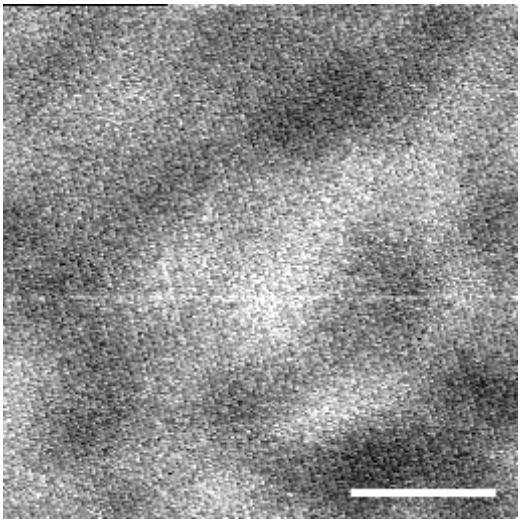

Figure 5.5. Fluorescence SNOM image for the PMMA network sample prepared in acetonitrile. The crosslink density was 0.1 %. The scale bar indicates 1 μm.

5.3.4. Crosslink Density Dependence

Figure 5.6 shows the fluorescence images for the side-chain labeled network samples with different crosslink densities. It should be noted that it is impossible to compare the absolute values of the fluorescence intensity among the different samples because the excitation intensity and the detection efficiency are not exactly the same for each sample in the near-field experiment. The bright domains were estimated to be ca. 600 and 250 nm for 0.1 % and 0.2 % samples, respectively. No contrast could be seen in the fluorescence images for 0.3 % and higher crosslink densities because the inhomogeneous structure for them was smaller than the resolution of the SNOM, ≤ 100 nm. The characteristic size of the structure decreased markedly with an increase of the crosslink density. In the gelation process, the crosslinks are thought to be introduced heterogeneously because of the concentration fluctuation in the polymerization solution, and then the chain length between crosslinking points had a wide dispersion. Considering the crosslink density of 0.1 – 0.2 %, the size of the structure induced by such a mechanism is expected to be in a scale of ~ 10 nm, whereas the domain size measured by SNOM was in a submicron scale. Therefore, the structure imaged by SNOM is not the mesh of the 'polymer chain,' and the following mechanism is considered. At the early stage of polymerization, microclusters of polymer chains are formed by introduction of crosslinking. As the polymerization proceeds, the microclusters are crosslinked to each other and form a three-dimensional network. The inhomogeneity of the polymer network in a scale of several hundred nanometers was composed of such a crosslinked microcluster, which is discussed later. For the network with a low crosslink density, inter-cluster crosslinking occurred after the individual cluster fully increased in size, consequently resulting in a larger domain size. In addition, the polymer chains, which were not incorporated into the infinite polymer network, were also produced in the gel as the sol fraction. They were extracted in the process of the sample preparation, yielding void of polymer segments in the resulting

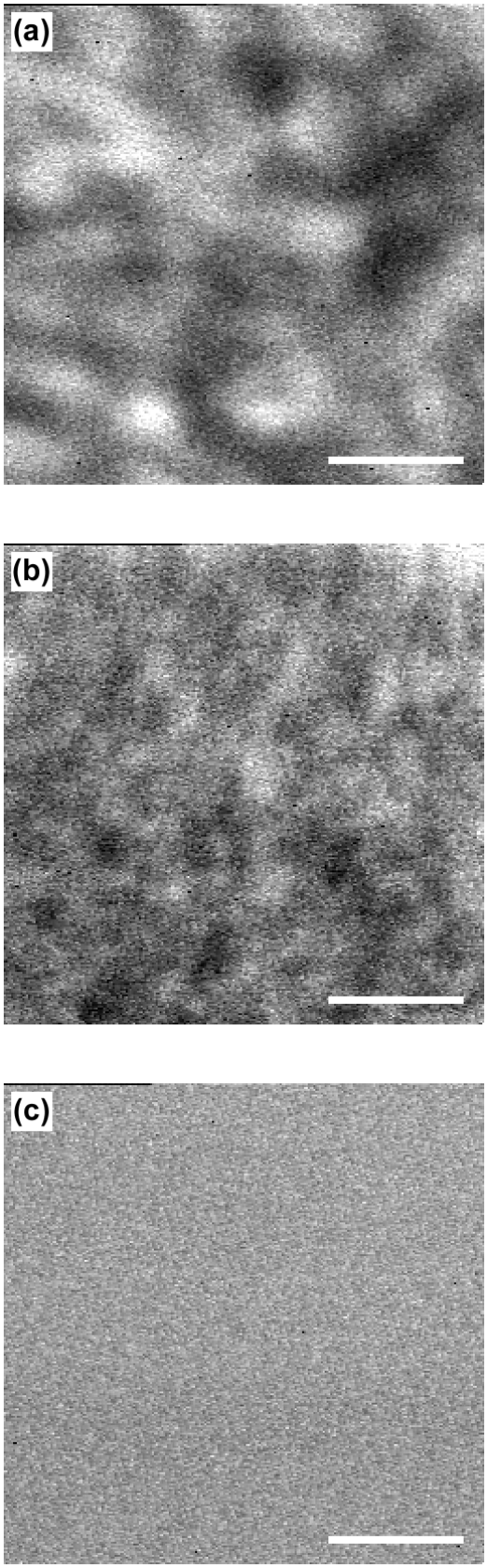

Figure 5.6. Fluorescence SNOM images for the network samples with different crosslink densities; 0.1% (a), 0.2% (b), and 0.3% (c). The scale bar in each image indicates 1 μm.

network. Thus, the low crosslink density resulted in a large network structure. On the other hand, the larger crosslink density resulted in a faster and smaller cluster formation, consequently yielding the smaller characteristic size of the network, which appeared more homogeneous under the SNOM images.

5.3.5. Time-Resolved Measurements in a Nanometric Scale

The inhomogeneous structure of the PMMA networks in a 100-nm scale could be directly measured by the fluorescence SNOM. Although the knowledge of the structure on the molecular scale is indispensable for understanding the morphology of polymer networks, the lateral resolution of a SNOM micrograph was far from the atomic resolution. Therefore, we investigated the structural inhomogeneity in a nanometer scale by the energy transfer method, which was applied to a local area using SNOM. In the sample labeled with both perylene and eosin, the non-radiative excitation energy transfer from perylene (energy donor) to eosin (energy acceptor) occurs when they are close to each other. The rate of the energy transfer by the Förster mechanism is proportional to $(R/R_0)^{-6}$, where R is the distance between a perylene and an eosin molecule and R_0 is the Förster radius. R_0 was determined to be 4.0 nm through a separate experiment; the theoretical decay curves[33] were fitted to the experimentally obtained decays for the PMMA cast films where perylene and eosin were homogeneously dispersed at given concentrations. Therefore, the fluorescence decay of a perylene molecule probes the distance of separation between a perylene and the surrounding eosin molecules in a range of 2 to 10 nm. The denser the polymer segments are, the faster the fluorescence decays because of the shorter distance to the acceptor. The energy transfer dynamics from perylene to eosin was examined in order to estimate the segment density in the local area by the near-field time-correlated single photon counting technique. Figure 5.7a shows the perylene fluorescence image for the PMMA network with a crosslink density of 0.1 %. The excitation source was a

frequency-doubled Ti:sapphire laser operated at 415 nm. Figure 5.7b depicts the fluorescence decay curves for perylene emission obtained at the points denoted as A, B, C, and D in Figure 5.7a. The decay profile was fairly similar at all points. Since the energy transfer dynamics is determined by the dye distribution in the distances of 2 – 10 nm, this implies that the spatial distribution of the network chain at the different points is quite similar within the scale of 10 nm, whereas the network structure is obviously inhomogeneous in the 100-nm scale.

Before discussing the fluorescence decay in more detail, we estimated the concentration of eosin averaged over the whole sample volume, $[\mathrm{Eo}]_{\mathrm{ensemble}}$, assuming that the dye molecules were homogeneously dispersed in the network. $[\mathrm{Eo}]_{\mathrm{ensemble}}$ could be calculated as

$$[\mathrm{Eo}]_{\mathrm{ensemble}} = \frac{N_0 - N_{\mathrm{ext}}}{V_0} \Bigg/ \left(\frac{d}{d_0}\right)^3 , \tag{5.1}$$

where N_0, V_0, and d/d_0 are the amount of eosin in feed, the initial volume (just after the polymerization), and the swelling ratio defined as the ratio of the diameters of the network sample in the initial and final states, respectively. The amount of extracted eosin, N_{ext}, was evaluated by UV-vis absorption measurement. The ensemble average concentration, $[\mathrm{Eo}]_{\mathrm{ensemble}}$, for the PMMA network shown in Figure 5.7 was estimated to be 0.71 mM. The perylene fluorescence decays indicated in Figure 5.7b were compared to that for the homogeneous system, which was a mixture of perylene and eosin monomer compounds dispersed in a PMMA spin cast film.[34] The near-field fluorescence decay profiles measured at different points for the spin cast film were in exact agreement with each other, and the far-field fluorescence decays separately obtained could be well fitted to the theoretical curve for the randomly distributed perylene and eosin molecules in a three-dimensional space:

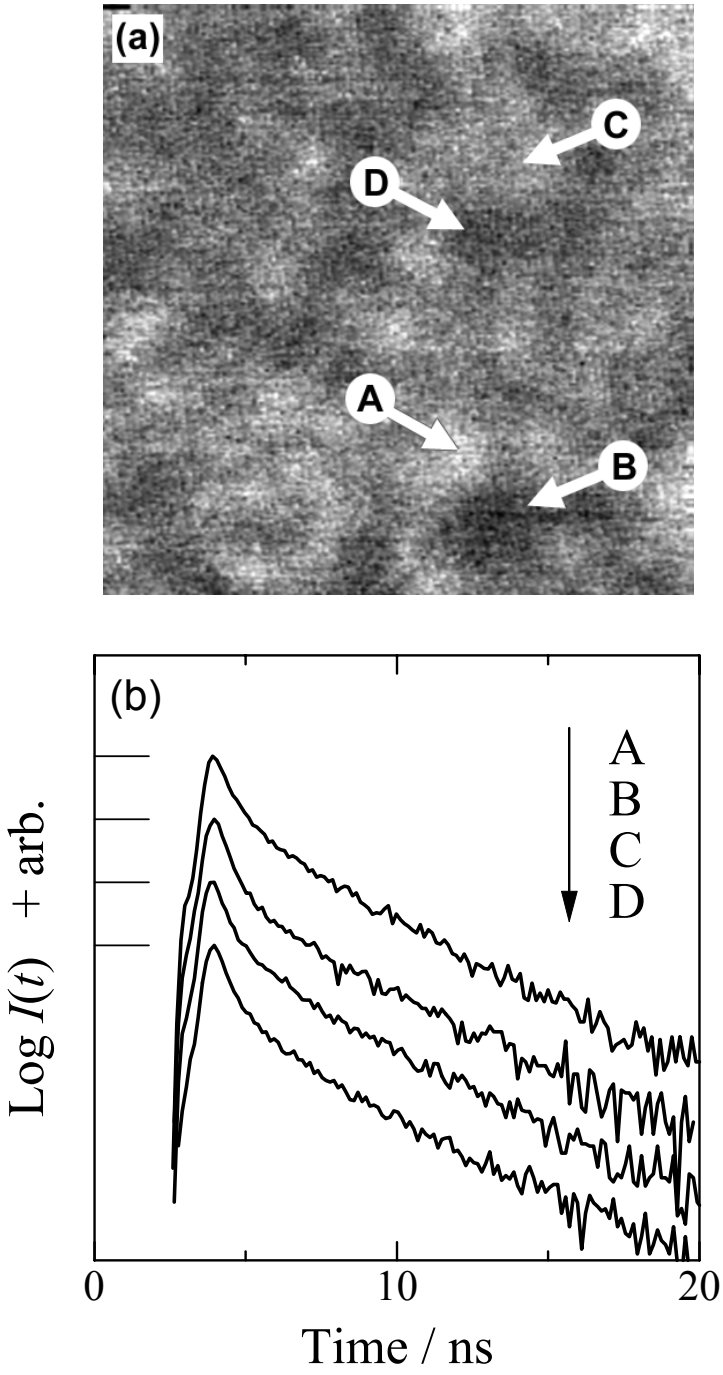

Figure 5.7. Fluorescence SNOM image (a) and perylene fluorescence decay curves (b) for the PMMA network labeled at side-chains with perylene and eosin. The sample was prepared in DMF, and the crosslink density was 0.1 %. (a) was obtained by collecting the perylene fluorescence. The scanning area in (a) was 3.75×3.75 μm^2. The fluorescence decay in (b) was measured at various points denoted as A, B, C, and D in (a). The excitation wavelength was 415 nm.

$$I(t) = I_0 \exp\left(-\frac{t}{\tau_0} - \frac{4}{3}\pi^{\frac{3}{2}} R_0^{\,3} [\mathrm{A}] \left(\frac{t}{\tau_0} \right)^{\frac{1}{2}} \right), \tag{5.2}$$

where I_0, [A], and τ_0 are the fluorescence intensity at t = 0, the concentration of the acceptor (eosin), and the intrinsic fluorescence lifetime of the donor (perylene) without the energy transfer process, respectively.[33] Thus, the dye-doped spin cast film can be used as a homogeneous model system.

Figure 5.8 shows the fluorescence decays for the uncrosslinked polymer sample and the spin cast film, in which the eosin concentrations were 0.70 mM. The decay curve for the network, which is shown as curve A in Figure 5.7b, is also shown in this figure. Although the averaged dye concentrations were the same for them (0.7 mM), the fluorescence decay profile for the network was quite different from those for the monomer model and linear polymer systems, that is, the decay rate for the network was much larger than those for the homogeneous systems. The initial decay rate corresponded to that for a spin cast film with [Eo] = 15 mM. It is difficult to simply compare the near-field fluorescence decays because the metal coating of the SNOM probe may affect the fluorescence lifetime.[35-37] However, in our case, both fluorescence decay profiles obtained in the near-field and the far-field were similar for the spin cast films, implying that the SNOM tip had little influence on the near-field time-resolved measurements. Therefore, it is safely said that the eosin concentration was more than 10 mM, i.e., the chain segment density was more than ten times concentrated compared to the ensemble average concentration. Thus, it was found that the local segment density was much larger than the ensemble average density and the estimated density was almost independent of the probe position through the time-resolved measurement for the local area, whereas the structure appeared heterogeneous in the fluorescence SNOM image. These results indicate that the PMMA network has a structural hierarchy as schematically illustrated in Figure 5.9. On the molecular scale, the network chain forms a microcluster, in which the chain segment is locally

concentrated due to the introduction of crosslinking. Such crosslinked clusters are connected to each other and form the inhomogeneous structure in a length scale of several hundred nanometers, which was observed in the fluorescence SNOM image.

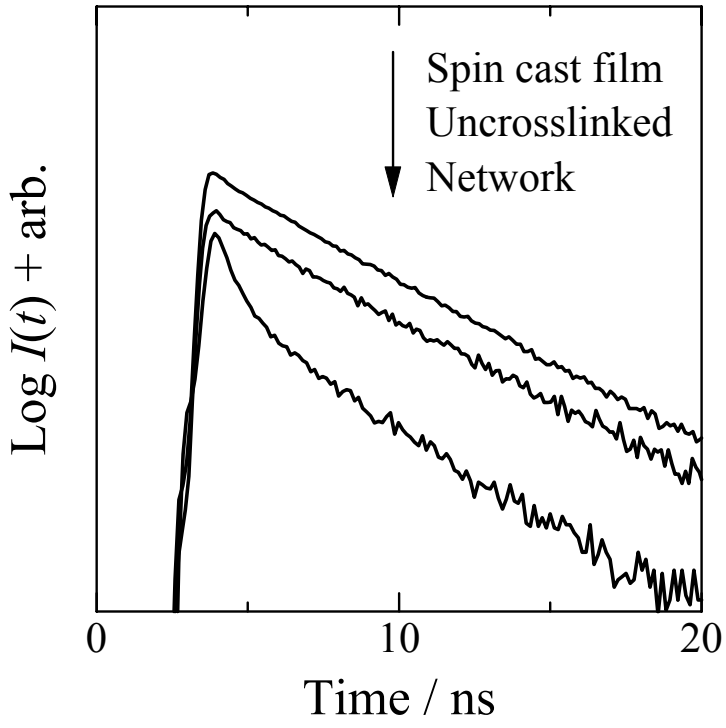

Figure 5.8. Near-field fluorescence decay curves for the spin-cast film, the uncrosslinked sample, and the polymer network sample. The average eosin concentration for each sample was 0.7 mM.

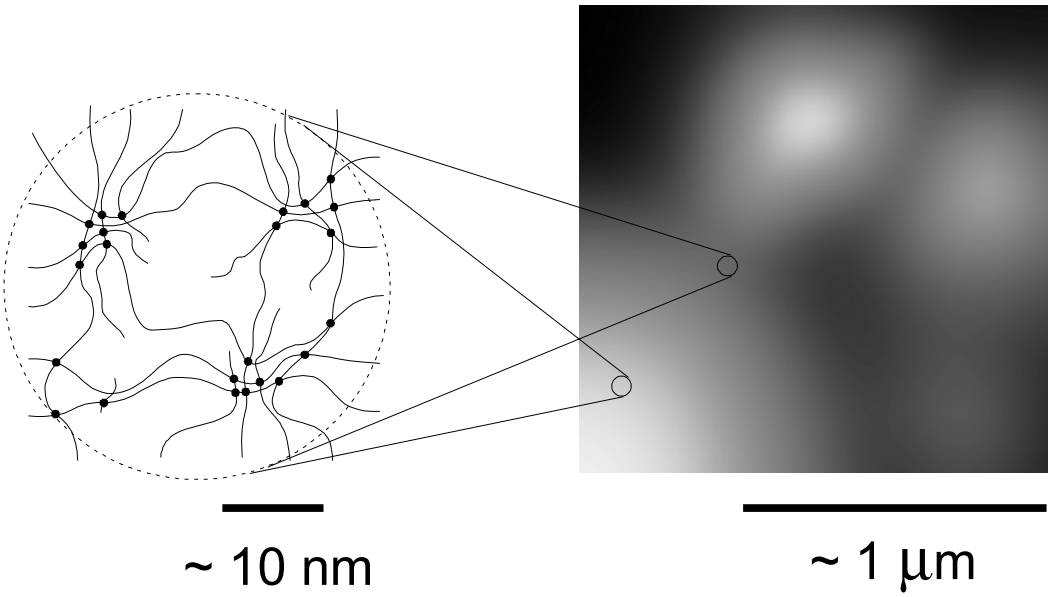

Figure 5.9. Schematic illustration for the inhomogeneous structure of the polymer network. The PMMA network has the structural hierarchy. On the molecular scale, the network chain forms a microcluster. The inhomogeneous structure in a submicron scale observed in SNOM images was induced by the heterogeneous connection of the microclusters.

5.4. CONCLUSION

The structural inhomogeneity of the PMMA network was studied by scanning near-field optical microscopy (SNOM). The spatial distribution of network chain segments and crosslinks could be directly imaged for optically transparent gels with a high resolution beyond the diffraction limit of light. SNOM allowed us to apply the energy transfer method to a nanometric local area. The energy transfer dynamics through the near-field time-resolved fluorescence technique indicated that the local segment density was higher than the ensemble average density of the network. The local density was independent of the heterogeneous structure in a submicron scale imaged by SNOM. This result indicates that the PMMA network has a hierarchical structure.

References and Notes

1. T. P. Hsu, D. S. Ma, and C. Cohen, *Polymer*, **24**, 1273 (1983).
2. N. Weiss, T. van Vliet, and A. Silberberg, *J. Polym. Sci., Polym. Phys. Ed.*, **17**, 2229 (1979).
3. A. M. Hecht, R. Duplessix, and E. Geissler, *Macromolecules*, **18**, 2167 (1985).
4. S. Mallam, F. Horkay, A. M. Hecht, and E. Geissler, *Macromolecules*, **22**, 3356 (1989).
5. E. Sato-Matsuo, M. Orkisz, S.-T. Sun, Y. Li, and T. Tanaka, *Macromolecules*, **27**, 6791 (1994).
6. M. Shibayama, T. Norisuye, and S. Nomura, *Macromolecules*, **29**, 8746 (1996).
7. F. Ikkai and M. Shibayama, *Phys. Rev. E*, **56**, 51 (1997).
8. M. Shibayama, F. Ikkai, Y. Shiwa, and Y. Rabin, *J. Chem. Phys.*, **107**, 5227 (1997).
9. F. Ikkai, M. Shibayama, and C. C. Han, *Macromolecules*, **31**, 3275 (1998).
10. Y. Rabin and S. Panyukov, *Macromolecules*, **30**, 301 (1997).
11. A. Suzuki, M. Yamazaki, and Y. Kobiki, *J. Chem. Phys.*, **104**, 1751 (1996).
12. A. Suzuki, M. Yamazaki, Y. Kobiki, and H. Suzuki, *Macromolecules*, **30**, 2350 (1997).
13. Y. Hirokawa, H. Jinnai, Y. Nishikawa, T. Okamoto, and T. Hashimoto, *Macromolecules*, **32**, 7093 (1999).
14. S. Ohmori, S. Ito, and M. Yamamoto, *Macromolecules*, **24**, 2377 (1991).
15. M. Mabuchi, K. Kawano, S. Ito, M. Yamamoto, M. Takahashi, and T. Masuda, *Macromolecules*, **31**, 6083 (1998).
16. H. Aoki, J. Horinaka, S. Ito, and M. Yamamoto, *Polym. Bull.*, **37**, 109 (1997).
17. A. D. Stein, D. A. Hoffman, C. W. Frank, and M. D. Fayer, *J. Phys. Chem.*, **96**, 3269 (1992).

18. J. P. S. Farinha, J. M. G. Martinho, S. Kawaguchi, A. Yekta, and M. A. Winnik, *J. Phys. Chem.*, **100**, 12552 (1996).
19. O. Tcherkasskaya, S. Ni, and M. A. Winnik, *Macromolecules*, **29**, 610 (1996).
20. E. Betzig and J. K. Trautman, *Science*, **257**, 189 (1992).
21. D. A. Vanden Bout, J. Kerimo, D. A. Higgins, and P. F. Barbara, *Acc. Chem. Res.*, **30**, 204 (1997).
22. H. Aoki, Y. Sakurai, S. Ito, and T. Nakagawa, *J. Phys. Chem. B*, **103**, 10553 (1999).
23. A. K. Dutta, P. Vanoppen, K. Jeuris, P. C. M. Grim, D. Pevenage, C. Salesse, and F. C. De Schryver, *Langmuir*, **15**, 607 (1999).
24. R. C. Dunn, *Chem. Rev.*, **99**, 2891 (1999).
25. B. Hecht, B. Sick, U. P. Wild, V. Deckert, R. Zenobi, O. J. F. Martin, and D. W. Pohl, *J. Chem. Phys.*, **112**, 7761 (2000).
26. J. D. McNeill, D. B. O'Connor, and P. F. Barbara, *J. Chem. Phys.*, **112**, 7811 (2000).
27. N. F. van Hulst, J. A. Veerman, M. F. Garcia-Parajo, and L. Kuipers, *J. Chem. Phys.*, **112**, 7799 (2000).
28. M. G. Krakovyak, T. D. Ananieva, and S. S. Skorokhodov, *Synth. Comm.*, **7**, 397 (1977).
29. M. Ohtsu, "Near-Field Nano/Atom Optics and Technology," Springer, Tokyo, 1998.
30. S. Mononobe, T. Saiki, T. Suzuki, S. Koshihara, and M. Ohtsu, *Opt. Commun.*, **146**, 45 (1998).
31. D. V. O'Cornner and D. Phillips, "Time-Correlated Single Photon Counting," Academic Press, London, 1984.
32. B. Hecht, H. Bielefeldt, Y. Inouye, D. W. Pohl, and L. Novotny, *J. Appl. Phys.*, **81**, 2492 (1997).

33. M. Hauser, U. K. A. Klein, and U. Gosele, *Z. Phys. Chem. NF*, **101**, 255 (1976).

34. A toluene solution of PMMA was prepared. The concentration was several percent by weight. Perylene and eosin monomer compounds were dissolved in the PMMA solution. The resulting solution was spin-cast on a cover glass. The near-field time-resolved measurements were carried out in the same manner as the case of the network samples.

35. W. P. Ambrose, P. M. Goodwin, J. C. Martin, and R. A. Keller, *Science*, **265**, 364 (1994).

36. X. S. Xie and R. C. Dunn, *Science*, **265**, 361 (1994).

37. R. X. Bian, R. C. Dunn, and X. S. Xie, *Phys. Rev. Lett.*, **75**, 4772 (1995).

Part II

NANOSECOND DYNAMICS STUDIED BY FLUORESCENCE DEPOLARIZATION METHOD

Chapter 6

LOCAL CHAIN DYNAMICS OF POLY(*N*-VINYLCARBAZOLE) STUDIED BY THE FLUORESCENCE DEPOLARIZATION METHOD

6.1. Introduction

Poly(*N*-vinylcarbazole) (PVCz) has been gathering much attention as a photofunctional polymer, and many fundamental[1-4] and practical[5-7] studies have been performed. For understanding the basis of photofunctional processes, the dynamic properties as well as the static properties of the polymer chain have to be fully understood.[3,4] Generally, the dynamics of polymers have been extensively studied from the theoretical[8-10] and experimental points of view. The local chain dynamics of flexible polymers has been experimentally studied by various techniques such as NMR,[11-13] ESR,[14] neutron scattering,[15] light scattering,[16,17] and fluorescence depolarization.[18-25] The time-resolved fluorescence depolarization method enables one to measure directly the orientational autocorrelation function of the fluorescent probe introduced into the polymer in a time range of 10^{-10} – 10^{-7} sec. We have examined the local dynamic behavior of the polymer chain by this method using a fluorescent probe introduced into the polymer chains of polystyrene (PS), poly(*cis*-1,4-isoprene) (PI), poly(oxyethylene) (POE), and poly(methyl methacrylate) (PMMA).[18-23] PVCz has bulky carbazolyl groups as the side chains. The static property of PVCz in dilute solutions[26-28] was investigated by several workers, however, few studies on the dynamic behavior of PVCz have been reported.[29] It is interesting to know the extent

to which the rotational relaxation of the polymer backbone is affected by the substituent.

In this chapter, the local chain dynamics of PVCz in dilute solutions was examined by the fluorescence depolarization method. The sample polymer was labeled at the middle of the chain with an anthracene probe by the coupling reaction of living ends of PVCz. The transition moment of the introduced probe lies along the main chain. Therefore, the obtained fluorescence anisotropy represents the orientational autocorrelation function for the middle segment of the main chain. The molecular weight dependence of the local motion of PVCz was examined in the Θ and good solvents, and the factors that govern the local chain dynamics were discussed. The characteristics of the dynamics of PVCz were also compared with those of other polymers.

6.2. EXPERIMENTS

6.2.1. Materials

Figure 6.1 shows the chemical structure of PVCz labeled with anthracene at the center of the chain. The double-headed arrow in Figure 6.1 indicates the transition moment for the anthracene group. The polymers were prepared by living cationic polymerization of *N*-vinylcarbazole initiated by HI in CH_2Cl_2 at –48 °C.[30] *N*-Vinylcarbazole (Nacalai Tesque) was recrystallized four times from hexane, and CH_2Cl_2 was doubly distilled before use. Anthracene was incorporated into the middle of the main chain by coupling the living ends of PVCz with 9,10-anthracenedithiol lithium salt, which was synthesized by addition of *n*-butyl lithium to 9,10-anthracenedithiol.[31] The GPC curve for the obtained polymer had two peaks. The peak at the lower molecular weight side was attributed to the PVCz chain unlabeled or

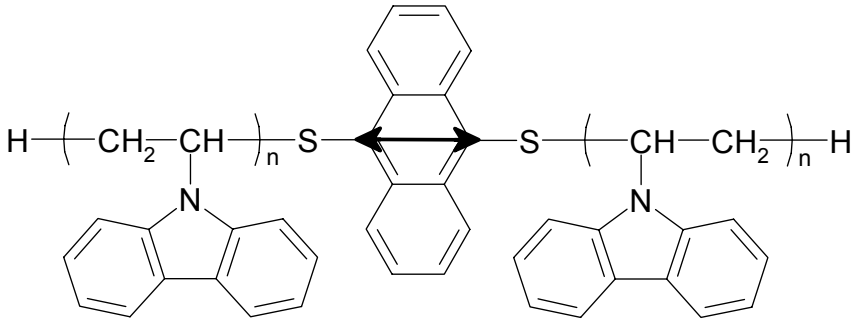

Figure 6.1. Molecular structure of PVCz labeled with anthracene at the center of the main chain. The double-headed arrow indicates the transition moment for the anthracene group.

Table 6.1. Characterization of The Samples

	$M_w \times 10^{-3}$	M_w/M_n
PVCz-09	9.2	1.12
PVCz-22	21.7	1.03
PVCz-42	41.6	1.06
PVCz-103	103	1.03

labeled at the one end. Only a higher molecular weight side peak, which was attributed to PVCz labeled at the chain center, was fractionated by GPC. The molecular weight was estimated from GPC measurement calibrated with the narrow molecular weight distributed PVCz standards whose molecular weights were determined by light scattering experiments. The fraction of racemic diads was estimated to be 0.63 independent of molecular weight from ^{1}H-NMR measurement.[32] Table 6.1 summarizes the weight-averaged molecular weights and the molecular weight distributions for the samples used in this study.

6.2.2. Fluorescence Depolarization Measurements

Toluene (Dojin, spectrophotomeric grade) and THF (Wako, guaranteed grade) were used as the solvents. Toluene was used without further purification, and THF was twice distilled before use. The concentration of the sample solution was ca. 10^{-5} M, so that the fluorescence depolarization due to the energy migration among anthracene probes[33] could be avoided. The solution was put into a quartz cell and degassed. The fluorescence anisotropy decay was measured by the time-correlated single photon counting technique.[34] A frequency-doubled Ti:sapphire laser (Tsunami, Spectra Physics) was used as a light source at a wavelength of 410 nm. The anthracene fluorescence from the sample was detected by a microchannel plate photomultiplier tube (R3809, Hamamatsu Photonics). The fluorescence signal and the excitation pulse signal detected by a photodiode (AR-S2, Antel Optronics) were inputted to a time-to-amplitude converter (Model 457, Ortec) as the start and stop signals, respectively. The fwhm of the instrumental function was ca. 60 ps. The fluorescence components parallel and perpendicular to the vertically polarized excitation pulse were measured alternately to avoid the data distortion due to the time drift. The measurement temperature was controlled within ± 0.1 °C by a water circulating system.

6.2.3. Data Analysis

The fluorescence anisotropy, $r(t)$, is defined as

$$r(t) = \frac{I_{\parallel}(t) - I_{\perp}(t)}{I_{\parallel}(t) + 2I_{\perp}(t)}, \tag{6.1}$$

where $I_{\parallel}(t)$ and $I_{\perp}(t)$ are the parallel and perpendicular component of the fluorescence intensity to the excitation polarization direction, respectively. The relaxational process of the polymer chain consists of various motional modes, so $r(t)$ may consist of the sum of two or more exponential functions. However, practically, the experimental

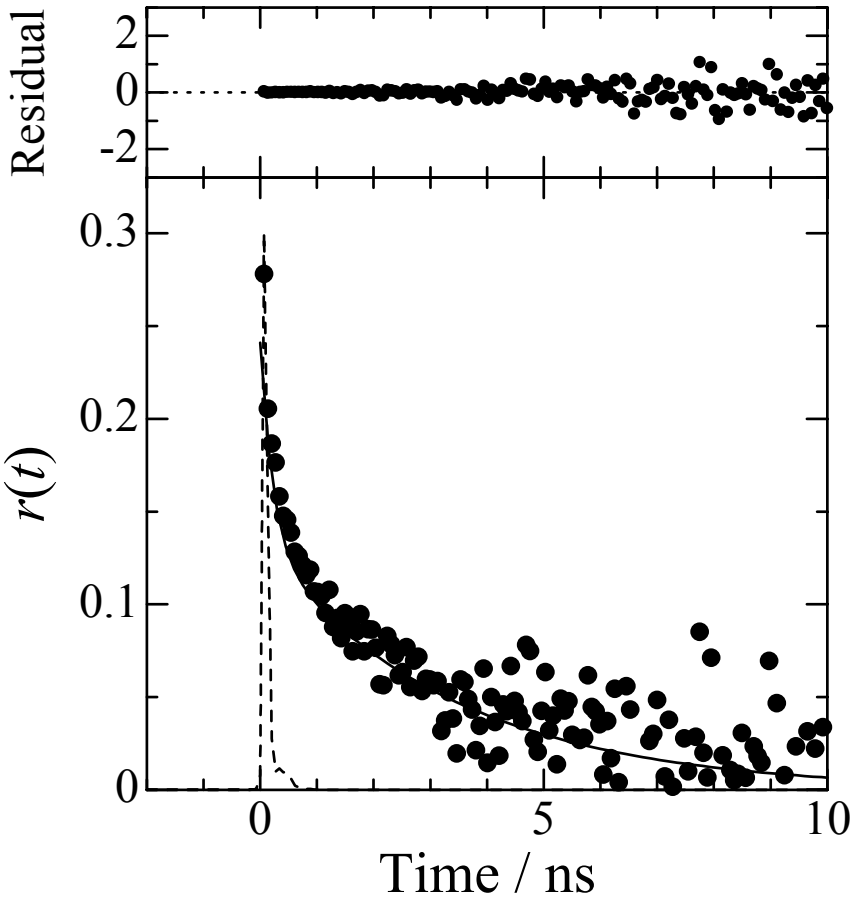

Figure 6.2. A fitting example of $r(t)$ with two-component exponential functions. The filled circles are observed $r(t)$ for PVCz-42 in THF at 17.4 °C. The broken and solid lines indicate the instrumental function and the fitting curve, respectively. The fitting parameters are $r_0 = 0.241$, $x = 0.554$, $T_1 = 3.34$ ns, and $T_2 = 0.225$ ns.

data fitted well to a double exponential function,

$$r(t) = r_0\left[x\exp\left(-\frac{t}{T_1}\right) + (1-x)\exp\left(-\frac{t}{T_2}\right)\right], \tag{6.2}$$

where $T_1 > T_2$. Figure 6.2 shows a fitting example of $r(t)$ for PVCz-42 in THF solvent

at 17.4 °C, where the longer and shorter component of the relaxation time, T_1 and T_2, were 3.34 ns and 0.225 ns, respectively, with the fraction of the longer component x = 0.554. The ratio of T_1 to T_2 and the fraction x were nearly independent of temperature, but dependent on the solvent. The detailed behavior of T_1, T_2, and x, i.e., the physical meaning of these parameters is being studied and will be reported later. In this study, the mobility of the polymer chain was discussed in terms of the mean relaxation time, T_m, defined as eq. 6.3 and calculated by eq. 6.4.

$$T_m = r_0^{-1} \int_0^\infty r(t)\mathrm{d}t \tag{6.3}$$

$$= xT_1 + (1-x)T_2 \tag{6.4}$$

6.3. RESULTS AND DISCUSSION

6.3.1. Reduced Relaxation Time

The previous studies showed that the relaxation time for the local motion of polymers in a low viscosity solvent, < 1 cP, is proportional to the solvent viscosity, η.[19,24,35] Hence, the local dynamics of a polymer chain can be discussed in terms of the reduced relaxation time, T_m/η. Figure 6.3 shows the molecular weight dependence of T_m/η for the toluene and THF solutions at 37 °C. In this plot, the reduced relaxation time for 9,10-dimethylanthracene is also indicated as a diamond symbol. The value of T_m/η for 9,10-dimethylanthracene, which provides the limiting value for low molecular weight PVCz, was estimated to be ca. 0.04 ns cP^{-1} from the steady state fluorescence anisotropy measurement. Toluene is a Θ solvent at 37 °C, and THF is a good solvent.[26,27] In THF, the value of T_m/η increased with the increase of molecular weight in the low molecular weight region. In this region, it seems that both the local

backbone motion and the entire rotational motion of the polymer chain contribute to the mean relaxation time. Then, the reduced relaxation time asymptotically reached T_m/η = 2.3 ns cP^{-1} at M_w = 25,000. The saturation of T_m/η in the high molecular weight region indicates that the fluorescence depolarization method measures the local motion of the PVCz backbone which occurs within the scale of the molecular weight of 25,000. The value of T_m/η for the toluene solution also increased with the increase of molecular weight in the range of M_w < ca. 50,000, and gradually reached a constant value, T_m/η = 3.6 ns cP^{-1}. Waldow et al. examined the local motion of PI by the fluorescence depolarization method and showed that the relaxation time increased with the increase of molecular weight in a Θ solvent while the relaxation time was independent of molecular weight in a good solvent. They explained the molecular weight dependence of the relaxation time for PI in terms of the chain segment density around the fluorescent probe.[36] In the case of PVCz, the value of T_m/η in the Θ state tended to be almost constant in a range of M_w > 50,000, whereas the segment density at the center of the unperturbed chain monotonically increased with the increase of molecular weight.[36] This indicates that the local chain dynamics cannot be explained merely from the viewpoint of the segment density. The motional modes for the local chain dynamics consist of the conformational transition across a potential barrier and the librational motion within a potential well.[10] Recent molecular dynamics simulations showed that the libration plays an important role in the local chain motion as well as the conformational transition.[37-39] Because the libration is the motion that occurs within a potential well, it is dependent upon the shape of the local potential. The local motion of the polymer chain on a nanosecond scale is influenced by the potential energy, which is affected by the solvent condition as well as by the molecular structure of the polymer.

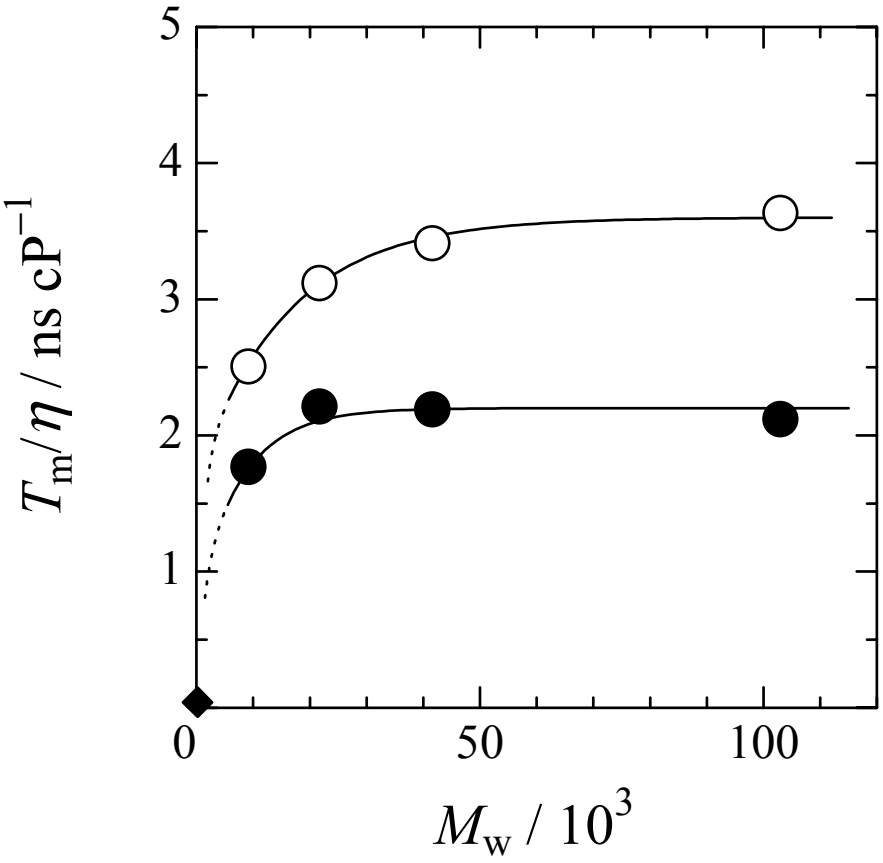

Figure 6.3. Molecular weight dependence of the reduced relaxation time, T_m/η, at 37 °C. The open and filled circles indicate the data for the toluene and THF solutions, respectively. A diamond symbol (◆) indicates the reduced relaxation time for 9,10-dimethylanthracene estimated from a steady state fluorescence depolarization measurement.

Now we consider the difference in T_m/η for PVCz in the two solvents in the range of M_w < 20,000. Abe et al. studied the excluded-volume effect in a wide molecular weight range. They examined the solvent dependence of the mean-square radius of gyration, $\langle S^2 \rangle$, and the intrinsic viscosity, $[\eta]$, for PS and PMMA.[40,41] They showed that the values of $\langle S^2 \rangle$ or $[\eta]$ were almost independent of the solvent condition in the oligomer region, indicating that the chain dimension even in a good solvent agreed with that of the unperturbed polymer chain for the two polymers. Therefore, it seems reasonable to be said that the dimensions and conformations of PVCz in toluene, Θ solvent, is similar to those in THF, a good solvent, in the low molecular weight region. If the local motion were governed only by the segment density, the reduced relaxation times in Θ and good solvents would be the same in the oligomer region. As shown in Figure 6.3, the reduced relaxation time, T_m/η, for PVCz in the low molecular weight region was dependent on the solvent quality. This indicates that the contribution of the segment density and the chain conformation is small and that the local motion of PVCz is affected by the local potential energy. Then, it is probable that the solvent quality affects the potential energy, that is, the poor solvent quality probably causes the high potential energy, resulting in a large reduced relaxation time in a Θ solvent. The behavior of T_m/η in the toluene and THF solutions had a different critical molecular weight, M_c, which is defined as the molecular weight where the reduced relaxation time reaches an asymptotic value. The value of M_c in toluene was larger than that in THF, that is, the values of T_m/η increased more gradually with the increase of molecular weight in toluene than in THF. Therefore, the mobility of the chain center is affected partly by the segment density in addition to the local potential.

6.3.2. Activation Energy

The activation energy for the local segmental motion, E^*, was estimated according to Kramers' diffusion limit.[9,42] The velocity coefficient, k, of a particle is

expressed as

$$k = \zeta^{-1} \exp\left(-\frac{E}{RT}\right), \tag{6.5}$$

where ζ and E are the frictional coefficient and a potential energy barrier, respectively. According to Stokes' law, the relaxation time, T_m, and the solvent viscosity, η, are proportional to k^{-1} and ζ, respectively. Thus, T_m/η is expressed as

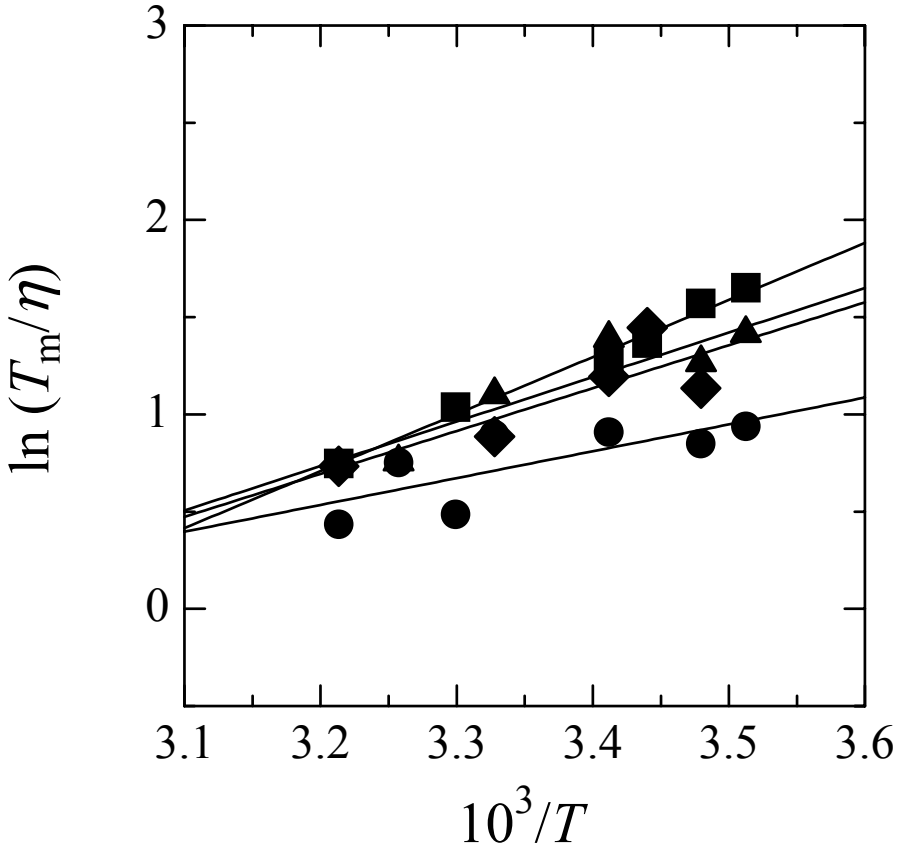

Figure 6.4. Arrhenius plots of T_m/η for PVCz-09(●), -22(▲), -42(■), -103(◆) in THF solvent.

$$T_m/\eta = A\exp\left(\frac{E^*}{RT}\right), \tag{6.6}$$

where R and T are the gas constant and the absolute temperature, respectively. Figure 6.4 shows the Arrhenius plot of T_m/η for PVCz in the THF solvent. The value of E^* was evaluated from the slope of this plot. The relationship between E^* for the THF solution and the molecular weight is shown in Figure 6.5. The molecular weight dependence of E^* was similar to that of T_m/η, that is, the value of E^* for the THF

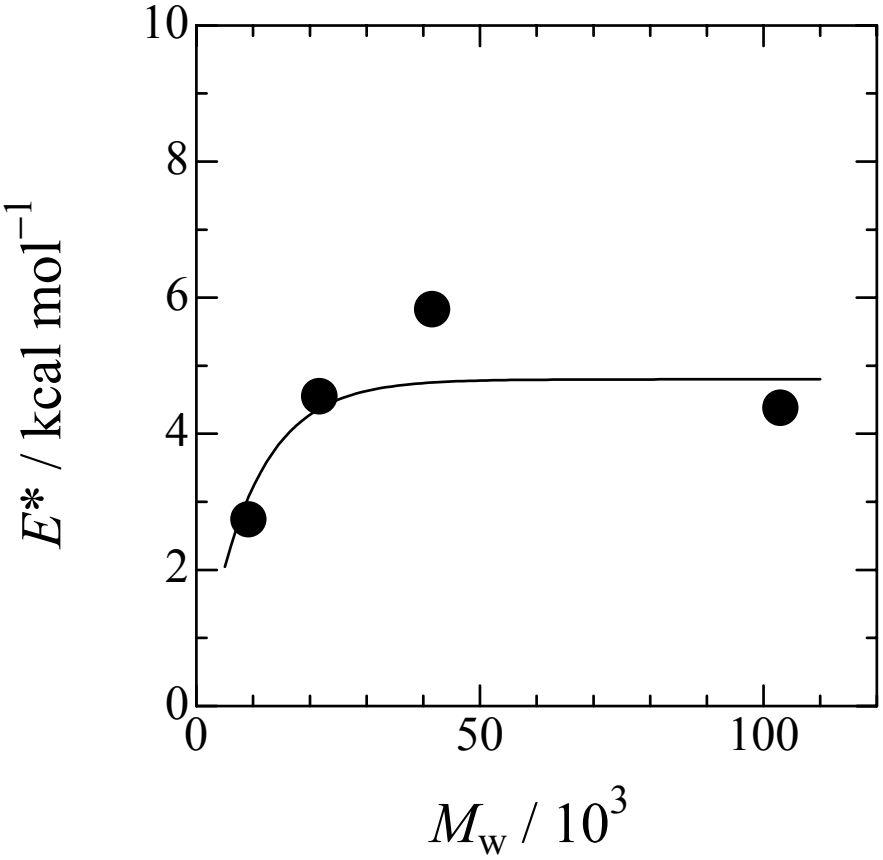

Figure 6.5. Molecular weight dependence of the activation energy, E^*, for PVCz in THF. The value of E^* was evaluated from the slope of the Arrhenius plot in Figure 6.4.

solution was saturated at M_w = 24,000. On the other hand, the activation energy obtained for PVCz in toluene above the Θ temperature, 37 °C, was considerably scattered due to high temperature. The value of E^* obtained below the Θ temperature did not reflect the activation energy for the local segmental motion of PVCz because of the poor solubility, so the activation energy in toluene is not discussed here.

6.3.3. Comparison with Other Polymers

The reduced relaxation time and the activation energy for PVCz were compared with those for other polymers: POE,[18] PI,[19] PS,[20,21] and *s*-PMMA.[22] All the polymers were labeled with anthracene group at the center of the main chain, and they had sufficiently large molecular weights. Table 6.2 shows the reduced relaxation time at 20 °C and the activation energy for each polymer in a good solvent evaluated by the fluorescence depolarization method. For comparison of the reduced relaxation time for each polymer, it should be noted that the PVCz was labeled with the anthracene group through C-S bonds, i.e., ~CHX-S-An-S-CHX~ (X and An indicate a substituent and anthracene, respectively), whereas the anthracene moieties for the others were introduced through methylene bonds (~CHX-CH_2-An-CH_2-CHX~). In the previous study, it was reported that the relaxation time is influenced by the chemical structure around the anthracene probe.[43] It is expected that bond rotation is more likely to occur around a CH_2-S bond than that around a CH_2-CH_2 bond due to the lower rotational potential barrier for the CH_2-S bond than that for the methylene bond. Hence, the reduced relaxation time for PVCz evaluated in this study was probably underestimated because of the structure around the anthracene probe. The value of T_m/η for PVCz was larger than that for PS and smaller than that for *s*-PMMA. However, considering the difference in the chemical structure around the anthracene probe, it is reasonable to say that the chain mobility of PVCz is similar to that of *s*-PMMA at least. Therefore, it can be said that the relaxation time for the PVCz chain

is fairly larger than those for the other polymers. The activation energy for PVCz is also larger than those for the others. These results indicate that the PVCz chain is less mobile and dynamically stiffer compared to the other polymers. This is attributed to the steric hindrance of the bulky carbazolyl side chain. Consequently, the rotational potential barrier for the conformational transition is high and the rotational motion is suppressed.

The molecular weight effect on the relaxation time for POE and PS in good solvents was examined in detail.[18,20] Now, the molecular weight dependence of local chain dynamics is discussed in terms of the critical number of bonds, N_c, which is the number of bonds corresponding to the critical molecular weight, M_c. M_c is the

Table 6.2. Reduced Relaxation Time Measured at 20 °C and Activation Energy for Other Polymers in Good Solvents

	Solvent	T_m/η / ns cP^{-1}	E^* / kcal mol^{-1}
POE	DMF	0.27	1.1
PI	Benzene	1.4	1.3
	o-Xyrene	1.1	1.2
PS	Benzene	3.1	1.7
	Toluene	3.2	1.4
	Ethylbenzene	3.2	1.3
s-PMMA	Benzene	4.5	2.7
	Chloroform	4.5	2.4
PVCz	THF	3.8	4.5

molecular weight where the reduced relaxation time reaches an asymptotic value. The relaxation time for PS in benzene reached the saturation value at $M_w \cong 10{,}000$, which corresponds to $N_c = 200$. Similarly, N_c for POE in a good solvent, DMF, is estimated to be 70. On the other hand, the relaxation time for PVCz in THF was constant above a molecular weight of 25,000, which corresponds to $N_c \cong 260$. The rotational motion along the polymer backbone occurs cooperatively. If a rotational motion took place along the main chain, counter rotations around the other bonds would cooperatively occur to avoid the movement of the large part of the polymer chain. This mechanism may consist of conformational transitions and librational motions.[10] The value of N_c for PVCz is greater than those for POE and PS. This indicates that the cooperative counter rotations for PVCz spread along the main chain in a longer range than those for POE and PS. Because the rotational motion around each bond for the PVCz backbone is suppressed due to the large steric hindrance of the carbazolyl group, the cooperative rotational motion occurs at more C–C bonds in a longer length scale along the backbone to localize the 'triggering' rotational transition, resulting in the larger critical number of bonds, N_c, compared to POE and PS.

6.4. CONCLUSION

PVCz labeled with anthracene at the middle of the main chain was synthesized by the living cationic polymerization followed by the coupling reaction of the living ends with 9,10-anthracenedithiol lithium salt. The local chain dynamics of PVCz at the chain center was examined by the fluorescence depolarization method. The molecular weight effect upon the relaxation time and the activation energy for the local segmental motion was evaluated in the range of molecular weight from 9,200 to 103,000. The molecular weight and solvent dependence of the reduced relaxation time indicates that

the local potential energy for the conformational transition is an important factor governing the local motion of PVCz. The values of the reduced relaxation time and the activation energy for PVCz were large compared to those for the other polymers: POE, PI, PS, and *s*-PMMA. Such high relaxation time and activation energy result from the suppression of the rotational motion of the backbone C–C bonds by bulky carbazolyl side chains.

References

1. Y. Tsujii, A. Tsuchida, Y. Onogi, and M. Yamamoto, *Macromolecules*, **23**, 4019 (1990).
2. A. Tsuchida, A. Nagata, M. Yamamoto, H. Fukui, M. Sawamoto, and T. Higashimura, *Macromolecules*, **28**, 1285 (1995).
3. H. Sakai, A. Itaya, H. Masuhara, K. Sasaki, and S. Kawata, *Polymer*, **37**, 31 (1996).
4. H. Miyasaka, T. Moriyama, and A. Itaya, *J. Phys. Chem.*, **100**, 12609 (1996).
5. T. Kawakami and N. Sonoda, *Appl. Phys. Lett.*, **62**, 2167 (1993).
6. S. M. Silence, C. A. Walsh, D. M. Burland, R. J. Twieg, W. E. Moerner, and M. C. J. M. Donckers, *Appl. Opt.*, **33**, 2218 (1994).
7. M. D. Rahn, D. P. West, and J. D. Shakos, *J. Appl. Phys.*, **87**, 627 (2000).
8. H. Yamakawa, "Helical Wormlike Chains in Polymer Solutions," Springer, Berlin, 1997.
9. E. Helfand, *J. Chem. Phys.*, **54**, 4651 (1971).
10. G. J. Moro, *J. Chem. Phys.*, **97**, 5749 (1992).
11. S. Glowinkowski, D. J. Gisser, and M. D. Ediger, *Macromolecules*, **23**, 3520 (1990).
12. W. Zhu and M. D. Ediger, *Macromolecules*, **28**, 7549 (1995).
13. C. Baysal, B. Erman, I. Bahar, F. Laupretre, and L. Monnerie, *Macromolecules*, **30**, 2058 (1997).
14. A. T. Bullok, G. G. Cameron, and P. M. Smith, *J. Phys. Chem.*, **77**, 1635 (1973).
15. T. Kanaya, T. Kawaguchi, and K. Kaji, *Macromolecules*, **32**, 1672 (1999).
16. T. Takaeda, T. Yoshizaki, and H. Yamakawa, *Macromolecules*, **27**, 4248 (1994).
17. A. K. Rizos and K. L. Ngai, *Macromolecules*, **31**, 6217 (1998).
18. J. Horinaka, S. Amano, H. Funada, S. Ito, and M. Yamamoto, *Macromolecules*,

31, 1197 (1998).

19. K. Ono, K. Ueda, and M. Yamamoto, *Polym. J.*, **26**, 1345 (1994).
20. J. Horinaka, H. Aoki, S. Ito, and M. Yamamoto, *Polym. J.*, **31**, 172 (1999).
21. K. Ono, Y. Okada, S. Yokotsuka, T. Sasaki, and M. Yamamoto, *Macromolecules*, **27**, 6482 (1994).
22. J. Horinaka, K. Ono, and M. Yamamoto, *Polym. J.*, **27**, 429 (1995).
23. M. Yamamoto, J. Horinaka, H. Aoki, K. Tawa, and S. Ito, *J. Soc. Rheol. Jpn.*, **25**, 203 (1997).
24. D. A. Waldow, M. D. Ediger, Y. Yamaguchi, Y. Matsushita, and I. Noda, *Macromolecules*, **24**, 3147 (1991).
25. S. Adams and D. B. Adolf, *Macromolecules*, **31**, 5794 (1998).
26. N. Kuwahara, S. Higashida, M. Nakata, and M. Kaneko, *J. Polym. Sci. A2*, **7**, 285 (1969).
27. G. Sitaramaiah and D. Jacobs, *Polymer*, **11**, 165 (1970).
28. L. M. Leon, I. Katime, and M. Rodriguez, *Eur. Polym. J.*, **15**, 29 (1979).
29. A. Karali, P. Dais, and F. Heatley, *Macromolecules*, **33**, 5524 (2000).
30. M. Sawamoto, J. Fujimori, and T. Higashimura, *Macromolecules*, **20**, 916 (1987).
31. E. Kobayashi, J. Jiang, H. Ohta, and J. Furukawa, *J. Polym. Sci., A, Polym. Chem.*, **28**, 2641 (1990).
32. A. Abe, H. Kobayashi, T. Kawamura, M. Date, T. Uryu, and K. Matsuzaki, *Macromolecules*, **21**, 3414 (1988).
33. N. Sato, S. Ito, K. Sugiura, and M. Yamamoto, *J. Phys. Chem. A*, **103**, 3402 (1999).
34. D. V. O'Cornner and D. Phillips, "Time-Correlated Single Photon Counting," Academic Press, London, 1984.
35. S. P. Velsko, D. H. Waldeck, and G. R. Fleming, *J. Chem. Phys.*, **78**, 2735 (1983).

36. D. A. Waldow, B. S. Johnson, P. D. Hyde, M. D. Ediger, T. Kitano, and K. Ito, *Macromolecules*, **22**, 1345 (1989).
37. N. E. Moe and M. D. Ediger, *Macromolecules*, **29**, 5484 (1996).
38. M. M. Fuson and M. D. Ediger, *Macromolecules*, **30**, 5704 (1997).
39. C. Baysal, A. R. Atilgen, B. Erman, and I. Bahar, *Macromolecules*, **29**, 2510 (1996).
40. F. Abe, Y. Einaga, T. Yoshizaki, and H. Yamakawa, *Macromolecules*, **26**, 1884 (1993).
41. F. Abe, K. Horita, Y. Einaga, and H. Yamakawa, *Macromolecules*, **27**, 725 (1994).
42. H. A. Kramers, *Physica*, **7**, 284 (1940).
43. J. Horinaka, S. Ito, M. Yamamoto, Y. Tsujii, and T. Matsuda, *Macromolecules*, **32**, 2270 (1999).

Chapter 7

LOCAL MOTION OF CROSSLINKS FOR POLY (METHYL METHACRYLATE) GELS STUDIED BY THE FLUORESCENCE DEPOLARIZATION METHOD

7.1. INTRODUCTION

In a gel, polymer chains are connected to each other by crosslinks, and it is expected that the motion, such as the translational and the rotational diffusion, of a chain is restricted compared to that of a linear chain. A gel has characteristic properties different from those of a concentrated solution and a bulk.[1] So far, many workers have studied macroscopic properties of gels such as swelling behavior[2,3] and mechanical behavior.[4-7] The macroscopic properties of polymer networks are governed by the molecular-scale dynamics at crosslinks.[8] Therefore it is important to understand the local motion of a gel from a microscopic point of view. Recently, gels have been studied by means of various methods: e.g., light scattering,[9-11] small angle neutron scattering,[12] NMR,[13,14] and fluorescence techniques.[15-18] Advances in experimental techniques enabled us to get information about microscopic structure and dynamics of polymer gels. Different techniques probe the polymer chain motion occurring on different time scales.[19-21] Among them, the fluorescence depolarization method enables one to measure directly the orientational autocorrelation function in a time range of 10^{-10} – 10^{-7} sec. Since the conformational transitions of the polymer chain occur in a time range of subnanosecond, the relaxation process measured by this

method reflects the local motion of the polymer chains.[22-31] With respect to the local chain dynamics in dilute solutions, Horinaka et al.[28,29] and the previous chapter showed that the local potential for the chain conformation has to be considered in discussing the local motion of polystyrene and poly(*N*-vinylcarbazole) in dilute solutions. It is interesting to examine the local motion of gels because it is expected that the dynamics of gels is different from that of polymer solutions due to crosslinking. In the current chapter, the local motion of crosslinks for PMMA gels was examined. The relaxation time of the local motion was measured in various solvents at swelling equilibrium states for the PMMA gels with different molecular weights between crosslinks by means of the time-resolved fluorescence depolarization method. The activation energy for the local motion was estimated, and the factors that govern the local motion of crosslinks was discussed.

7.2. EXPERIMENTS

7.2.1. Materials

Anthracene-labeled PMMA gels (Figure 7.1) were prepared by the free radical copolymerization of methyl methacrylate (MMA; Wako Pure Chemical Industries), ethylene glycol dimethacrylate (EGDMA; Wako Pure Chemical Industries), and 9,10-anthrylenedimethyl dimethacrylate (AnDMA). α,α'-Azobisisobutyronitrile (AIBN; Nacalai Tesque) and distilled toluene were used as initiator and solvent, respectively. All the reagents for polymerization were purified before use. AnDMA was synthesized from 9,10-bis(chloromethyl)anthracene (bis(ClMe)An; Tokyo Chemical Industries) and methacrylic acid (MAA; Wako Pure Chemical Industries).[32,33] Bis(ClMe)An was recrystallized from toluene, and MAA was used as received. The feed ratios of EGDMA to MMA, f_c, were set at 0.3, 0.5, 1.0, 3.0, and 5.0 mol-%. The

polymerization was carried out in toluene with [MMA] = 4 M, [AIBN] = 2.8×10^{-2} M, and [AnDMA] = ca. 10^{-5} M for 15 h at 60 °C in glass tubes under vacuum. The conversion of the polymerization was about 95 %. Then, the obtained gels were immersed in toluene (Nacalai Tesque, spectrophotomeric grade) at room temperature to extract unreacted monomers and sol fraction. The extraction was repeated until the emission of anthracene in the range of 400 – 480 nm was no longer measured from the decanted toluene. The concentration of anthracene probe was less than 10^{-5} M in each gel, so the fluorescence depolarization due to excitation energy migration was negligible. The sample gel of f_c = 0.5 mol-% was swollen to the equilibrium state in four kinds of solvents: toluene, chloroform (Dojin, spectrophotomeric grade), acetone (Nacalai Tesque, spectrophotomeric grade), and acetonitrile (Nacalai Tesque, spectrophotomeric grade). The sample of f_c = 3.0 mol-% was swollen in toluene and acetonitrile. The other samples were swollen in toluene. All the samples were macroscopically homogeneous and optically clear.

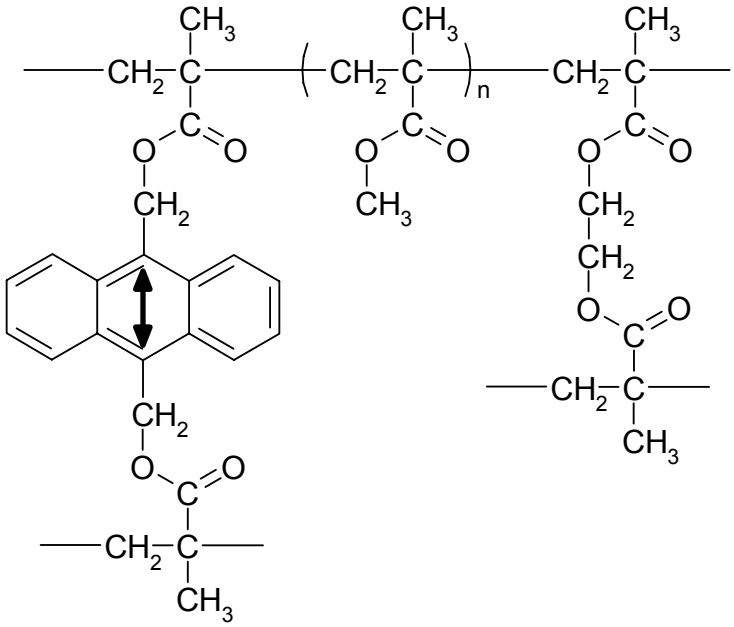

Figure 7.1. PMMA gels labeled at crosslinks with anthracene. The double-headed arrow indicates the direction of the transition moment of anthracene.

Table 7.1. Crosslinking Agent Fraction, f_c, Molecular Weight Between Crosslinks, M_c, and Swelling Ratio, V/V_0, at 20°C

Sample	f_c / %	$M_c \times 10^{-3}$	V/V_0
PMMA-1.0/toluene	1.0	14	2.85
PMMA-0.5/toluene	0.5	53	4.57
PMMA-0.3/toluene	0.3	120	7.25
PMMA-0.5/chloroform	0.5	53	7.79
PMMA-0.5/acetone	0.5	53	4.13
PMMA-0.5/acetonitrile	0.5	53	2.18
PMMA-3.0/toluene	3.0	1.9	1.18
PMMA-3.0/acetonitrile	3.0	1.9	0.79
PMMA-5.0/toluene	5.0	1.1	0.98

7.2.2. Equilibrium Swelling Measurements

The molecular weight between crosslinks, M_c, was determined from the polymer volume fraction at the swelling equilibrium state for each gel (f_c = 0.3, 0.5 1.0, 3.0, and 5.0 %) swollen in toluene using the Flory-Rehner equation.[34] The Flory-Huggins interaction parameter was estimated to be 0.43 from the value of the second virial coefficient for PMMA/toluene solution reported in the literature.[35] The swelling ratio, V/V_0, was defined as

$$\frac{V}{V_0} = \left(\frac{d}{d_0}\right)^3, \tag{7.1}$$

where V and d is the volume and the diameter of the sample at the equilibrium swelling state, respectively, and V_0 and d_0 are those for the gel just after preparation. V/V_0 for

the samples of f_c = 0.3, 0.5, and 1.0 % was measured as a function of temperature from 10 to 40 °C. The molecular weights between crosslinks, M_c, and the swelling ratios, V/V_0, at 20°C for all the samples are given in Table 7.1. A sample is denoted by PMMA-f_c/swelling solvent in Table 7.1.

7.2.3. Time-Resolved Fluorescence Measurements and Analysis

Time-resolved fluorescence depolarization measurements were carried out by the single-photon counting system.[24,36] The second harmonic of a Ti:sapphire laser (Spectra Physics, Tsunami) was used as a light source. The wavelength was 396 nm. The instrumental function had a full width at half maximum of ca. 60 ps. The excitation pulse was polarized vertically, and the parallel fluorescence component, $I_{\parallel}(t)$, and the perpendicular one, $I_{\perp}(t)$, were measured alternately to avoid data distortions due to the time drift. The time-resolved fluorescence measurement was made at the swelling equilibrium state for each sample. The measurement of the gels of f_c = 3.0 and 5.0 % was made only at 20 °C. For the other samples, the temperature range of measurement was from 10 to 40 °C. The temperature was kept constant for more than 2 days to ensure the establishment of the swelling equilibrium before the measurements.

The fluorescence anisotropy ratio, $r(t)$, is defined as

$$r(t) = \frac{I_{\parallel}(t) - I_{\perp}(t)}{I_{\parallel}(t) + 2I_{\perp}(t)}. \tag{7.2}$$

We convoluted a double-exponential function, eq 7.3, with the instrumental function to analyze the anisotropy ratio, $r(t)$, and fitted it to the experimental anisotropy data by the method of nonlinear-least-squares.[22]

$$r(t) = r_0\left[x\exp\left(-\frac{t}{T_1}\right) + (1-x)\exp\left(-\frac{t}{T_2}\right)\right] \tag{7.3}$$

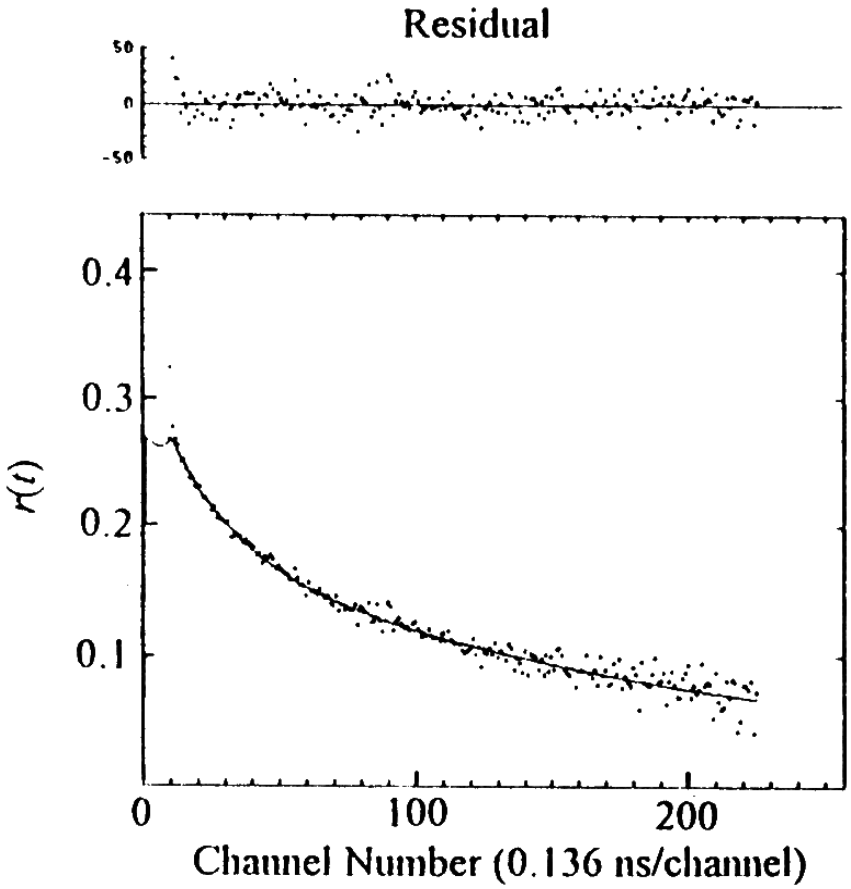

Figure 7.2. Fluorescence anisotropy decay measured for PMMA-0.5/toluene at 20°C. The dots are the experimental data and the solid line is the fitting curve obtained by the method of nonlinear-least-squares: $r(t) = 0.268\ [\ 0.676\ \exp(-t / 27.8) + 0.324\ \exp(-t / 3.14)]$.

Eq. 7.3 is an empirical equation, but it fitted the experimental data very well for all the samples. Figure 7.2 shows an example of $r(t)$ data fitting with eq. 7.3. The mean relaxation time, T_m, is defined as eq. 7.4 and calculated by eq. 7.5 with the best-fit values of x, T_1, and T_2.

$$T_m = r_0^{-1} \int_0^\infty r(t)dt \tag{7.4}$$

$$= xT_1 + (1-x)T_2 \tag{7.5}$$

7.3. RESULTS AND DISCUSSION

7.3.1 Reduced Relaxation Time

The local dynamics of gels at crosslinks is discussed in terms of the viscosity reduced mean relaxation time, T_m/η, where η is the solvent viscosity. Figure 7.3 shows a relationship between T_m/η and V/V_0 for PMMA gels at 20°C. Also shown in Figure 7.3 are the data points for the samples with different M_c's. It is obvious from Figure 7.3 that T_m/η decreased as V/V_0 and M_c increased, i.e., the mobility at crosslinks became greater with the increase of V/V_0 and M_c. First, we compared the mobility of PMMA-0.5s swollen in four kinds of solvents (open symbols in Figure 7.3) to evaluate the effect of V/V_0 on the local motion. The local motion of PMMA-0.5 at crosslinks became faster with the increase of V/V_0, while M_c was the same for these samples. Secondly, the mobility for PMMA-0.5/chloroform (symbol, □, in Figure 7.3) and PMMA-0.3/toluene (▼) was compared in terms of V/V_0, M_c, and T_m/η. V/V_0 for PMMA-0.5/chloroform and that for PMMA-0.3/toluene were approximately the same, i.e., 7.79 and 7.25, respectively, while M_c of PMMA-0.5 was 2.3 times lower than that of PMMA-0.3. The mobility of PMMA-0.5/chloroform at crosslinks was roughly the same as that of PMMA-0.3/toluene, that is, the values of T_m/η were 15.8 and 22.0 ns/cP, respectively. This indicates that the mobility of a gel at crosslinks is the same when its swelling ratio is kept constant, even though the molecular weights between crosslinks M_c, are different. It was experimentally found that T_m/η is proportional to the power of V/V_0 for the gels with the same M_c. The data for the samples except

PMMA-5.0/toluene (×) lie on one line independently of M_c and the swelling solvent. Therefore, it can be said that the mobility of a gel at crosslinks is dependent on its swelling ratio and independent of the solvent and the molecular weight between crosslinks in the case of large M_c. It was reported that the local motion of polymer chains in solutions is mainly governed by the local potential for the chain conformation

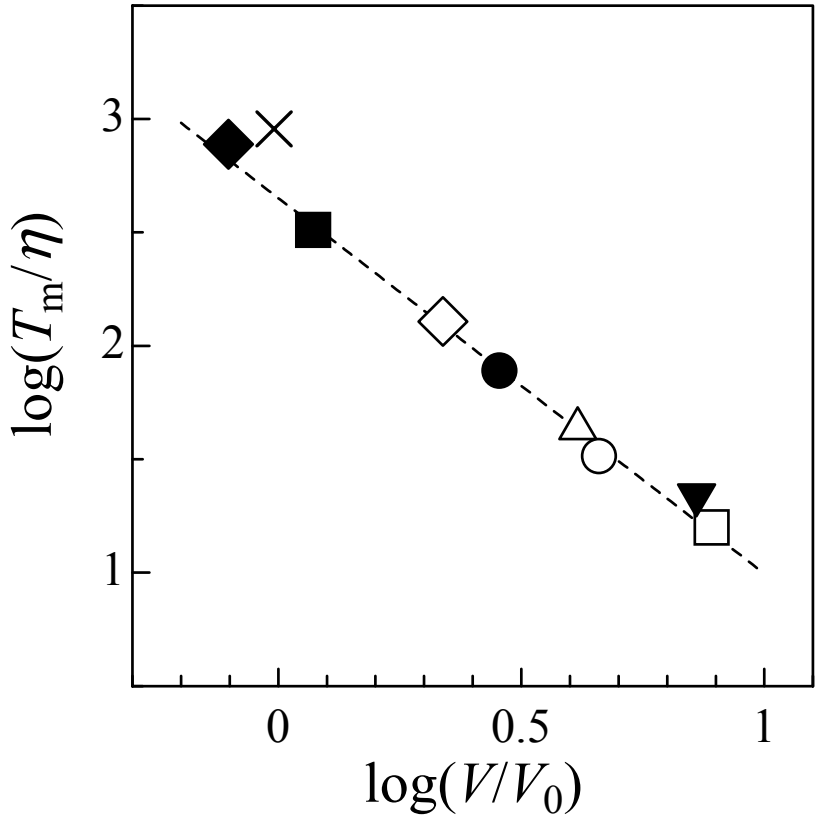

Figure 7.3. Relationship between reduced relaxation time and swelling ratio for PMMA gels. Symbols: ▼, PMMA-0.3/toluene; ○, PMMA-0.5/toluene; ●, PMMA-1.0/toluene; □, PMMA-0.5/chloroform; △, PMMA-0.5/acetone; ◇, PMMA-0.5/acetonitrile; ■, PMMA-3.0/toluene; ◆, PMMA-3.0/acetonitrile; ×, PMMA-5.0/toluene.

dependent upon the solvent quality.[28,29] In the case of the PMMA gels, four network chains converge at a crosslinking points, therefore, the local motion at crosslinks is probably susceptible to the network chain concentration. The increase of the swelling ratio results in the high chain segment density around the crosslinks. Thus, the mobility at crosslinks is affected by the segment density in the vicinity of the crosslinks.

7.3.2. Activation Energy

The activation energy for the local motion, E^*, was estimated by the theory of Kramer's diffusion limit.[37] In this theory, the activation energy, E^*, is related to the reduced relaxation time and the temperature by the following equation.

$$\frac{T_m}{\eta} = A \exp\left(\frac{E^*}{RT}\right), \tag{7.7}$$

where R and T are the gas constant and the absolute temperature, respectively. Clearly from this equation, the temperature dependence of the relaxation time has to be examined to evaluate the activation energy. As indicated in the previous section, the reduced relaxation time for the crosslinks is dependent on the swelling ratio. Hence, if the swelling ratio varies with the temperature, the actual value of E^* cannot be obtained. Figure 7.4 shows the temperature dependence of the swelling ratio. The swelling ratios were almost constant with respect to the variation of the temperature. Therefore, the value of E^* can be obtained as the slope of the Arrhenius plot of T_m/η, i.e., the plot of $\ln(T_m/\eta)$ against $1/T$.

The value of E^* for each sample is plotted against the swelling ratio, V/V_0, in Figure 7.5. E^* became smaller with the increase of V/V_0 and was not affected by M_c similarly to the case of the reduced relaxation time, T_m/η, if M_c is large.

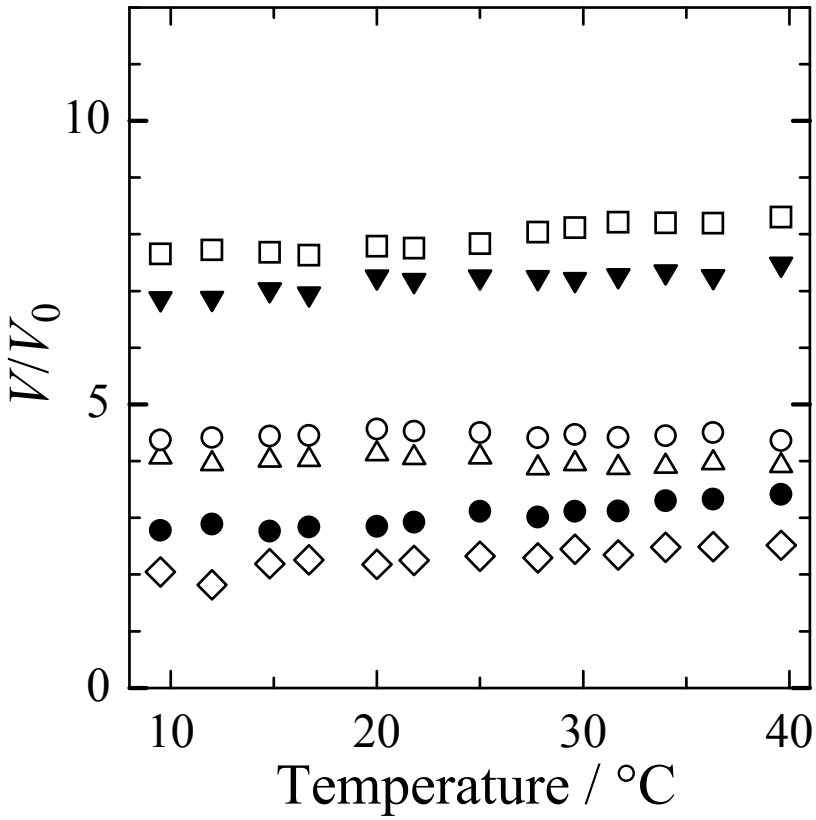

Figure 7.4. Temperature dependence of swelling ratio. Symbols: ▼, PMMA-0.3/toluene; ○, PMMA-0.5/toluene; ●, PMMA-1.0/toluene; □, PMMA-0.5/chloroform; △, PMMA-0.5/acetone; ◇, PMMA-0.5/acetonitrile.

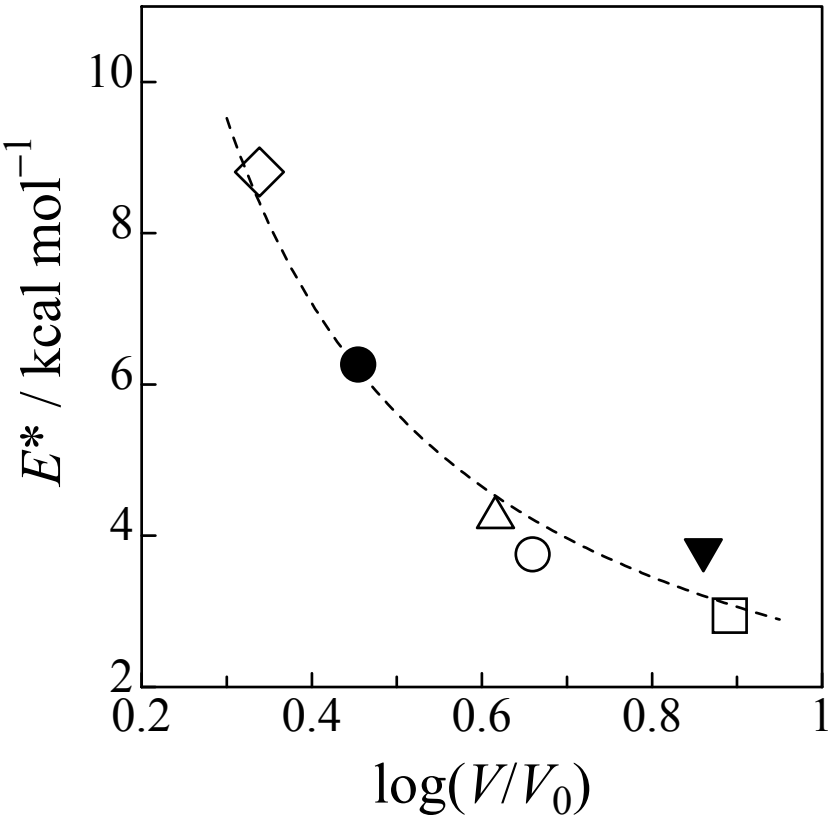

Figure 7.5. Relationship between activation energy of local motion and swelling ratio. Symbols are the same as those in Figure 7.4.

The relaxation time and the activation energy for the local motion at crosslinks were dependent only on the swelling ratio when M_c is large. When the swelling ratio becomes small, that is, the network chains shrink, the space around the probe is crowded with the network chain segments. The conformational transition of the chain is suppressed by this steric hindrance effect. Thus, the local motion of crosslinks is more constrained and the values of the relaxation time and the activation energy increase. The reorientation of the probe reflects the motion in a short length scale of the network chain, so that the local motion at crosslinks is independent of the length of

the network chain between crosslinks. In other words, if the network chain is sufficiently longer than the distance scale that influences on the motion of crosslinks (Figure 7.6a), rotational motion of the crosslinks is not affected by the neighboring crosslinks. Thus, the local motion of a gel at crosslinks is greatly dependent on the network chain expansion in the vicinity of crosslinks.

Finally, it should be noted the case that M_c is small. In Figure 7.3, T_m/η for PMMA-5.0 (×) deviated upwards from the line. For PMMA-5.0, the crosslinks are

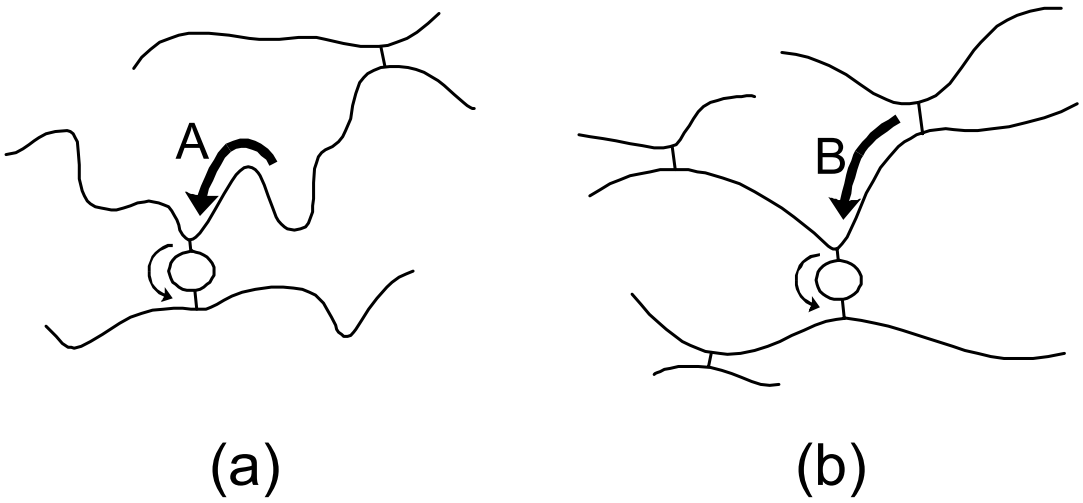

Figure 7.6. Schematic figures for the local motion of crosslinks for a gel when (a) M_c is large and (b) M_c is small. The labeled crosslinks (circles in this figure) reorient by the micro-Brownian motion of the neighboring network chains (arrows A and B). When the length of network chain between crosslinks is sufficiently long (case (a)), reorientation of the crosslinks is not affected by the neighboring crosslinks. In the case of (b), neighboring crosslinks have an influence on the reorientation of the labeled crosslinks (motion B) because the motion of the crosslinks is constrained by the neighboring one due to the short length between crosslinks.

separated only by about ten segments from each other, and the chain motion that affects the local dynamics of the crosslinks is restricted by the neighboring crosslinks (Figure 7.6b). Therefore, in the case of low M_c, the local motion of the labeled crosslinks also depends on the molecular weight between crosslinks.

7.4. CONCLUSION

We examined the local chain dynamics of a PMMA gel at crosslinks at the equilibrium swelling state by the fluorescence depolarization method. It was found that the mobility of crosslinks for gels depends only upon the swelling ratio, V/V_0, when the molecular weight between crosslinks, M_c, is large. In the case that M_c is small, the motion of the crosslinks is affected by both V/V_0 and M_c. These results indicate that the local motion of a gel at crosslinks is governed mainly by the segment density of the network chains in the vicinity of crosslinks when the length between crosslinks is long.

References

1. J. D. Ferry, "Viscoelastic Properties of Polymers," 2nd ed. John Wiley and Sons, New York, 1970.
2. E. Sato and T. Tanaka, *J. Chem. Phys.*, **89**, 1695 (1988).
3. Y. Kaneko, K. Sakai, A. Kikuchi, R. Yoshida, Y. Sakurai, and T. Okano, *Macromolecules*, **28**, 7717 (1995).
4. E. Geissler and A. M. Hecht, *Macromolecules*, **13**, 1276 (1980).
5. K. Urayama, T. Takigawa, and T. Masuda, *Macromolecules*, **26**, 3092 (1993).
6. E. Geissler, F. Horkay, A. M. Hecht, and M. Zrinyi, *J. Chem. Phys.*, **90**, 1924 (1989).
7. F. Horkay, M. Zrinyi, E. Geissler, and A. M. Hecht, *Makromol. Chem., Macromol. Symp.*, **40**, 195 (1990).
8. B. E. Eichinger, *Ann. Rev. Phys. Chem.*, **34**, 359 (1983).
9. T. Tanaka, L. O. Hocker, and G. B. Benedek, *J. Chem. Phys.*, **59**, 5151 (1973).
10. J. G. H. Joosten and J. L. McCarthy, *Macromolecules*, **24**, 6690 (1991).
11. T. Takebe, K. Nawa, S. Suehiro, and T. Hashimoto, *J. Chem. Phys.*, **91**, 4160 (1989).
12. H. Takahashi, M. Shibayama, H. Fujisawa, and S. Nomura, *Macromolecules*, **28**, 8824 (1995).
13. T. Tokuhiro, T. Amiya, A. Mamada, and T. Tanaka, *Macromolecules*, **24**, 2936 (1991).
14. T. Ikehara, T. Nishi, and T. Hayashi, *Polym. J.*, **28**, 169 (1996).
15. A. D. Stein, D. A. Hoffman, C. W. Frank, and M. D. Fayer, *J. Phys. Chem.*, **96**, 3269 (1992).
16. P. B. Leezenberg, A. H. Marcus, C. W. Frank, and M. D. Fayer, *J. Phys. Chem.*, **100**, 7646 (1996).

17. Y. Hu, K. Horie, T. Torii, H. Ushiki, and X. Tang, *Polym. J.*, **25**, 123 (1993).
18. Y. Hu, K. Horie, H. Ushiki, and F. Tsunomori, *Eur. Polym. J.*, **29**, 1365 (1993).
19. M. D. Ediger, *Ann. Rev. Phys. Chem.*, **42**, 225 (1991).
20. G. Fytas, T. Dorfmuller, L. Y. H., and B. Chu, *Macromolecules*, **14**, 1088 (1981).
21. G. Heinrich and T. A. Vilgis, *Macromolecules*, **25**, 404 (1992).
22. T. Sasaki, M. Yamamoto, and Y. Nishijima, *Macromolecules*, **21**, 610 (1988).
23. T. Sasaki, K. Nawa, M. Yamamoto, and Y. Nishijima, *Eur. Polym. J.*, **25**, 79 (1989).
24. J. Horinaka, K. Ono, and M. Yamamoto, *Polym. J.*, **27**, 429 (1995).
25. K. Ono, T. Sasaki, M. Yamamoto, Y. Yamasaki, K. Ute, and K. Hatada, *Macromolecules*, **27**, 5012 (1995).
26. K. Ono, K. Ueda, and M. Yamamoto, *Polym. J.*, **26**, 1345 (1994).
27. K. Ono, Y. Okada, S. Yokotsuka, T. Sasaki, and M. Yamamoto, *Macromolecules*, **27**, 6482 (1994).
28. J. Horinaka, M. Maruta, S. Ito, and M. Yamamoto, *Macromolecules*, **32**, 1134 (1999).
29. J. Horinaka, H. Aoki, S. Ito, and M. Yamamoto, *Polym. J.*, **31**, 172 (1999).
30. D. A. Waldow, B. S. Johnson, P. D. Hyde, M. D. Ediger, T. Kitano, and K. Ito, *Macromolecules*, **22**, 1345 (1989).
31. S. Adams and D. B. Adolf, *Macromolecules*, **31**, 5794 (1998).
32. M. G. Krakovyak, T. D. Ananieva, and S. S. Skorokhodov, *Synth. Comm.*, **7**, 397 (1977).
33. M. G. Krakovyak, T. D. Ananieva, E. Anufrieva, Y. Gotlib, T. Nekrasova, and S. S. Skorokhodov, *Synth. Comm.*, **7**, 397 (1977).
34. P. J. Flory, "Principles of Polymer Chemistry," Cornell University Press, Ithaca, New York, 1953.
35. C. Konak, Z. Tuzar, and J. Jakes, *Polymer*, **31**, 1866 (1990).

36. D. V. O'Cornner and D. Phillips, "Time-Correlated Single Photon Counting," Academic Press, London, 1984.

37. H. A. Kramers, *Physica*, **7**, 284 (1940).

SUMMARY

This thesis described the studies on polymer structures and dynamics by using the fluorescence techniques with high spatial and temporal resolutions. The first part of this thesis was concerned with the nanometric structure of polymer systems, and described the instrumentation of scanning near-field optical microscope with ultra-violet light (UV-SNOM) and its applications in observation and fabrication of polymer nano-structures. UV-SNOM was employed to examine the phase separation structures of polymer blend monolayers and the structural inhomogeneity of polymer gels. The second part focused on the nanosecond dynamics of polymers. The fluorescence depolarization method was employed for probing the rotational motion of polymer chain segments in dilute solutions and in gels. The study presented in each chapter is summarized below.

In Chapter 2, scanning near-field optical microscopy operated in an ultra-violet region (UV-SNOM) was developed and applied to polymer systems. An optical fiber probe made from pure silica allowed the use of UV light in SNOM measurements. The versatility of UV-SNOM for studying the nanometric structure of polymer systems was demonstrated by the following experiments. i) Fluorescence SNOM imaging and spectroscopy on polymer nano-particles were performed. Whereas the topographic measurement could not distinguish the latex beads labeled with different dyes, they were identified one by one through the spectroscopic measurement. ii) Photorecording/reading on a dye-labeled polymer monolayer was carried out by UV irradiation of the optical near-field with a high energy density. The spatial resolution for recording was estimated to be 120 nm, which was beyond the diffraction limit. iii) Single macromolecule detection was demonstrated for poly(isobutyl methacrylate) labeled with perylene. The weak fluorescence from the single polymer chain was

efficiently enhanced with the UV excitation. Thus, it was shown that UV-SNOM is a powerful tool for nanometric chemical analysis, nano-fabrication, and probing molecular information in addition to imaging the nano-structure of polymeric materials with a high resolution beyond the diffraction limit.

Chapter 3 described the fluorescence SNOM study on the phase separation structure of binary polymer blend monolayers, which consisted of pyrene-labeled poly(isobutyl methacrylate) (PiBMA-Py) and perylene-labeled poly(octadecyl methacrylate) (PODMA-Pe). SNOM observation was performed for the monolayers annealed at 40 °C prior to deposition onto substrates. Each phase of the completely phase-separated PiBMA-Py and PODMA-Pe was selectively imaged as a bright area by choosing the excitation wavelength (325 or 442-nm line of a He-Cd laser). The fluorescence SNOM enabled mapping of the excitation energy transfer efficiency between pyrene and perylene, which probed the region where the both components were mixed on the molecular level. The energy transfer emission was detected at the phase boundary, which had a width of a few hundred nanometer.

In Chapter 4, the phase separation behavior was studied for polymer blend monolayers of dye-labeled poly(octadecyl methacrylate) (PODMA) and poly(isobutyl methacrylate) (PiBMA). The sample monolayers were deposited onto a substrate after different periods of annealing at 40 °C on a water surface. Without annealing, the phase separation structure had an indented shape and a broad dispersion in size from ~ 100 nm to several tens of micrometers. The energy transfer emission was observed in the PODMA rich domain, indicating that the PiBMA chains were trapped in the PODMA domains. This was attributed to the strong crystallinity of octadecyl side chain. The phase separation process on a water surface was examined. The separation of both polymers was almost completed by annealing of several minutes, and then the domain size increased with annealing time. The structure of the phase boundary was examined through the energy transfer dynamics in a nanometric area.

The time-resolved fluorescence profiles were obtained across the phase interface. The fluorescence lifetime decreased at the interface with scanning the probe toward the acceptor-labeled polymer domain. The alteration of the fluorescence lifetime was observed in a range of several hundred nanometers. This result indicates the existence of the interfacial width on the order of hundred nanometers for the two-dimensional polymer blend. This width was markedly larger than the interfacial thickness expected in the three-dimensional bulk state.

In Chapter 5, the structural inhomogeneity of poly(methyl methacrylate) (PMMA) networks was studied by SNOM. The optically transparent PMMA network was labeled with fluorescent dyes either at the network chain or at the crosslinking points. The spatial distribution of the chain segments and crosslinks could be directly visualized in real space. The PMMA network with a crosslink density of 0.1 % had an inhomogeneous structure in a scale of several hundred nanometers, and the characteristic length for the structure decreased with the increase of crosslink density. Nanosecond dynamics of the energy transfer among the dyes introduced to the side-chain was also examined to probe the distribution of the chain segments on the molecular level. The local segment density was ca. 10 times higher than the ensemble average density. The local segment density had little correlation with the structure in a submicron scale observed in SNOM images. These findings indicated that the PMMA gel has structural hierarchy.

In Chapter 6, the local segmental motion at the center of the main chain of poly(*N*-vinylcarbazole) (PVCz) in dilute solutions was examined by the time-resolved fluorescence depolarization method. Anthracene-labeled PVCz's with various molecular weights in a range of $9.2 \times 10^3 - 1.0 \times 10^5$ were synthesized by living cationic polymerization. The relaxation time and the activation energy for the local motion were evaluated through the fluorescence anisotropy decay. The molecular weight dependence of the reduced relaxation time, T_m/η, was examined in THF and

toluene, which are good and Θ solvents, respectively. The reduced relaxation time in the good solvent increased with the increase of molecular weight and became a constant value of 2.3 ns cP^{-1} at a molecular weight of 25,000. In the Θ solvent, the value of T_m/η reached an asymptotic value at a molecular weight of ca. 50,000. Such the molecular weight dependence of the relaxation time could not be explained merely from the viewpoint of segment density, suggesting that the local potential for the rotational motion in dilute solutions is an important factor governing the local dynamics of the polymer chain. The local motion of PVCz was compared with those of other polymers: poly(isoprene), poly(oxyethylene), polystyrene, and PMMA. Both the relaxation time and the activation energy for PVCz were larger than those of the others, and PVCz had a larger critical molecular weight, which was defined as the molecular weight where the reduced relaxation time reaches the saturation value. This is attributed to the fact that the bulky side chain suppresses the conformational transition of the polymer backbone.

In Chapter 7, the local motion of crosslinking points of PMMA gels was examined by the fluorescence depolarization technique. The sample gels were labeled at crosslinking points with anthracene. The relaxation time and the activation energy for the local motion were measured for the PMMA gels with various molecular weights between cronsslinks, M_c, and in various swelling solvents. The mobility of crosslinks became faster with the increase of swelling ratio, and the relaxation time and the activation energy were independent of M_c and the solvent quality. In other words, when the swelling ratios were the same, the mobility of crosslinks was almost the same irrespective of the molecular weights between crosslinks and the solvent. This result indicates that the local motion of crosslinks for the PMMA gel is mainly governed by the segment density of network chains in the vicinity of crosslinks.

LIST OF PUBLICATIONS

Chapter 2

"UV-SNOM Characterization of Polymer Chains in an Ultrathin Monolayer"

Shinzaburo Ito, Hiroyuki Aoki, and Makoto Anryu

Trans. Mater. Res. Soc. Jpn., in press.

Chapter 3

"Phase-Separation Structure of a Monolayer of Binary Polymer Blend Studied by Fluorescence Scanning Near-field Optical Microscopy"

Hiroyuki Aoki, Yuji Sakurai, Shinzaburo Ito, and Tatsuo Nakagawa

J. Phys. Chem. B, **103**, 10553 (1999).

Chapter 4

"Two-Dimensional Polymers Investigated by Scanning Near-Field Optical Microscopy: 1. Phase Separation of Polymer Blend Monolayer"

Hiroyuki Aoki and Shinzaburo Ito

J. Phys. Chem. B, in press.

Chapter 5

"Nanometric Inhomogeneity of Polymer Network Investigated by Scanning Near-Field Optical Microscopy"

Hiroyuki Aoki, Shigeyuki Tanaka, Shinzaburo Ito, and Masahide Yamamoto

Macromolecules, **33**, 9650 (2000).

Chapter 6

"Local Chain Dynamics of Poly(*N*-vinylcarbazole) Studied by the Fluorescence Depolarization Method"

Hiroyuki Aoki, Jun-ichi Horinaka, Shinzaburo Ito, Masahide Yamamoto, Hiroshi Katayama, Masami Kamigaito, and Mitsuo Sawamoto

Polym. J., submitted.

Chapter 7

"Local Motion of Crosslinks for Poy(methyl methacrylate) Gels by the Fluorescence Depolarization Method"

Hiroyuki Aoki, Jun-ichi Horinaka, Shinzaburo Ito, and Masahide Yamamoto

Polym. Bull., **39**, 109 (1997).

Others

"Local Chain Dynamics of Several Polymers in Θ Solvents Studied by the Fluorescence Depolarization Method"

Masahide Yamamoto, Jun-ichi Horinaka, Hiroyuki Aoki, Keiko Tawa, and Shinzaburo Ito

J. Soc. Rheol. Jpn., **25**, 203 (1997).

"Molecular Weight Effect on Local Motion of Polystyrene Studied by the Fluorescence Depolarization Method"

Jun-ichi Horinaka, Hiroyuki Aoki, Shinzaburo Ito, and Masahide Yamamoto

Polym. J., **31**, 172 (1999).

ACKNOWLEDGMENT

The studies presented in this thesis were carried out at the Department of Polymer Chemistry, Graduate School of Engineering, Kyoto University from 1995 to 2000 under the guidance of Professor Shinzaburo Ito and Professor Masahide Yamamoto. I express my sincere gratitude to Prof. Shinzaburo Ito for his critical comments, valuable discussions, and continuous encouragement throughout this work. I am indebted to Prof. Masahide Yamamoto for kind guidance and thoughtful advice especially on the fluorescence depolarization studies.

I wish to thank Dr. Hideo Ohkita and Mr. Masataka Ohoka for their suggestion and advice in various situations.

I would like to thank Professor Mitsuo Sawamoto, Associate Professor Masami Kamigaito, and Mr. Hiroshi Katayama, Department of Polymer Chemistry, Kyoto University, for the preparation of anthracene-labeled poly(*N*-vinylcarbazole).

I would like to thank Professor Takeji Hashimoto and Associate Professor Hirokazu Hasegawa, Department of Polymer Chemistry, Kyoto University, for allowing the use of an ultra-microtome.

Thanks are also due to Professor Fumihiko Tanaka and Dr. Tsuyoshi Koga, Department of Polymer Chemistry, Kyoto University, for helpful discussion.

I am indebted to Professor Motoichi Ohtsu, Tokyo Institute of Technology, Dr. Shuji Mononobe, and Dr. Toshiharu Saiki, Kanagawa Academy of Science and Technology, for their helpful advice on the fabrication of the SNOM probes.

I am grateful to Professor Hiroo Iwata and Mr. Isao Hirata, Institute for Frontier Medical Sciences, Kyoto University, who allowed us to use a metal sputtering system.

Thanks are due to Dr. Tatsuo Nakagawa, Unisoku, Co. Ltd., for his technical support for the scanning near-field optical microscope. Without his help, I could not

start the SNOM studies.

I acknowledge the active collaboration and helpful discussion with the previous and present colleagues of Ito Laboratory: especially, Dr. Jun-ichi Horinaka, Mr. Shigeyuki Tanaka, Mr. Yuji Sakurai, Mr. Makoto Anryu, and Mr. Yuichiro Kunai. Without their encouragement and collaboration, I could not carry out my studies.

At last, I express my sincere gratitude to my parents, Shinya Aoki and Tomiko Aoki, for their support and encouragement.

January, 2001

Hiroyuki Aoki